

Spin-Polarized Electrons in Monolayer MoS₂

Inauguraldissertation

zur
Erlangung der Würde eines Doktors der Philosophie
vorgelegt der
Philosophisch-Naturwissenschaftlichen Fakultät
der Universität Basel
von

Jonas Gaël Roch

Basel, 2019

The original document is saved on the university of Basel document server
<http://edoc.unibas.ch>



This work is licensed under a Creative Commons
Attribution-NonCommercial-NoDerivatives 4.0 International License.

The complete text may be reviewed here:
<http://creativecommons.org/licenses/by-nc-nd/4.0/>

Genehmigt von der Philosophisch-Naturwissenschaftlichen Fakultät auf Antrag von

Prof. Dr. Richard J. Warburton

Prof. Dr. Illaria Zardo

Prof. Dr. Bernhard Urbaszek

Basel, den 25. Juni 2019

Prof. Dr. Martin Spiess
Dekan

Acknowledgments

First, I would like to thank Richard Warburton for his supervision and spending hours with me, drawing MoS₂'s band structure. His enthusiasm for interesting new physics has been motivating me for the whole duration of my Thesis. His deeply rational thinking has always helped to focus on the essence of the physics at play and not to get lost into details.

Then, I would also give a special thank to Guillaume Froehlicher who supervised me for a year. His high levels of curiosity and perfection have definitely been key factors to the success of the main outcomes of this Thesis. I would also like to thank Peter Makk for his supervision, although he was from a different research group. Dmitry Miserev helped also significantly to understand the main results in this Thesis with his expertise in theory.

Of course, I would also like to thank all the members of the Nano-Photonics' group as a whole. Idea exchanges over coffee breaks and other Mensa meals have definitely contributed to the main results of this Thesis. Thank you as well to the whole staff of both the electronic and mechanical workshops. Their help and expertise helped in the realisation of the experimental setups. All my friends that made the time of my studies fun also deserve a big thank you! Whether in a bar or in the Swiss alps, they were always here for me !

I would also like to thank my family for their support. They supported me for all my studies and always helped me to take the right decisions in life. A special thank goes to my girlfriend Sonia for her support when things went wrong in the lab. She was always here to support me whenever I needed it.

Contents

1	Introduction	1
2	Transition metal dichalcogenides	6
2.1	Band structure	7
2.2	Optical transitions	8
2.2.1	Excitons	9
2.3	Coulomb interaction in a two-dimensional electron gas	10
2.3.1	Non-interacting electron gas	10
2.3.2	Coulomb interaction	11
2.3.3	Screening	14
3	Methods	18
3.1	Sample fabrication	18
3.1.1	Exfoliation and identification of monolayers	18
3.1.2	Building van der Waals heterostructures	21
3.1.3	Electrical contacts to Van der Waals heterostructure	25
3.2	Optical characterisation setup	26
3.2.1	Photoluminescence measurement	27
3.2.2	Absorption measurement	28
4	Quantum-Confined Stark Effect in a MoS₂ Monolayer van der Waals Heterostructure	31
4.1	Introduction	32
4.2	Device and device characterization	33
4.3	Measurement of the Stark shift at low electron concentration	35
4.4	Conclusion	39
4.5	Methods	39
5	Spin-Polarized Electrons in Monolayer MoS₂	44
5.1	Introduction	45
5.2	Methods	46

5.3	Optical susceptibility of a monolayer of MoS ₂ at various electron concentrations	47
5.4	Conclusion	51
6	First order phase transition in a MoS₂ itinerant ferromagnet	55
6.1	Introduction	55
6.2	Methods	57
6.3	Results and discussion	59
6.4	Conclusion	63
7	Conclusion	66
A	Supplementary information to chapter 5 “Spin-Polarized Electrons in Monolayer MoS₂”	69
A.1	Sample fabrication	70
A.2	Experimental setup	71
A.3	Reflectivity of a thin film: determination of the susceptibility	73
A.4	Selection rules and valley Zeeman effect	77
A.5	Theory of trion absorption in a 2DEG	81
A.6	Band filling and optics in MoS ₂	85
A.7	Temperature dependence of the optical susceptibility	88
A.7.1	Reproducibility of the data	88
B	Details of the Hartree-Fock calculation	95
B.1	Idea of the computation	95
B.2	Kinetic energy term	97
B.3	Intervalley Coulomb term	97
B.4	Intravalley Coulomb term	98
B.5	Expression of the 2DEG as a function of carrier densities	99

Chapter 1

Introduction

Moore's law has predicted feature sizes in the semiconductor industry for more than several decades [1]: the number of transistors on an integrated circuit doubles every two years. However, as the feature sizes in transistors approach the nanometer scale, the semiconductor industry is hitting a physical limit: the electron flow at these small scales is limited by the quality of the interfaces in all three spatial directions.

Layered van der Waals crystals gained a great interest after K. Novoselov and A. Geim were awarded the Nobel Prize for their work on graphene [2]. As the name indicates it, these crystals consist of weakly bound sheets with a thickness of less than a nanometer, given by the size of the unit cell of the material. The extend of the electron wavefunction in these materials is mostly limited to the plane of the sheets, so that a single sheet of a van der Waals material can be used as an active material and be a "clean" interface at the same time.

Standard semiconductor materials, based on bulk 3D crystals (*e.g.* silicon, germanium, gallium arsenide...) have strong chemical bonds in the three spatial directions, imposing strict rules for hetero-epitaxy such as lattice-matching. The weak binding between the sheets of van der Waals crystals makes it possible to stack different van der Waals materials without compromises [3, 4] within a van der Waals heterostructure [4], creating functional devices with semiconductor materials, metals and insulators layers within a few nanometers. There is a wide variety of van der Waals materials, and new materials continuously join this growing class of materials. Relevant to this thesis are the monolayers of the optically active transition metal dichalcogenides (TMDCs) and in particular molybdenum disulfide (MoS_2), molybdenum diselenide (MoSe_2), tungsten disulfide (WS_2) and tungsten diselenide (WSe_2). These four materials are semiconductors in the monolayer limit with a direct band-gap in the red part of the optical spectrum. It was shown that both the optical [5] and electronic transport properties [6] are significantly improved when the monolayer crystal is placed within two thin layers of the insulating material hexagonal boron nitride (h-BN), forming a Van der Waals

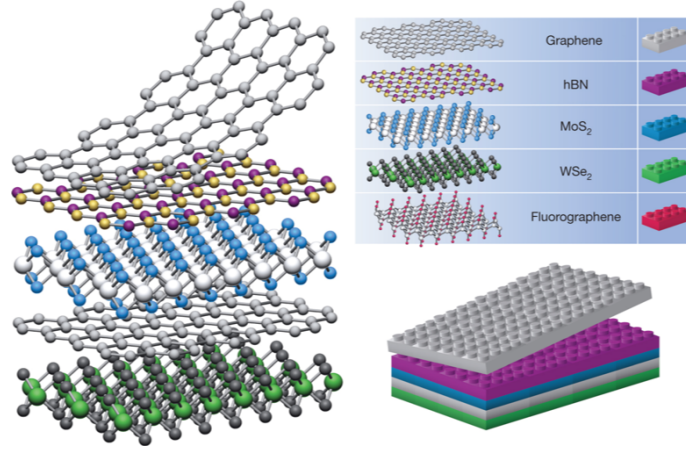


Fig. 1.1. Idealised Van der Waals heterostructure presented as Lego bricks. Image from Ref. [4].

heterostructure.

The lack of dangling bonds combined with the atomic thicknesses of van der Waals materials make them interesting as a way to extend Moore's law [7]. There are however a few challenges to overcome before van der Waals materials make it to our private computers [7]. An obvious challenge is the growth: large scale growth of van der Waals materials remains challenging. The best properties are still obtained by mechanical exfoliation (*i.e.* the scotch tape method, discussed in the Method chapter). This method provides an easy way to fabricate elaborated heterostructures. Another challenge is to understand how the truly two-dimensional nature of these materials impact their physical properties. The reinforced Coulomb interaction in 2D impacts basic properties of the semiconductor, such as the effective mass of the electrons [8] or the ground state for instance.

This thesis focusses mostly on the second challenge: understanding how the 2D nature of van der Waals materials impacts the physical properties of a material. Absorption and photoluminescence spectroscopy is used to study the optical properties of monolayer MoS₂ with and without the presence of free electrons.

In Section 1, the band structure of TMDCs and their optical excitation spectrum are discussed, introducing the concept of exciton. Then, Coulomb interaction in a 2D material will be introduced. The most important Coulomb matrix elements for TMDCs are derived in this Section. In Section 3, the fabrication techniques used for the fabrication of our sample are explained. In the same Section, the scotch tape technique and how individual few-nanometer-thick layers can be stacked to form a van der Waals heterostructure are discussed. The experimental details on photoluminescence and ab-

sorption spectroscopy are also discussed in this Section.

Excitons, the lowest energy optical excitations of an uncharged semiconductor, are formed by an electron-hole pair. When an external electric field is applied, the electron and the hole will tend to separate thus creating a dipole moment aligned with the electric field, lowering the energy of the exciton. This feedback mechanism is named the Stark effect, characterised by the polarisability of the exciton. In Section 4, we will discuss the measurement of the Stark effect in a van der Waals heterostructure formed by a single layer MoS₂ encapsulated in the insulator material hexagonal boron nitride. The minute polarisability that we measure unambiguously proves the 2D nature of monolayers TMDCs [9].

The 2D dimensionality of our sample also has dramatic consequences on the electron-electron Coulomb interaction. We present in Section 5 how we make use of optical absorption to investigate the ground state of free electrons in a directly contacted monolayer of MoS₂. The extreme strength of Coulomb interaction in MoS₂ allows a regime in which Coulomb interaction dominates over Pauli-blocking to be probed [10]. We find that the electronic ground state is spin-polarized up to a large electron density [11]. This spontaneous symmetry breaking was not expected by standard 2DEG, in which any long-range ferromagnetic order is excluded at finite temperature as a result of the Mermin-Wagner theorem [12]. In MoS₂, the small but finite spin-orbit interaction lifts the conditions of the Mermin-Wagner theorem and allows for an Ising-type of ferromagnetic ordering. The roots of the spin-polarisation are to be found in infrared electron-hole pair excitations near the Fermi surface [13].

In the last part, we will discuss the dramatic effects of the spin-polarised electronic ground state on the optical properties of electron doped MoS₂. We will show how photoluminescence spectroscopy can be used to witness that a MoS₂ 2DEG undergoes a first-order phase transition between the ferromagnetic phase and the normal paramagnetic phase as the electron density increases. The first order nature of the phase transition is not expected from the standard Ginzburg-Landau theory and relies on non-analyticities in the thermodynamic potential [13].

Bibliography

- [1] Moore, G. E. Cramming more components onto integrated circuits. *Electronics* 114 (1965).
- [2] Novoselov, K. S. *et al.* Electric field effect in atomically thin carbon films. *Science* **306**, 666 (2004).
- [3] Novoselov, K. S., Mishchenko, A., Carvalho, A. & Castro Neto, A. H. 2D materials and van der Waals heterostructures. *Science* **353**, 461 (2016).
- [4] Geim, A. K. & Grigorieva, I. V. Van der Waals heterostructures. *Nature* **499**, 419 (2013).
- [5] Cadiz, F. *et al.* Excitonic linewidth approaching the homogeneous limit in MoS₂-based van der Waals heterostructures. *Phys. Rev. X* **7**, 021026 (2017).
- [6] Pisoni, R. *et al.* Interactions and magnetotransport through spin-valley coupled Landau levels in monolayer MoS₂. *Phys. Rev. Lett.* **121**, 247701 (2018).
- [7] Li, M.-Y., Su, S.-K., Wong, H.-S. P. & Li, L.-J. How 2D semiconductors could extend Moore’s law. *Nature* **567**, 169 (2019).
- [8] Žak, R. A., Maslov, D. & Loss, D. Spin susceptibility of interacting two-dimensional electrons in the presence of spin-orbit coupling. *Phys. Rev. B* **82**, 115415 (2010).
- [9] Roch, J. G. *et al.* Quantum-confined Stark effect in a MoS₂ monolayer van der Waals heterostructure. *Nano Lett.* **18**, 1070 (2018).
- [10] Attaccalite, C., Moroni, S., Gori-Giorgi, P. & Bachelet, G. B. Correlation energy and spin polarisation in the 2D electron gas. *Phys. Rev. Lett.* **88**, 256601 (2002).
- [11] Roch, J. G. *et al.* Spin-polarized electrons in monolayer MoS₂. *Nat. Nanotechnol.* **14**, 432–436 (2019).

- [12] Mermin, N. D. & Wagner, H. Absence of ferromagnetism or antiferromagnetism in one- or two-dimensional isotropic Heisenberg models. *Phys. Rev. Lett.* **17**, 1133 (1966).
- [13] Miserev, D., Klinovaja, J. & Loss, D. Spontaneous Symmetry Breaking in Monolayers of Transition Metal Dichalcogenides. *arXiv e-prints* arXiv:1902.07961 (2019). arXiv:[1902.07961](#).

Chapter 2

Transition metal dichalcogenides

Layered transition metal dichalcogenides (TMDs) consist of a plane of a transition metal atom (M) sandwiched between two planes of chalcogen atoms (X), with stoichiometry MX_2 . Fig. 2.1(b) shows the atomic structure of a plane of a TMD with the transition metal in the middle, in grey. Seen from the top, as in Fig. 2.1(a), the lattice is hexagonal with each two site corresponding to the two chalcogen atoms (overlapping). From Fig. 2.1(b), one can clearly see that monolayers of TMDs lack inversion symmetry. The broken inversion symmetry has profound consequences on the band structure and the optical properties of monolayers of TMDs.

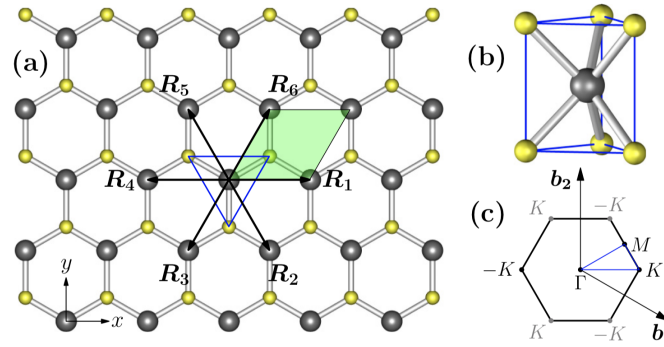


Fig. 2.1. **Crystal lattice of monolayer MoS_2 .** (a) Top view of the crystal lattice. The molybdenum atoms are depicted in grey and the sulphur atoms are drawn in yellow. The lattice is similar to the staggered graphene lattice. (b) Drawing of the three dimensions unit cell. One can notice that the crystal lattice does not respect inversion symmetry. (c) The first Brillouin zone of monolayer MoS_2 is defined by the area defined by the vectors b_1 and b_2 . The Brillouin zone contains both the K and K' point. Image from Ref. [1].

2.1 Band structure

Seen from the top, as in Fig. 2.1(a), monolayers TMDs consists of two hexagonal sublattices with lattice constant a_{latt} formed by the chalcogen atoms and the transition metal atoms. Similar to graphene, TMDs have band edges at the $K = \frac{4\pi}{3a_{latt}}$ and $K' = -K$ points. However, TMDs are semiconductors with a finite band-gap E_g and exhibit parabolic bands around the K and K' points. Fig. 2.2 shows the band structure of the TMD molybdenum disulfide, MoS_2 . The large angular momentum of d -orbitals of the transition metal atom induces a large spin-orbit splitting ($\Delta_{VB} \approx 150$ meV) of the two valence bands. On the other hand, the states in the conduction band have mostly a s -orbital nature, limiting the spin-orbit splitting of the two conduction bands to $\Delta_{CB} \approx 3$ meV. A direct consequence of the finite spin-orbit interaction and broken inversion symmetry is the inversion of the spins of the band edges in TMDs. The band edges are located at the K and K' points. The spin (indicated by the arrows and the colours of the lines) are inverted at the inequivalent K and K' points.

In MoS_2 , there is a strong imbalance between the strength of the spin-orbit splitting of the bands in the conduction band and the valence bands, making this semiconductor unique in the family of the TMDs (see Table 2.1). In chapter 5, we will see how the small value of the spin-orbit interaction in the conduction band of MoS_2 has a deep impact on the electronic ground state of electron-doped MoS_2 .

The band structure of MoS_2 extracted from DFT calculation has been accurately described in terms of an effective hamiltonian close to the band edges, at the proximity of the K and K' points [2]. For the conduction band, in the absence of an out-of-plane magnetic field, the band structure can be written simply written as

$$H = \frac{\hbar^2 q^2}{2m_{CB}^{\tau,s}} + \tau \Delta_{CB} s_z , \quad (2.1)$$

where $m_{CB}^{\tau,s}$ is the electron effective mass in the conduction band in the valley with index τ and spin s_z . τ is defined such that $\tau = 1(-1)$ for K (K') and s_z is defined such that its eigenvalues are $s = \pm 1$. The momentum q is measured from the bottom of the band at K or K' . Δ_{CB} is the spin-orbit splitting of the two low energy conduction bands. A similar hamiltonian can be written for the valence band.

Table 2.1 lists common values of the parameters appearing in the effective hamiltonian of Eq. 2.1.

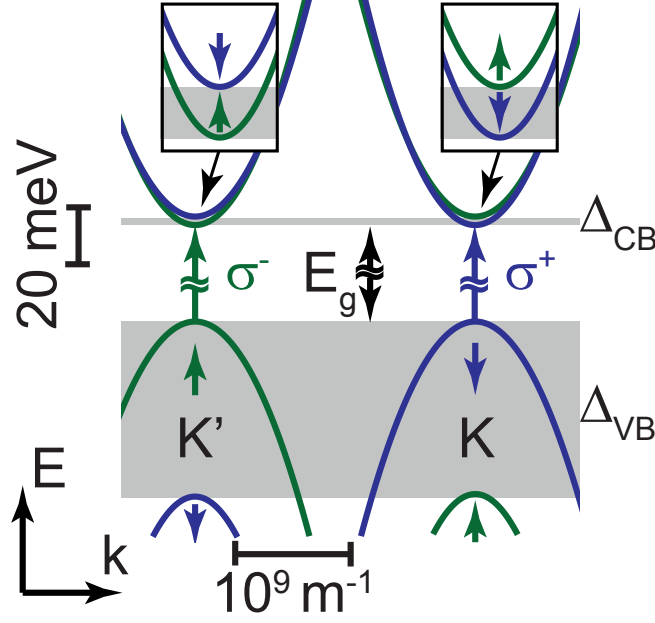


Fig. 2.2. **Band structure of monolayer MoS₂.** MoS₂ has four conduction bands and four valence bands that are experimentally relevant. A direct band-gap $E_g \approx 2.0$ eV is formed at the inequivalent K and K' points of the Brillouin zone. A small spin-orbit interaction splits the spin states in the conduction band by $\Delta_{CB} \approx 3$ meV. In the valence band, the spin splitting is significantly larger with $\Delta_{CB} \approx 150$ meV. The broken inversion symmetry implies that the spin ordering of the bands at the K point is the inverse of that of the K' point.

Material	E_g (eV)	$2\Delta_{CB}$ (meV)	$2\Delta_{VB}$ (meV)	m_{CB}^\downarrow	m_{CB}^\uparrow	m_{VB}
MoS ₂	1.59-2.97	3	148	0.44	0.49	0.54
WS ₂	1.58-3.11	-38	429	0.27	0.35	0.35
MoSe ₂	1.34-2.33	23	186	0.56	0.64	0.59
WSe ₂	1.27-2.51	-46	466	0.3	0.4	0.36

Table 2.1. Calculated band structure parameters for different TMDs. All reported values are from Ref. [3]. Due to the large spread of the calculated values of the band-gap, I report the upper and lower bounds of the band-gap energy.

2.2 Optical transitions

Optical transitions conserve the total angular momentum and momentum. As a photon has a momentum close to zero, photons can only couple bands of the same valley. A circularly-polarized photon carries an angular momentum of ± 1 . For a quantum dot or an atom, we would then just need to verify that the change in angular momentum between the initial state and the final state is $\Delta m = \pm 1$. However, as the band edges are

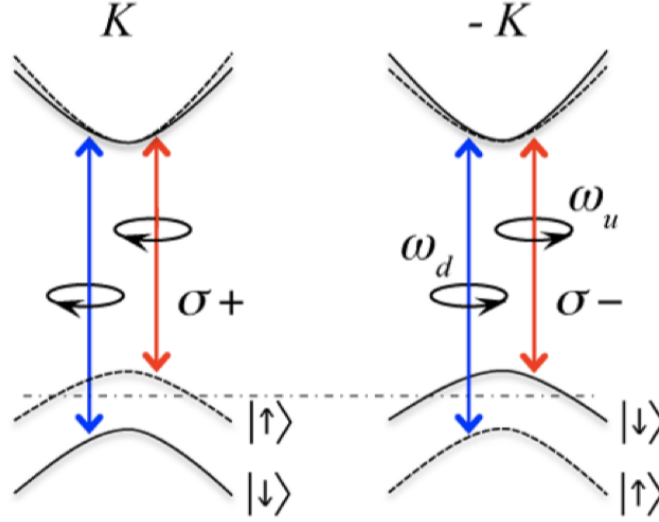


Fig. 2.3. **Optical selection rules in monolayer transition metal dichalcogenides.** Due to the broken inversion symmetry of the crystal lattice, it is possible to excite an electron-hole pair in a specific valley using circularly polarised light (σ^+ and σ^- polarisations). As the spin-orbit splitting is large in the valence band (≈ 100 meV), we can excite A-excitons at frequency $\hbar\omega_u$ and B-excitons at frequency $\hbar\omega_d$. The band ordering here is typical from tungsten-based transition metal dichalcogenides. Figure from Ref. [5].

located at the K point, the orbital magnetic moment of the electrons have a contribution stemming from the intercellular current circulation [4]. The sign of this contribution depends on the position in the Brillouin zone and is opposite at the K point than that at the K' point. For instance, it was shown that in MoS_2 , the conduction bands with $m_z = -2(2)$ are optically coupled to the $m_z = 0$ valence bands with $\sigma^+(\sigma^-)$ photons [5]. Fig. 2.3 shows the optical transitions in monolayer MoS_2 .

2.2.1 Excitons

We have previously discussed the inter-band selection rules which dictate which valence band can be coupled to which conduction band. In a single particle picture, we need at least a photon energy greater than the bandgap energy E_g in order to promote an electron from the valence band to the conduction band. This type of transition is characterised by an absorption threshold in the absorption spectrum: photons with energies higher than E_g will be absorbed by the single-particle type of transitions.

The many electrons present in the system (full valence band !) are however interacting via Coulomb interaction. Coulomb interaction impacts the inter-band transitions by creating a bound state at energy lower than the band-gap. This state can be understood

as a bound electron-hole pair: when promoting an electron from the valence band to the conduction band, an unoccupied state is left in the valence band. This unoccupied state can be seen as a hole, a positively charged particle that can bind with the photo-promoted electron. This electron-hole pair is the analogous of a hydrogen atom: the binding energies are given by the Rydberg in the system and the possible wave-functions are described by the 2D hydrogen excitation spectrum 1s, 2s... with energies, counted from the effective bandgap (E_g plus the electron and hole confinement energies) given as

$$E_n = -E_0 \frac{1}{(n + 1/2)^2}, \quad n = 0, 1, \dots \quad \text{with} \quad E_0 = \frac{e^2}{8\pi\epsilon_0\epsilon_r a_0}. \quad (2.2)$$

Here, a_0 is the Bohr radius of the exciton,

$$a_0 = \frac{4\pi\epsilon_0\epsilon_r\hbar^2}{m_r e^2}, \quad (2.3)$$

which is extremely small in TMDs due to the large electron and hole effective masses and the relatively small relative dielectric constant ϵ_r . These results can be derived under the assumption of an unscreened $\propto 1/r$ Coulomb potential [6]. An exciton binding energy of 320 meV was experimentally measured in the TMD WS_2 showing the extreme strength of excitonic features in TMDs [7]. However, the same work [7] reported deviations to the idealistic hydrogen series of Eq. 2.2, hence showing that the $1/r$ Coulomb potential may not be completely valid in TMDs.

2.3 Coulomb interaction in a two-dimensional electron gas

Free electrons interact with each other via Coulomb interaction. In Chapter 5, we will discuss an experiment where Coulomb interaction is dominating all other energy scales in the system.

2.3.1 Non-interacting electron gas

Electrons carry a spin-1/2 and are therefore Fermions. In the frame of the second quantisation, we can define $a_{k,\sigma}^\dagger$ and $a_{k,\sigma}$, the creation and annihilation operators for an electron with wave-vector k and spin σ . The particle operator $n_{k,\sigma} = a_{k,\sigma}^\dagger a_{k,\sigma}$ informs about the occupancy of the state with quantum numbers (k, σ) . As two Fermions cannot populate the same state, $n_{k,\sigma} \in \{0, 1\}$, $\forall (k, \sigma)$. For parabolic bands with energy dispersion $\epsilon_\sigma(k) = \hbar k^2/2m$, the 2DEG ground state can be written in the form of a Fermi sea

$|FS\rangle$:

$$|FS\rangle = \prod_{\{k: \|k\| \leq \|k_\sigma^F\|\}} a_{k,\sigma}^\dagger |0\rangle \quad (2.4)$$

where $\|k_\sigma^F\|$ is the Fermi wave-vector and $|0\rangle$ is the state where describing the intrinsic semiconductor with a filled valence band and an empty conduction band.

2.3.2 Coulomb interaction

Electrons interact via Coulomb interaction. The density of electrons at a given point r , $\rho(r)$ can be used to measure the overall energy from Coulomb interaction E_C as

$$E_C = \int d^2r d^2r' \rho(r) \rho(r') V(r - r') [1 - \delta(r' - r)] , \quad (2.5)$$

where the term $[1 - \delta(r' - r)]$ takes the term $r' = r$ out of the integration as it is an infinite contribution stemming from the Coulomb interaction of an electron with itself (self-energy).

The density $\rho = n(r)$ can be expressed in term of the field operators

$$\rho(r) = \sum_{\sigma} \psi_{\sigma}^\dagger(r) \psi_{\sigma}(r) \quad (2.6)$$

By definition of the field operators,

$$\psi_{\sigma}(r) = \sum_k a_{k,\sigma} e^{ikr} , \quad (2.7)$$

we can obtain the Hamiltonian for Coulomb interaction in term of the creation and annihilation operators

$$H_C = \frac{1}{2} \sum_{(k,\sigma)} \sum_{(k',\sigma')} \sum_{q \neq 0} V_q a_{k+q,\sigma}^\dagger a_{k'-q,\sigma'}^\dagger a_{k',\sigma'} a_{k,\sigma} \quad (2.8)$$

In order to derive Eq. 2.8, the only assumption is that the interaction energy depends on the density at point r and at point r' . The $r - r'$ dependence of the interaction is translated in Fourier space by the wavevector q being the Fourier transform of $r - r'$. The energy needed to bring a particle with charge e from far away at a distance $|r - r'|$ from another particle with charge at r is given by

$$V(r - r') = \frac{1}{4\pi\epsilon_0} \frac{e^2}{|r - r'|} \quad V_q = \frac{e^2}{2\epsilon_0 L^2} \frac{1}{q} , \quad (2.9)$$

where L is the size of the crystal on taking the 2D Fourier transform. Details of the Fourier transform can be found in Ref. [6].

Inter- and intra- valley Coulomb interaction

The Coulomb interaction Hamiltonian in Eq. 2.8 shows that Coulomb scattering processes conserve both the spin and the total momentum: a momentum q is transferred from a particle with spin σ and momentum k to a particle with spin σ' and momentum k' . In the case of the TMDs, there are four valence bands that can be filled. The additional valley degree of freedom needs to be taken into account by the Hamiltonian. The non-interacting Hamiltonian H_0 is given by Eq. 2.1, that we rewrite within the frame of the second quantization:

$$H_0 = \sum_{k,\sigma,\tau} \underbrace{\left(\frac{\hbar^2 k^2}{2m_{CB}^{\tau,s}} + \tau \Delta_{CB} s_z \right)}_{\epsilon_{\sigma,\tau}(k)} a_{k,\sigma}^\dagger a_{k,\sigma} = \sum_{k,\sigma,\tau} \epsilon_{\sigma,\tau}(k) a_{k,\sigma}^\dagger a_{k,\sigma} . \quad (2.10)$$

In Eq. 2.10, the sums over the degrees of freedom of the electron states now account for the valley index τ , therefore restricting the sum over wavevector k in the vicinity of the $\tau \cdot K$ point with $\tau \in \{-1; 1\}$.

We rewrite now the Coulomb interaction of Eq. 2.8 in two parts: the intra-valley part H_C^{intra} and the inter-valley part H_C^{inter} . The intra-valley Coulomb interaction is basically described by the same hamiltonian as in Eq. 2.8, while the inter-valley interaction describes scattering processes between electrons living in different valleys.

$$H_C^{intra} = \frac{1}{2} \sum_{q \neq 0} \sum_{(k,\sigma,\tau)} \sum_{(k',\sigma',\tau')} V_q \hat{a}_{k+q,\sigma,\tau}^\dagger \hat{a}_{k'-q,\sigma',\tau'}^\dagger \hat{a}_{k',\sigma',\tau'} \hat{a}_{k,\sigma,\tau} \quad (2.11)$$

$$H_C^{inter} = \frac{1}{2} \sum_q \sum_{(k,\sigma,\tau)} \sum_{(k',\sigma',\tau')} V_{q+K} \hat{a}_{k+q,\sigma,-\tau}^\dagger \hat{a}_{k'-q,\sigma',-\tau'}^\dagger \hat{a}_{k',\sigma',\tau'} \hat{a}_{k,\sigma,\tau} \quad (2.12)$$

As q is an intra-valley wave-vector, it is extremely small compared to the Brillouin-zone sized wave-vector K . The inter-valley Coulomb scattering elements V_{q+K} can therefore be considered as a constant

$$V_{q+K} \approx V_K = \frac{e^2}{2\epsilon_0 L^2} \frac{3a_{latt}}{4\pi} \quad (2.13)$$

Hartree-Fock approximation

The Fermi sea was discussed as the ground state of the non-interacting electron gas. Here, the impact of Coulomb interaction is discussed within the frame of the Hartree-Fock approximation. The Hartree-Fock calculation is a variational computation based on a non-interacting initial Hamiltonian and Coulomb interaction is added as a perturbation. The mechanism of exchange will appear from the calculation, a mechanism yielding a reduction of the energy due to Coulomb interaction.

We perform here a variational computation of the energy of the 2DEG. We consider that the 2DEG wavefunction is described by a Fermi sea occupying an area Ω in the Hilbert space. The goal is to minimize the 2D electron gas energy by finding the optimal geometry for Ω .

The domain Ω is defined in terms of the Fermi wavevectors $k_F^{\sigma,\tau}$ in the different valleys (momentum measured from the bottom of the bands). Ω can be written (see Appendix B) as

$$\Omega = \bigcup_{\sigma=\pm 1, \tau=\pm 1} \{k, \text{ s.t. } |k| < k_F^{\sigma,\tau}\} \quad (2.14)$$

$$|\Psi_\Omega\rangle = \prod_{(k,\sigma,\tau) \in \Omega} \hat{a}_{k,\sigma,\tau}^\dagger |0\rangle \quad (2.15)$$

The Hamiltonian of the system is made of the three parts discussed in Eq. 2.10, Eq. 2.11 and Eq. 2.12. The energy E_Ω of the variational wave-function $|\Psi_\Omega\rangle$ is evaluated for a given domain Ω :

$$E_\Omega = \langle \Psi_\Omega | \hat{H} | \Psi_\Omega \rangle = \langle \Psi_\Omega | H_0 | \Psi_\Omega \rangle + \langle \Psi_\Omega | H_C^{intra} | \Psi_\Omega \rangle + \langle \Psi_\Omega | H_C^{inter} | \Psi_\Omega \rangle \quad (2.16)$$

In Appendix B, the details of the computation of the energy are given. After lengthly operator algebra, the energy E_Ω can be expressed in term of the population $n_{\sigma,\tau}$ of each of the Fermi seas

$$\frac{E_\Omega^0}{L^2} = \underbrace{\sum_{(\sigma,\tau)} 2n_{\sigma,\tau} \Delta_{CBT} s_z + \pi n_{\sigma,\tau}^2 \frac{\hbar^2}{m}}_{\text{Single-particle energy}} - \underbrace{2V_{|K|} L^2 \sum_{\sigma,\tau} n_{\sigma,-\tau} n_{\sigma,\tau}}_{\text{Inter-valley exchange}} - \underbrace{\sum_{\sigma,\tau} \frac{e^2 C}{3\pi\epsilon_0} (2\pi n_{\sigma,\tau})^{3/2}}_{\text{Intra-valley exchange}}, \quad (2.17)$$

where

$$C = \sum_{l=0,2,\dots,\infty} \frac{2}{l+2} \left[\frac{1}{2^l} \binom{l}{l/2} \right]^2 \approx 1.26. \quad (2.18)$$

Coulomb interaction yields an energy reduction to the single-particle energies. This energy reduction is named exchange and it is known that the Hartree method overestimates its value [6]. An interesting feature is that the unscreened intra-valley exchange scales as $n^{3/2}$ whereas the single particle energies scale as n^2 . At low carrier densities, it can therefore be expected that exchange could dominate and create a spin- and valley-polarization. This exact mechanism was proposed to explain population of a single Fermi sea at low carrier density in WS₂ [8].

The inter-valley term derived from the Hartree-Fock calculation shows that the electron population of one band drags the energy of the other band with the same spin but opposite valley index to lower energy [9]. Although this simple Hartree-Fock approach is crude and incorrect, it already underlines the importance of inter-valley exchange as a means to favour spin-polarisation. In Chap. 5, we present an experiment where the inter-valley exchange term dominates over all other energy scales in the system: we demonstrate that the 2DEG electronic ground-state at “low” electron density is spin-polarised.

In the absence of spin-orbit interaction, Mermin-Wagner theorem however excludes the creation of a spin-polarized 2DEG ground state at finite temperature. The reason is that fluctuations are extremely strong in two dimensions. In presence of spin-orbit interaction, the Mermin-Wagner theorem doesn’t hold anymore. Fluctuations remain nevertheless important and should be taken into account. The Hartree-Fock mechanism presented here is based on a mean-field description which neglect fluctuations and is therefore inaccurate. A complete computation accounting for fluctuations is presented in Ref. [10].

2.3.3 Screening

In the computation presented above, the Coulomb potential was considered to be a diverging function of the wave-vector q . Translated into a real-space picture, electrons that are far away from each other interact. However, in our experiments, we typically have electron densities of 10^{12} cm^{-2} . These electrons create charge density fluctuations that screen the interaction at long distance. These density fluctuations can be caused by either collective excitations, named plasmons, or by simple electron-hole pair excitations.

In order to account for the effect of the many electrons around, one should consider that the electric potential at a given point is given by the sum of the Coulomb potential of a test charge and of the potential stemming from the feedback of all the other electrons:

$$V_{eff} = V + V_{ind} , \quad (2.19)$$

where V_{eff} is the effective Coulomb interaction, V is the Coulomb potential of a test charge and V_{ind} stems from the feedback of all the other electrons. It can be shown that within the framework of the rotating phase approximation (RPA), the screened Coulomb potential V_{eff} can be related to the unscreened Coulomb interaction V via the dielectric function $\epsilon(\omega, k)$ obtained with the Lindhard formula

$$\epsilon(\omega, q) = V_q \sum_k \frac{f_{k-q} - f_k}{\hbar\omega + i\delta + \epsilon(k-q) - \epsilon(k)} , \quad (2.20)$$

where f_k is the occupancy of an electronic state with wavevector k , such that

$$V_{eff}(q) = \frac{V_q}{\epsilon(\omega, k)} \quad (2.21)$$

Thomas-Fermi screening and Coulomb matrix elements

The evaluation of the Lindhardt formula 2.20 for the case of a degenerate semiconductor with one single conduction band yields the Thomas-Fermi screened Coulomb potential.

$$V_{eff,TF}(q) = V_q \frac{1}{1 + k_{TF}/q} = \frac{e^2}{2\epsilon_0 L^2} \frac{1}{q + k_{TF}} , \quad (2.22)$$

where the Thomas-Fermi screening wave-vector k_{TF} for a degenerate semiconductor is given by

$$k_{TF} = \frac{2}{a_0} , \quad (2.23)$$

with the Bohr radius a_0 .

In the case of TMDs, the Coulomb interaction has two contributions, the inter-valley scattering processes and the intra-valley processes. In typical gating, a Fermi wave-vector on the order of $k_F \approx 10^9 \text{ m}^{-1}$ is obtained at large densities. The Bohr radius of the exciton is $a_0 \approx 0.4 \text{ nm}$. The intra-valley Coulomb matrix elements can therefore be replaced by

$$V_{intra} \approx \frac{e^2}{2\epsilon_0 L^2} \frac{1}{k_{TF}} = \frac{e^2}{4\epsilon_0 L^2} a_0 = \frac{1}{L^2} \frac{\pi \hbar^2}{m_r} = \frac{1}{N\nu} , \quad (2.24)$$

where ν is the parabolic density of states in two-dimension and N is the number of bands [10]. On the other hand, the Thomas-Fermi wave-vector is small compared to the inter-valley scattering wave-vector K , so that we can simplify the inter-valley matrix elements with

$$V_{inter} \approx \frac{e^2}{2\epsilon_0 L^2} \frac{3a_{latt}}{4\pi} = \frac{1}{N\nu} \frac{3}{2\pi} \frac{a_{latt}}{a_0} \quad (2.25)$$

As the Bohr radius is almost as small as the unit cell in transition metal dichalcogenides, it turns out that inter-valley scattering are only ≈ 2 times weaker than intra-valley scattering. This is a property unique to transition metal dichalcogenides !

Bibliography

- [1] Liu, G.-B., Shan, W.-Y., Yao, Y., Yao, W. & Xiao, D. Three-band tight-binding model for monolayers of group-VIB transition metal dichalcogenides. *Phys. Rev. B* **89**, 039901 (2014).
- [2] Kormányos, A., Zoloyomi, V., Drummond, N. D. & Burkard, G. Spin-orbit coupling, quantum dots , and qubits in monolayer transition metal dichalcogenides. *Phys. Rev. X* **4**, 011034 (2014).
- [3] Kormanyos, A. *et al.* k.p theory for two-dimensional transition metal dichalcogenides semiconductors. *2d Mater.* **2**, 022001 (2015).
- [4] Yao, W., Xiao, D. & Niu, Q. Valley-dependent optoelectronics from inversion symmetry breaking. *Phys. Rev. B* **77**, 235406 (2008).
- [5] Xiao, D., Liu, G.-B., Feng, W., Xu, X. & Yao, W. Coupled spin and valley physics in monolayer of MoS₂ and other group-VI dichalcogenides. *Phys. Rev. Lett.* **108**, 196902 (2012).
- [6] Haug, H. & Koch, S. W. *Quantum Theory of the Optical and Electronic Properties of Semiconductors* (World Scientific, 2004), 4 edn.
- [7] Chernikov, A. *et al.* Exciton binding energy and nonhydrogenic Rydberg series in monolayer WS₂. *Phys. Rev. Lett.* **113**, 076802 (2014).
- [8] Scrace, T. *et al.* Magnetoluminescence and valley polarized state of a two-dimensional electron gas in WS₂ monolayers. *Nat. Nanotechnol.* **10**, 603 (2015).
- [9] Dery, H. Theory of intervalley Coulomb interactions in monolayer transition-metal dichalcogenides. *Phys. Rev. B* **94**, 075421 (2016).
- [10] Miserev, D., Klinovaja, J. & Loss, D. Spontaneous Symmetry Breaking in Monolayers of Transition Metal Dichalcogenides. *arXiv e-prints* arXiv:1902.07961 (2019). [arXiv:1902.07961](https://arxiv.org/abs/1902.07961).

Chapter 3

Methods

3.1 Sample fabrication

A great advantage of the van der Waals materials is that they can be easily combined with another material to add some functionality to a material. A stack of different van der Waals material is named a van der Waals heterostructure. All the samples discussed within this thesis are van der Waals heterostructures. The basic idea for building a van der Waals heterostructure is to stack layers of different materials which are 10 nm thick or less, down to atomic monolayers.

3.1.1 Exfoliation and identification of monolayers

Before stacking the different materials, one needs to prepare the layers. For this purpose, we use the basic property of van der Waals materials: they consist of weakly bound layers. Using scotch tape, we can tear off the first layers from a bulk crystal of a given material on a scotch tape. By folding the scotch tape a few times, we can spread fragments of the crystal on the whole surface of the scotch tape. The tape is then placed on a substrate, and when peeled off the substrate, a few pieces of the crystal decide to stay on the substrate. The method using scotch tape to isolate thin crystals on a substrate is often referred to as “mechanical exfoliation” in the literature. The thicknesses, sizes and shapes of the different layers left on the substrate can be characterized using different techniques, such as optical microscopy, Raman spectroscopy and AFM.

Fig. 3.1 shows in greater details the exfoliation technique that was used to produce the samples discussed within this thesis. (a) Bulk crystal (here, natural MoS₂); (b) we press the crystal on a scotch tape (Nitto tape) and (c) we remove the bulk of the crystal gently, leaving some material on the tape. (d) By folding the tape a few times, a large dense homogeneous area (d) of the tape is covered by the crystal. A reddish glare of the crystal indicates that the crystals on the tape are thin, a good prerequisite to obtain thin

Company	Product
Nitto (scotch tape)	ELP BT-150P-LC
Ultron Systems (scotch tape)	1005R-6.0
Gel-Pack (PDMS strip)	WF-25-X4

Table 3.1. References of the different exfoliation material used for exfoliation in the frame of this thesis.

Material	Type	Reference
MoS ₂	Natural	SPI Supplies
MoSe ₂	Synthetic	HQ Graphene
WSe ₂	Synthetic	HQ Graphene
Graphite	Natural	NGS Nanographit
h-BN	Synthetic	K. Watanabe & T. Taniguchi [1]

Table 3.2. References of the different bulk crystals used in the frame of this thesis.

layers on the substrate. (f) We press a strip of PDMS onto the scotch tape to transfer some flakes from the blue tape to the PDMS. This step is not necessary, but tends to reduce the amount of scotch tape residues on the final substrate. For increasing the exfoliation yield, the blue tape as well as the PDMS strip can be exposed for 2 minutes in a UVO cleaner before putting the two surfaces into contact. The contact between the two surfaces should hold for two minutes with a mild force (≈ 2 N). (g) We remove the PDMS from the tape and we place it on the substrate. As before, the contact should be held for around 2 minutes with a mild force. (h) When we peel the PDMS off the substrate, a few crystals are left on the chip. The purple colour of the chip comes from the 290 nm of silicon oxide grown on the silicon. (f) When looking at the chip with a x5 microscope objective, a lot of small crystal fragments can be seen. We are mostly interested into purple-blue-green thin crystals, as they are only a few monolayers thick. (g) With a 100x objective, we show a picture of a monolayer of MoS₂.

Optical contrast

As we are mostly looking for crystals of thicknesses of less than 10 nm, these crystals do not absorb and reflect white light significantly. They are therefore extremely difficult to see with an optical microscope on a general substrate. However, by choosing an appropriate wafer, one can create interference effects. Fig. 3.1(i) shows the surface of a SiO₂/Si substrate after exfoliation of molybdenum disulfide. When looking carefully (Fig. 3.1(j)), some crystals look blue/purple-transparent. This are the colours that we expect from thin crystals. In Fig. 3.1(j), one can see a monolayer of MoS₂. In the 2D

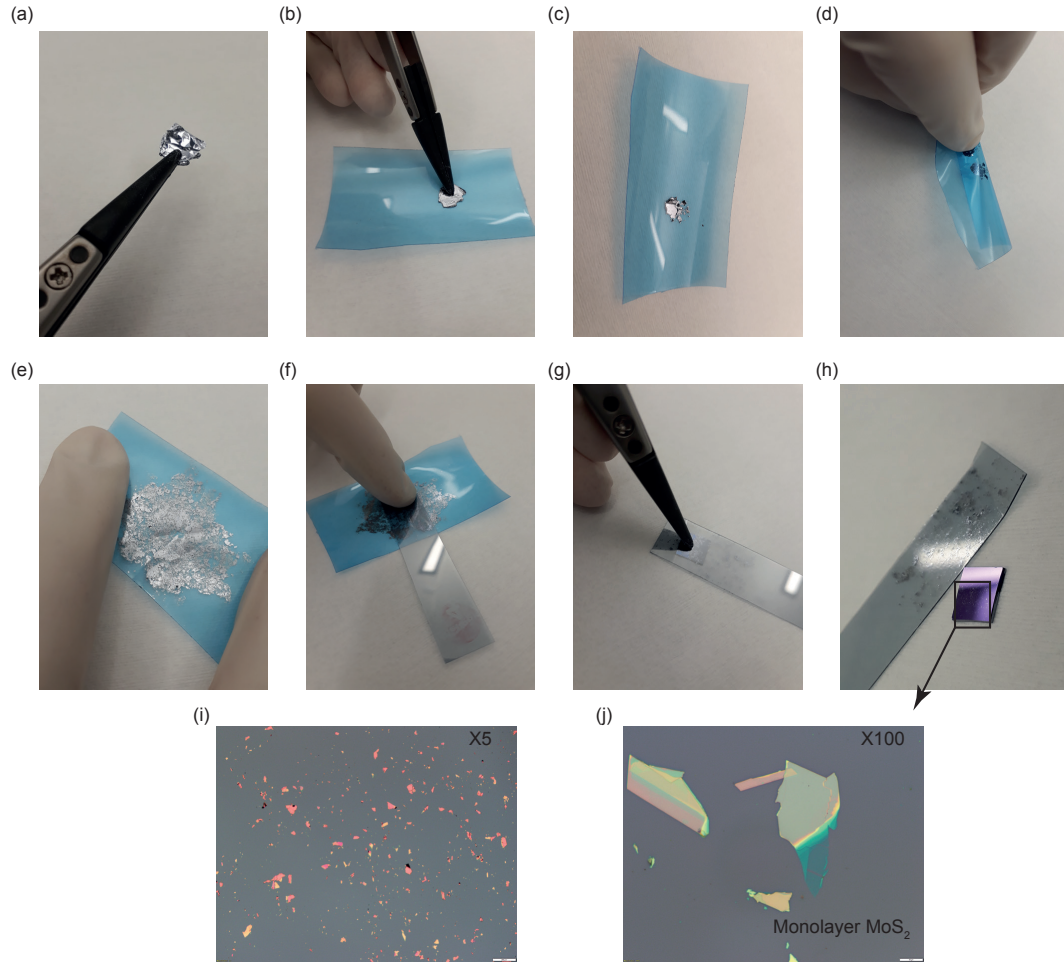


Fig. 3.1. Mechanical exfoliation process. A bulk crystal is exfoliated on a Si/SiO₂ substrate.

material community, a silicon wafer with a 290 nm thick layer of SiO₂ is often used as substrate. The first reason is that it is cheap and the second reason is that the 290 nm of oxide on the highly reflective silicon enhance the contrast obtained with a white light source when looking at few-layers thick crystals. An advantage of using silicon is the possibility to use heavily doped silicon wafers as bottom gates for the samples placed on the oxide surface.

Raman spectroscopy

Although a well-trained eye can easily spot monolayers by looking at them with an optical microscope, Raman spectroscopy can be used to determine the number of layers. When the thickness of the crystal varies, the interaction between the layers changes [2].

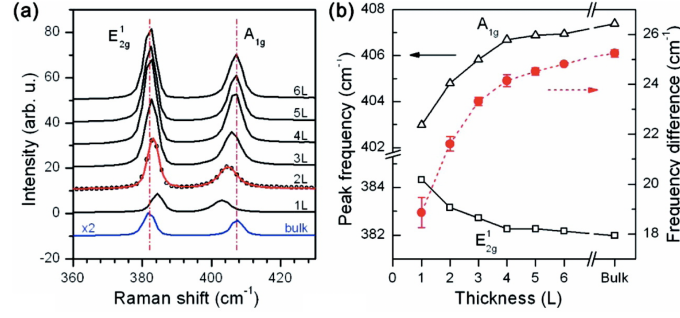


Fig. 3.2. The energy of in-plane (E_{2g}^1) and out of plane (A_{1g}) Raman modes changes with the number of layers in MoS_2 . (a) Raman spectra of a crystal of MoS_2 with different thicknesses given in monolayer (L) units. (b) Energy of the Raman peaks as a function of layer number. Image from Ref. [2].

Consequently, the Raman frequency of the out-of-plane phonon mode (A_{1g}) and the in-plane Raman mode (E_{2g}^1) shifts when the crystal becomes thinner. The energy difference between the two Raman modes can be used to identify monolayers accurately, as shown in Fig. 3.2

3.1.2 Building van der Waals heterostructures

To fabricate our van der Waals heterostructures, we use a dry-transfer technique [3]. This technique uses the fact that exfoliated flakes on a substrate are only loosely attached to the substrate. If we put in contact with the flake a stamp of a material that sticks more to the flakes than the flake sticks to the substrate, then the flake will come with the stamp when we peel it off. It turns out the van der Waals materials tend to stick better to most of the polymers (poly(methyl methacrylate), polydimethylsiloxane, polycarbonate...) than to SiO_2 .

We use a stamp made of 5 mm x 5 mm layer of thickness ≈ 3 mm of polydimethylsiloxane (PDMS) placed on a clean microscope slide. As PDMS residues are extremely hard to remove, we add a thin layer of polycarbonate (PC) on top of the PDMS stamp. The PC layer will be the layer in contact with the flakes of the heterostructure. In contrast to PDMS, PC can be simply dissolved in chloroform. Fig. 3.3 shows the different steps for the fabrication of a stamp and Table 3.3 shows the references of the different polymer materials we use for the dry transfer method.

In order to obtain a clean van der Waals heterostructure, it is important to build it quickly with freshly exfoliated material. Prior to starting the stacking of the different materials, the stamps and the different layers to be stacked should be already prepared. When we are ready, we can start by picking up the first layer of the van der Waals

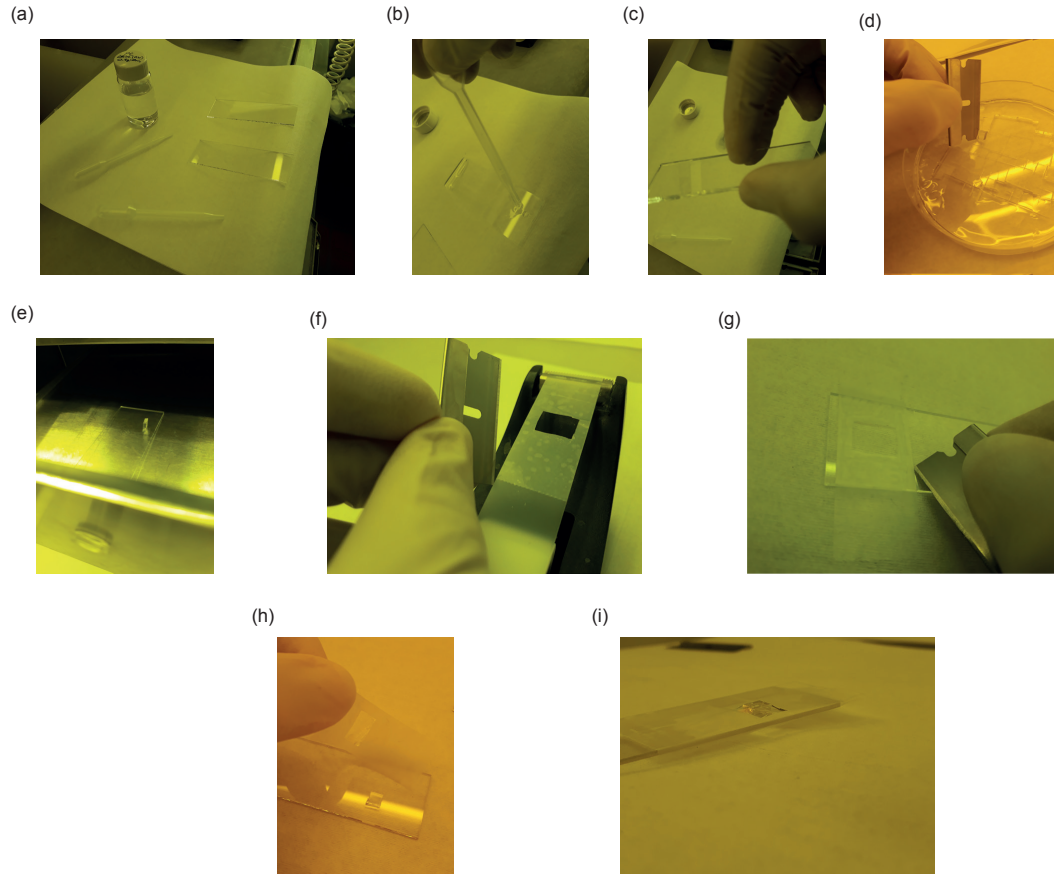


Fig. 3.3. Fabrication of the stamp. (a-c) Preparation of a thin PC film. A bit of liquid PC dissolved in chloroform is poured on a clean microscope glass slide and directly after, another glass slide is pressed onto it to create a homogeneous film. Slide the microscope glass slide to the side and let dry. A thin PC film is now ready on the two microscope glass slides. (e) Chop a little piece of PDMS and leave it standing on a clean microscope side in a UVO cleaner for 5 minutes (in d). Then, let the flat side of the PDMS touch the glass slide (as in h). (f-g) Prepare a window in a doubled piece of scotch tape with a cutter. The window should be larger than the PDMS piece. Stick it on the glass slide with the PC film and cut the PC at its sides with a cutter. (h) Peel slowly the scotch with the window from the glass slide. The thin PC film should normally stick to it. Place the scotch tape on the slide with the PDMS stamp such that the PC covers the PDMS. (i) Use more scotch tape to secure the PC film at its position. The stamp is ready.

Polymer	Company & product name	Mix & recipe
PC	Sigma-Aldrich, polycarbonate	0.8 g dissolved overnight in 20 mL chloroform
PDMS	Down Corning, sylgard 184, silicon elastomer	10 g (big bottle) mixed with 1 g (small bottle)

Table 3.3. References and recipes of the different polymers used for stamp fabrication.

heterostructure on the stamp. In this method, we pick up first the top layer of the stack. Fig. A.1 shows the whole process to obtain the samples discussed in chapter 5. The initial pick up works best if the first layer is a h-BN flake.

We use an optical microscope with a modified sample stage to stack our layers. The sample stage allows to move the chip with exfoliated material and the stamp independently, as shown in Fig. 3.4. The sample stage also has a heater that we will use in the last step to melt the PC layer.

For picking up the first layer, we centre the flake in the centre of the field of view of the microscope and then place the stamp on the stamp positioning stage a few millimeters above the surface of the sample. We ensure that the stamp is also centred with the field of view of the microscope. We can then lower the stamp. The stamp should not be completely parallel to the surface of the sample. A few degrees angle between the chip and the stamp will help for stacking as the contact will happen at a slower pace. When the stamp is in contact with the chip, a change in colour can be seen through the microscope. Place the contact line (see Fig. 3.4) after the flake. The sample stage should then be heated to 85°C. With heat, the PDMS stamp expands. The height of the stamp should be adjusted during the heating to always keep the contact line a few tens of micrometer past the flake. When the stage is at 85°C, we turn the heater off and as the PDMS retracts slowly, the flake will be gently peeled off from the substrate.

When the stamp retracted enough that the flake sticks completely to the stamp, the stamp positioning stage can be elevated until the stamp is not in contact with the chip anymore. We remove the first chip and we can place on the sample stage the chip with the next layer to stack. Again, the second layer should be placed in the centre of the field of view of the microscope. The stamp should be then aligned with the flake on the substrate such that the two layers to stack overlap. While coming into contact, always check that the two layers always stay aligned. Once in contact, we can again heat the stage to 85°C and repeat the steps mentioned before until the layer before last.

The last layer will stay on its substrate and it is the rest of the stack that will be deposited onto it. Usually, the substrate of the last layer contains some alignment marks for electron-beam lithography. These marks tend to make the pick up of layers difficult, so only the last layer is exfoliated on such a substrate. The stamp now contains all the layers except the last one, that is on the substrate with markers. As always, we align the full stack on the stamp with the last layer, come into contact and then we lower the stage until the whole surface of the chip is in contact with the stamp. We heat then the sample stage to 190°C in order to melt the PC layer. We can then remove slowly the PDMS stamp. The stack with the PC layer on top should stay on the substrate. Afterwards,

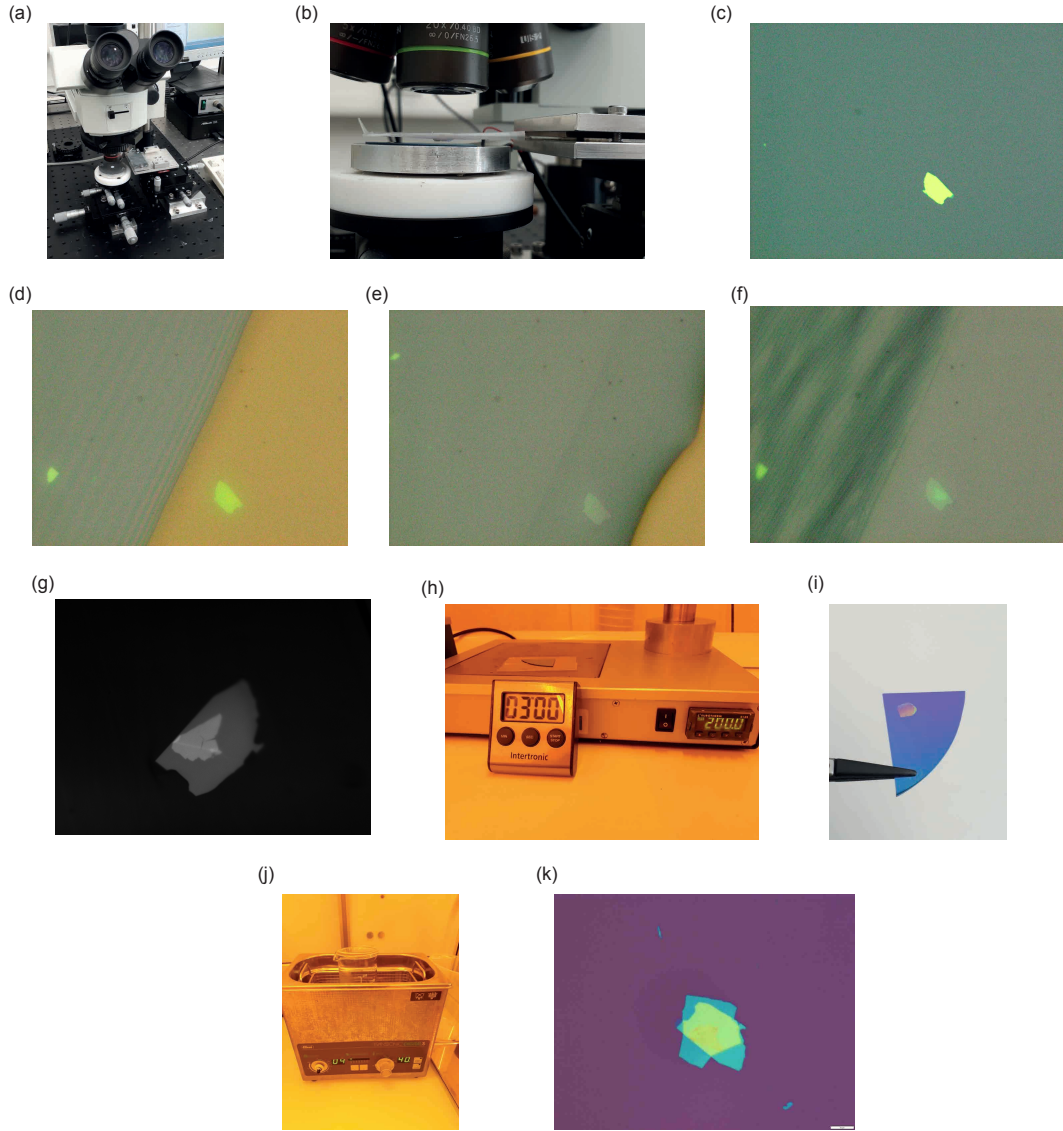


Fig. 3.4. (a) Stacking stage. Two independent positioning stages allow for moving both the sample and the substrate. (b) We place the chip on the stage and we centre the stamp such that the microscope light goes through the PDMS. We ensure that the stamp and the substrate are slightly not parallel. (c) We localise the flake to be picked up through the stamp by moving the sample stage. (d) As we go down with the stamp, we start to see the contact line. We place it next to the stamp, heat up to 85° and then turn off the heater. (e) When the PDMS cools down, it retracts slowly and the flake will stick to the PC film. (A change in colour of the flake can be noticed between (c) and (e)). (f) We go up with the stamp, place the substrate with the next layer under the microscope and align the two layers. We can see the next layer in light blue in the middle of the first flake. (g) We pick up the flake similarly as in (d+e) and we can see that the second flake has been successfully picked up. We repeat this step until the end, when we heat up the stage to 190° . At this temperature, the PC melts and we can remove the PDMS only. Then, place the substrate with the stack on a hot plate for 3 minutes at 200° , as in (h). (j) We can see the melted PC on the substrate. (i) We remove the PC by leaving the substrate in chloroform at 40° for several hours. (k) A three layers stack is finished.

the substrate should be placed on a hotplate at 200°C for 3 minutes to ensure that the PC is completely melted. The PC is then dissolved in chloroform at 40°C for a couple of hours. If the stack still looks good when coming out of the chloroform, congratulations: the stack is now ready!

3.1.3 Electrical contacts to Van der Waals heterostructure

In the frame of this thesis, we investigated two types of contacts: few layers graphite and metallic contact. While we haven't characterised the quality of our contacts with transport measurements, they were generally good enough for gating.

Metallic contacts

There are two ways of contacting a specific layer within a van der Waals heterostructure: either the layer can be accessed from the top and electron beam lithography can be performed once the stack is finished, or the layer is too small and the contacts must be made during the middle of the stacking process.

In the case where we can print the contacts once the stack is finished, we have usually used Ti (5 nm)/Au (45 nm) or Cr (5 nm)/Au (45 nm) as contacts. It was, however, shown that the best contacts to semiconducting monolayers are obtained with the dual-gating scheme: two contacts are made on top of each other, but are insulated by a h-BN flake. The lower contact touches the layer while the top contact serves as a local gate. The contact area near the middle contact can then be locally doped by field-effect by the top contact. The dual-gating scheme has allowed recently the measurement of extremely clean Shubnikov de Haas oscillations in monolayer MoS₂, where an ohmic resistance of 25 kΩ was achieved [4]. Note that the contact resistances tend to decrease significantly when the sample is annealed for more than 12 hours in vacuum at 100°C.

FLG contacts

Another way of contacting a layer within a van der Waals heterostructure is to use a few layers of graphite or graphene (FLG) to contact the layer. The use of FLG as a contact ensures that the surface between the FLG electrode and the flake to be contacted is clean. The FLG flake can be contacted easily from the top using metallic Ti (5 nm)/Au (45 nm) or Cr (5 nm)/Au (45 nm) contacts defined by electron beam lithography.

3.2 Optical characterisation setup

In this thesis, two types of optical measurements were carried out: photoluminescence and reflectivity measurements. In a photoluminescence experiment, photons of energy higher than the exciton energy are used to excite the sample and the light emitted by the sample is collected at lower energy. In a reflectivity experiment, white light is sent on our sample and reflected light is collected. Although the two methods seem quite similar in practice (light-in, light-out), the information they provide is extremely different.

In order to understand the difference between absorption and photoluminescence, we could think of the difference between a guitar and a harp. Let us focus on one specific note, for instance a the low E (82.41 Hz) of a guitar. In a reflectivity experiment, we would fix firmly one extremity of the string and drive the other extremity with a small amplitude at various frequencies (see for instance <https://www.youtube.com/watch?v=BSIw5SgUirg>). As the frequency sweeps, we would find that the guitar string would absorb energy at $n \times 82.42$ Hz, $n = 1, 2, \dots$. These are the eigenmodes of the string. The same eigenmodes would be found if we were to use the harp string. The equivalent of the photoluminescence experiment would be to hit quickly the string with the fingers. When we hit the cord with the fingers swiftly, the Fourier spectrum of the sound is different whether we use a guitar or a harp. The reason is that the relaxation mechanisms toward the lowest energy eigenmode are different in these two instruments.

In an absorption measurement, we excite the sample at different energies and we see when the material can absorb energy. The absorption spectrum comes from changes in the dielectric function in the material and it is an intrinsic property of the material. On the other hand, in photoluminescence spectroscopy, we excite the material with energy and we see how it relaxes toward its ground-state. From the example above, we understand that we learn very different information about the system when we perform a photoluminescence (PL) measurement and an absorption measurement.

Our optical setup is modular and allows for room-temperature or cryogenic temperature (4.2 K) characterisation of our samples. The setup can be split into three parts: the microscope head, the microscope skeleton and the sample holder, as shown in Fig. 3.5

The sample holder consists of a titanium housing that holds a microscope objective or an aspherical lens, a set of x-, y-, z-piezo nano-positionners (Attocube steppers, Premium series), a sample holder with 24 electrical lines for contacting the sample (if needed) and a small heater and thermometer for monitoring the sample's temperature.

The microscope skeleton consists simply of a cage made from three or four non-magnetic stainless steel rods that make the link between room temperature and cryogenic

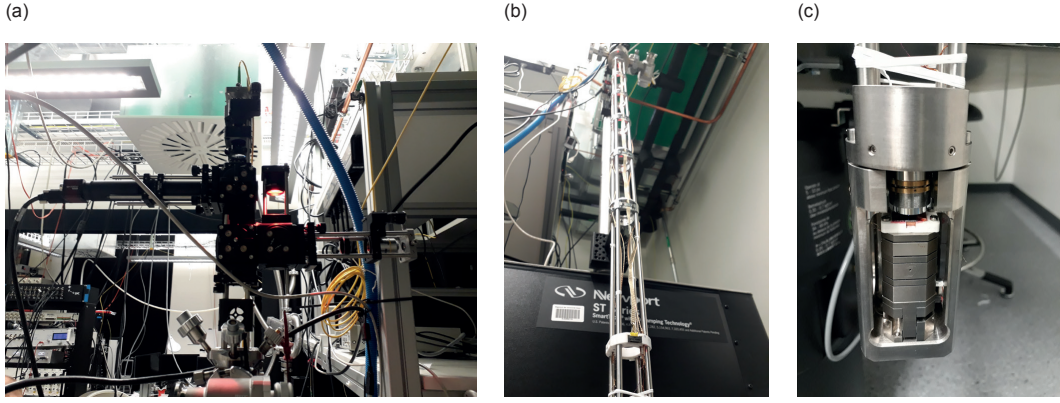


Fig. 3.5. The setup consists of three components: (a) the microscope head (b) the skeleton and (c) the sample holder.

temperature. The length of the cage is designed such that our sample sits in the center of the magnetic field in our cryostat systems. For quick room temperature characterisation, the microscope skeleton can be omitted.

The modularity of our setups is best illustrated with the concept of the microscope head. A microscope head is in itself an optical setup that can be placed on the microscope skeleton. We have two different microscope head designs used in this thesis: a photoluminescence head and an absorption head. We can change the type of measurement by changing the design of the head. The two designs are optimised for the one or the other application, but have the following in common: a camera with a red LED are used for sample positioning, an out-coupler brings light from a light source (laser or LED...) to the sample via a fibre, and an in-coupler brings the light resulting from the experiment (photoluminescence or reflected light...) into a fibre that is connected to a spectrometer.

3.2.1 Photoluminescence measurement

The photoluminescence measurements presented into this Thesis were performed using an orange (594 nm, 2.09 eV) HeNe laser or a red HeNe laser (633 nm, 1.96 eV). The laser light is coupled into an optical single-mode fiber (Thorlabs, HP630) in order to be sent to the microscope head. The use of a single-mode fiber has the advantage of performing a mode filtering of the light in the fiber. Fig. 3.6 shows the optical design of the microscope head. A laser clean-up filter removes the fibre luminescence and leaves spectrally pure laser light in the microscope head. The light passes then through a linear polariser followed by a liquid crystal variable retarder that is here used as a $+\lambda/2 \leftrightarrow$

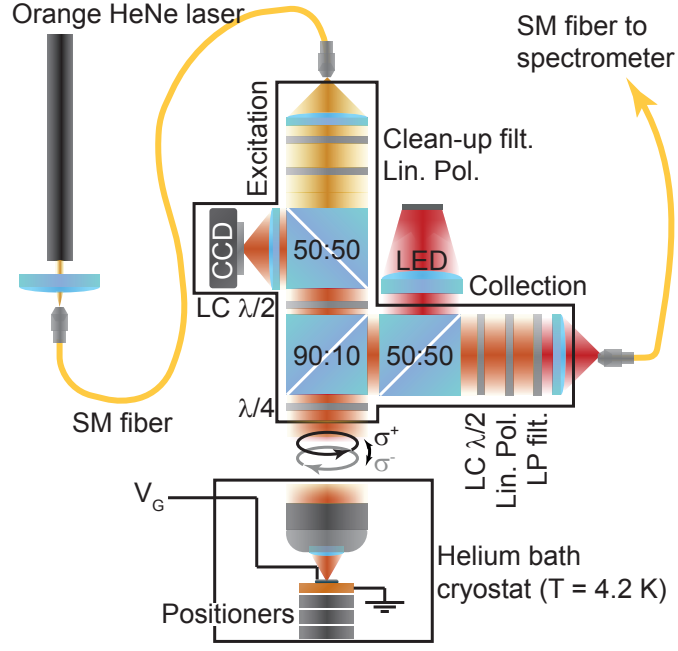


Fig. 3.6. Design of the photoluminescence microscope head.

$-\lambda/2$, such that when the light reaches the $\lambda/4$ waveplate, we can electronically switch from a left-handed circular polarisation to a right-handed polarisation. The light then reaches the microscope objective (or the lens) and is focussed onto the sample. The emitted light is collected by the objective and goes through the $\lambda/4$ and 90% is sent into the collection arm. The polarisation selection occurs by going through the $\lambda/2$ and linear polariser combination. After spectral filtering, we filter out the reflected laser light with a long-pass filter.

In order to locate the samples, we can turn on a red LED on the microscope head. The 50:50 beamsplitter right under the LED can be removed during measurements in order to limit the light losses in the collection arm. The LED light disperse light on a large area on the sample and the reflected light is partially sent to a CCD camera.

3.2.2 Absorption measurement

The microscope head, depicted in Fig. 3.7 for the absorption measurement is quite similar to the PL head (Fig. 3.6). When we measure absorption, we use a white LED coupled into our microscope head with a multimode fibre. The use of a multimode fibre is con-

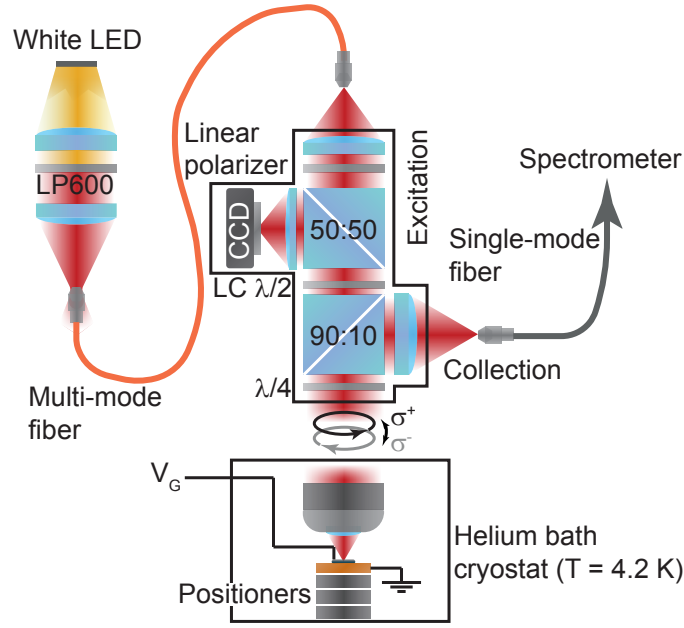


Fig. 3.7. Design of the absorption microscope head.

venient, as it disperses the light onto a large area on the sample, allowing the sample to be observed on the camera without need for an extra LED, as in PL. We collect the light from a diffraction limited small spot with the use of a single-mode fibre for collection of the reflected light. For reflectivity measurement, we do not need to filter out the polarisation of the collected light.

The big problem in an absorption measurement is that, as the signal is broadband, etaloning becomes a problem. Etaloning is caused by optical interferences within the CCD chip. In order to limit etaloning, defocussing the light at the input of the spectrometer helps, as it spreads the light over a large area of the CCD chip, averaging out etalon effects.

In Appendix A.3, we will discuss how we can deduce the imaginary part of the optical susceptibility from the reflectivity spectrum by using the Kramers-Kronig relations.

Bibliography

- [1] Taniguchi, T. & Watanabe, K. Synthesis of high-purity boron nitride single crystals under high pressure by using Ba–BN solvent. *J. Cryst. Growth* **303**, 525–529 (2007).
- [2] Lee, C. *et al.* Anomalous lattice vibrations of single- and few-layer MoS₂. *ACS Nano* **4**, 2695 (2010).
- [3] Zomer, P., Guimarães, M., Brant, J., Tombros, N. & Van Wees, B. Fast pick up technique for high quality heterostructures of bilayer graphene and hexagonal boron nitride. *Appl. Phys. Lett.* **105**, 013101 (2014).
- [4] Pisoni, R. *et al.* Interactions and magnetotransport through spin-valley coupled Landau levels in monolayer MoS₂. *Phys. Rev. Lett.* **121**, 247701 (2018).

Chapter 4

Quantum-Confined Stark Effect in a MoS₂ Monolayer van der Waals Heterostructure

Adapted from: Jonas Gaël Roch, Nadine Leisgang, Guillaume Froehlicher, Peter Makk, Kenji Watanabe, Takashi Taniguchi, Christian Schönenberger, and Richard John Warburton,

“Quantum-Confined Stark Effect in a MoS₂ Monolayer van der Waals Heterostructure”,

Nano Lett., **18** (2), 1070-1074 (2018)

The optics of dangling-bond-free van der Waals heterostructures containing transition metal dichalcogenides are dominated by excitons. A crucial property of a confined exciton is the quantum confined Stark effect (QCSE). Here, such a heterostructure is used to probe the QCSE by applying a uniform vertical electric field across a molybdenum disulfide (MoS₂) monolayer. The photoluminescence emission energies of the neutral and charged excitons shift quadratically with the applied electric field provided the electron density remains constant, demonstrating that the exciton can be polarized. Stark shifts corresponding to about half the homogeneous linewidth were achieved. Neutral and charged exciton polarizabilities of $(7.8 \pm 1.0) \times 10^{-10} \text{ D m V}^{-1}$ and $(6.4 \pm 0.9) \times 10^{-10} \text{ D m V}^{-1}$ at relatively low electron density ($\approx 10^{12} \text{ cm}^{-2}$) have been extracted, respectively. These values are one order of magnitude lower than the previously reported values, but in line with theoretical calculations. The methodology presented here is versatile and can be applied to other semiconducting layered materials.

4.1 Introduction

The recent emergence of optically-active layered semiconductors [1, 2], such as molybdenum disulfide (MoS_2), and of the so-called van der Waals heterostructures (vdWhs) [3, 4] pave the way towards engineered quantum structures. Excitons in MoS_2 and other transition metal dichalcogenides have particularly large exciton binding energies [5] such that excitons dominate the optical properties, even at room temperature. Therefore, the fundamental properties of the excitons need to be elucidated. A basic feature of semiconductor nanostructures is the quantum confined Stark effect (QCSE), the change in optical response on applying an electric field perpendicular to the layers [6]. On the one hand, the QCSE characterizes the sensitivity of the exciton energy to charge noise as charge noise results in a fluctuating electric field within the device. The QCSE is therefore important in optimizing and understanding optical linewidths. On the other hand, the QCSE can be exploited to trap and manipulate excitons on the nano-scale by applying a locally varying vertical electric field [7, 8].

When a DC electric field is applied perpendicular to a MoS_2 monolayer (z -axis), electrons and holes will tend to move apart in order to decrease their electrostatic potential energy. The resulting energy shift ΔE of the exciton energy is known as the QCSE and is given by $\Delta E = -\mu_z F_z - \beta_z F_z^2$ where F_z is the component of the electric field, μ_z the excitonic dipole moment and β_z the excitonic polarizability along the z -direction. Owing to the reflection symmetry about the molybdenum plane, $\mu_z = 0$ in a MoS_2 monolayer embedded in a symmetric dielectric environment [9] such that the QCSE is expected to be quadratic in F_z .

Measurement of the Stark shift of the A-exciton in a MoS_2 monolayer has been reported [10]. However, the experiment was performed on monolayers encapsulated in standard oxides (aluminium and silicon oxides) which have poor optical quality and, most probably, contain a significant density of charge traps [11]. Lately, a theoretical study [12] has predicted β_z to be more than one order of magnitude below the reported experimental value. An unambiguous measure of the QCSE in MoS_2 is therefore missing. A particular challenge is that the exciton energies depend strongly on the electron density in the MoS_2 monolayer [13]. Furthermore, the description of the optical excitations in the high-density regime has a strong many-electron flavor: the quasi-particles are no longer the simple excitons [14, 15]. These considerations mean that the QCSE should be measured at a low and constant electron density.

In this Letter, high quality MoS_2 monolayers, obtained by encapsulation in hexagonal boron nitride (h-BN), are used to determine precisely the QCSE of the neutral X^0

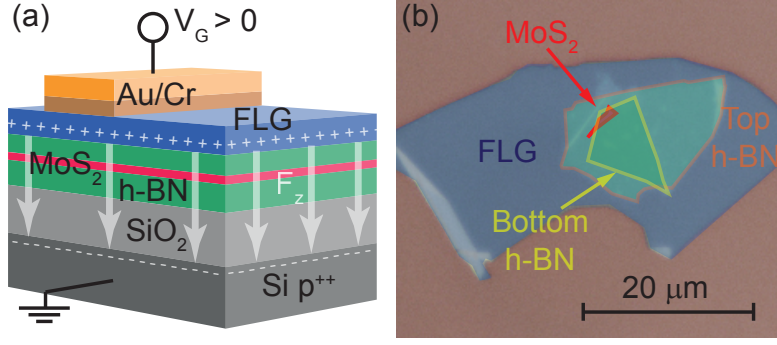


Fig. 4.1. (a) Three-dimensional schematic view of the device used to measure the quantum confined Stark effect. The device consists of a MoS₂ monolayer sandwiched between two layers of h-BN and covered by a few-layer graphene (FLG) top electrode, deposited onto a highly *p*-doped Si/SiO₂ substrate. A voltage V_G is applied between the Si substrate and the top electrode to create a uniform electric field across the MoS₂. (b) Optical micrograph of the device. The different layers have been artificially highlighted with colors. Photoluminescence is carried out on the part of the MoS₂ monolayer which is fully encapsulated in h-BN.

and negatively charged X^- A-excitons. The photoluminescence (PL) spectra of these samples show narrow linewidths (≈ 8 meV), close to the ideal limit ($1 - 2$ meV [16]), allowing the X^0 and X^- to be identified unambiguously. Both spectral features shift when applying an electric field. However, at the same time, the ratio between the integrated intensities of X^- and X^0 varies. The change in this ratio signifies a change in the electron density which, in turn, shifts the emission energies. To separate carefully QCSE and doping contributions to the energy shifts, additional measurements were performed on a directly contacted MoS₂ device. These measurements quantify precisely both the X^- to X^0 intensity ratio and the exciton energy shifts as a function of the electron density. We use this information to find a region in the encapsulated device where the electric field can be changed at a constant and relatively low electron density. In this region, we demonstrate a clear QCSE. We determine excitonic polarizabilities typically one order of magnitude smaller than the values reported in Ref. [10] but in good agreement with calculations in Ref. [12].

4.2 Device and device characterization

The QCSE was measured using the encapsulated device with geometry as depicted in Fig. 4.1(a): two thick h-BN layers are used as dielectric spacers and the top few-layer graphene (FLG) acts as a transparent electrode (see Methods for a description of the

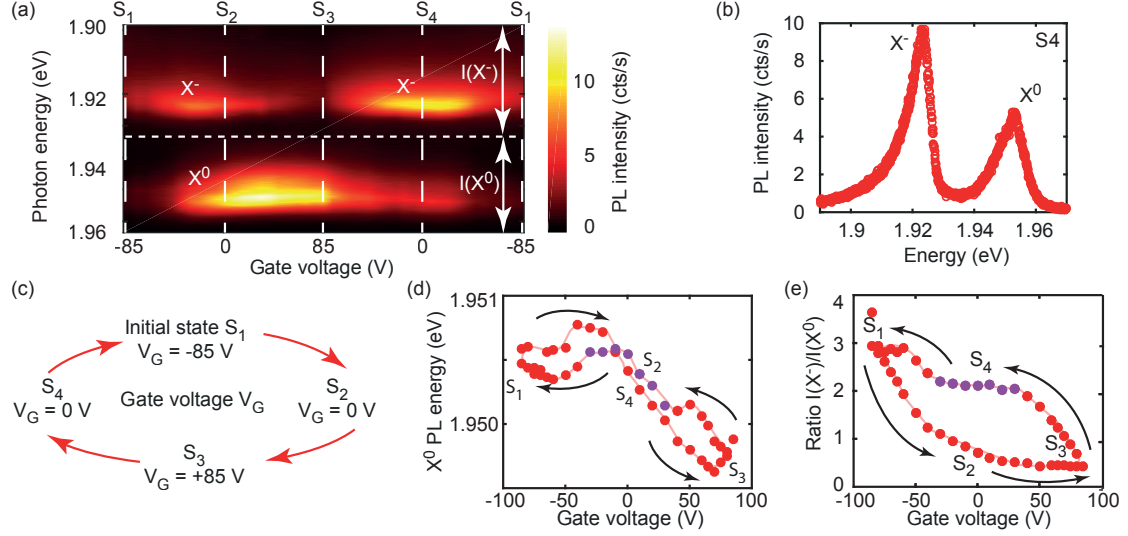


Fig. 4.2. (a) Colormap of the photoluminescence spectra of MoS₂ as a function of V_G . The neutral X⁰ and negatively charged X⁻ excitons and the four states defined in (c) are labeled. (b) Typical photoluminescence spectrum recorded at S₄. (c) The gate voltage V_G in the device was varied along a loop from state S₁ (−85 V) to S₃ (+85 V) and back, reaching $V_G = 0$ twice (states S₂ and S₄). (d) Emission energy of X⁰ as a function of V_G . The experimental data points extracted from the spectra in (b) are represented by circles where the purple circles correspond to the data used to measure the Stark shift. The solid line is a guide to the eye and the black arrows indicate the changes made to V_G . (e) Ratio between the integrated intensity of the X⁻ and X⁰ features extracted from the data in (a) as a function of V_G . The range of integration is indicated by the white double-headed arrows in (a).

fabrication process). Applying a DC voltage V_G between the FLG and the highly doped bottom Si substrate creates a uniform electric field in the MoS₂ monolayer, oriented perpendicular to the basal plane of the sample. PL spectra were recorded at 4 K as a function of V_G in a home-built confocal microscope (see Methods).

Figure 4.2(a) shows typical PL spectra recorded over a voltage loop as illustrated in Fig. 4.2(c): V_G varies from the initial state (S₁) at −85 V to +85 V (S₃) via S₂ (0 V) and then back to S₁ via S₄ (0 V). Two prominent features can be clearly identified (see Fig. 4.2(b)): a low-energy peak near 1.92 eV and a high-energy peak near 1.95 eV attributed to the negatively charged X⁻ and the neutral X⁰ A-excitons [16, 17], respectively. The emission energies of X⁻ and X⁰ change with V_G , as seen in Fig. 4.2(d) where the X⁰ energy has been plotted. However, as demonstrated in the colormap in Fig. 4.2(a), the intensities of the X⁻ and X⁰ features also vary with V_G . The ratio between the integrated PL intensities of X⁻ and X⁰, $I(X^-)/I(X^0)$ (Fig. 4.2(e)), cannot be explained by the QCSE as it depends on the gate voltage sweep direction. Instead,

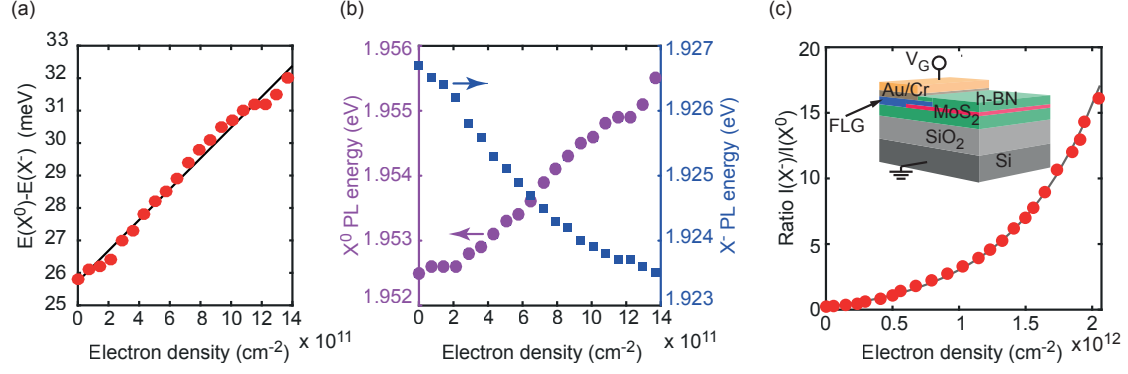


Fig. 4.3. Directly contacted MoS₂ device (reference sample). (a) Separation between the emission energy of the neutral $E(X^0)$ and negatively charged $E(X^-)$ excitons as a function of the electron density in the MoS₂ monolayer. (b) Variation of the photoluminescence energy of X^0 (purple circles, left axis) and X^- (blue squares, right axis) as a function of the electron density. (c) Ratio between the integrated intensity of the X^- and X^0 photoluminescence features as a function of the electron density. Inset: three-dimensional schematic view of the device. The MoS₂ is contacted at one side by a few-layer graphene electrode.

the change in relative intensity arises from a change in the electron density [18]. The noticeable hysteresis appearing in Fig. 4.2 (d) and Fig. 4.2 (e) reflects the fact that the electron density depends on the direction of the voltage sweep. The hysteresis, not the focus of the present investigation, arises as a combined consequence of photodoping effects [19, 20], tunneling [21] from the FLG top gate through the insulating h-BN top layer, and, possibly, charge trapping [22] at the SiO₂/h-BN interface.

4.3 Measurement of the Stark shift at low electron concentration

In order to monitor the electron density and its relation to $I(X^-)/I(X^0)$, a reference sample consisting of an encapsulated yet contacted MoS₂ monolayer was fabricated as sketched in the inset to Fig. 4.3(c). In this case, the MoS₂ layer is directly contacted by a few-layer graphene sheet. This is a capacitive device and as such the electron density in the sample is expected to change linearly with the applied gate voltage [17]. This expectation was confirmed experimentally by measuring the energetic separation between the X^0 and X^- features in the PL spectra: we find a linear dependence of the X^0 and X^- energy separation with gate voltage (see Fig. 4.3(a)). At low electron densities, the energetic separation between X^0 and X^- scales linearly with the Fermi level, as

ionization of X^- requires that an electron is moved up to the Fermi level [17, 23]. Given the linear dependence of Fermi energy on electron density for a two-dimensional system, the PL itself demonstrates that the reference sample charges as a capacitive device (with a capacitance $\approx 12 \text{ nF cm}^{-2}$). It is noteworthy that the X^0 and X^- emission energies show opposite dependences on the electron density (Fig. 4.3(b)): X^0 blue-shifts while X^- red-shifts with increasing electron density [13]. As in the main sample, the reference sample shows hysteresis effects on ramping the voltage up and down. The voltage at which the electron density is close to zero changes depending on the history of the device. Despite this, we find a robust relationship between the intensity ratio $I(X^-)/I(X^0)$ and the X^0 , X^- splitting, equivalently the electron density. Fig. 4.3(c) plots $I(X^-)/I(X^0)$ as a function of the electron density extracted from the PL spectra recorded at various gate voltages on the reference sample. The monotonic increase of this ratio with the electron density can be well described by a phenomenological exponential fit. This means that the ratio $I(X^-)/I(X^0)$ provides a highly sensitive tool to monitor any changes in the electron density. Of course, spatial inhomogeneities and sample-to-sample variations [16, 24] may also influence $I(X^-)/I(X^0)$ but for a particular location on a particular sample, this ratio is a very useful probe of the electron density. We exploit this feature but determine the absolute electron density from the energetic difference $E(X^0) - E(X^-)$ as this is a robust quantity without the sample-to-sample variations.

We return to the main sample. Using the energetic difference $E(X^0) - E(X^-)$ along the voltage loop displayed in Fig. 4.2(c), we find a total variation of the electron density of $\sim 10^{12} \text{ cm}^{-2}$. In order to isolate the QCSE contribution to the exciton energy, it is important to identify regions where the gate voltage can be swept without changing the ratio $I(X^-)/I(X^0)$, which, as explained above, is extremely sensitive to changes in the electron density. Inspection of the $I(X^-)/I(X^0)$ data in Fig. 4.2(e) shows that there are no significant changes in MoS_2 electron density around S_3 and S_4 . These two regions are therefore good candidates for measuring the QCSE in MoS_2 .

Between S_2 and S_3 , the ratio $I(X^-)/I(X^0)$ is small and corresponds to a region where MoS_2 has a low electron density ($\lesssim 10^{12} \text{ cm}^{-2}$). In this region, the X^- signal is weak and evaluation of the ratio $I(X^-)/I(X^0)$ becomes unreliable. It is therefore difficult to attest that the Fermi level in this region remains absolutely constant. Moreover, it is in this range of Fermi energy that photo-induced doping from the h-BN layers occurs leaving charged defects in the h-BN that potentially induce electric field screening [19]. The region around S_3 is therefore problematic with regards to the QCSE. The region around S_4 , between +30 V and -30 V, exhibits a stronger X^- feature and the ratio $I(X^-)/I(X^0)$ can therefore be reliably measured. From this ratio, the electron density is evaluated

to remain constant to within 5%. Using the energetic difference $E(X^0) - E(X^-)$, the electron density is estimated to be of $(1.5 \pm 1.0) \times 10^{12} \text{ cm}^{-2}$. The large uncertainty arises through spatial inhomogeneities in $E(X^0) - E(X^-)$, a feature of both the main and reference samples.

Fig. 4.4 displays the change in X^- and X^0 emission energies, $\Delta E(X^-)$ and $\Delta E(X^0)$ respectively, in the region around S_4 . F_z was determined by dividing V_G by the electrode-to-electrode distance of 300 nm and adding a constant built-in electric field of 0.66 MV/cm. This value was chosen such that $\Delta E(X^-)$ and $\Delta E(X^0)$ vanish at $F_z = 0$, i.e. it is assumed that $\mu_z = 0$. This built-in electric field arises from space charge within the layers of the heterostructure. Both $\Delta E(X^-)$ and $\Delta E(X^0)$ exhibit a quadratic dependence on F_z , equivalently a linear dependence on F_z^2 , as shown in Fig. 4.4. This is the signature of a QCSE. We argue that the experiment reveals a QCSE and not a residual effect of any small changes in electron density. First, for each point the measurement error in $I(X^-)/I(X^0)$ results in an electron density variation which leads to possible changes in $\Delta E(X^-)$ and $\Delta E(X^0)$ even without a QCSE. However, these changes (shown by the error bars in Fig. 4.4) are considerably smaller than the $\Delta E(X^-)$ and $\Delta E(X^0)$ values observed experimentally: the uncertainties in electron density cannot account for the shifts in X^- and X^0 emission energies. Second, both X^0 and X^- red-shift around S_4 yet a change in electron density would result in $\Delta E(X^-)$ and $\Delta E(X^0)$ values of opposite sign (see Fig. 4.3(b)). (Note that X^0 and X^- are measured simultaneously.) From a fit to a second order polynomial, $\Delta E(X^-)$ and $\Delta E(X^0)$ versus F_z , excitonic polarizabilities of $\beta_z(X^-) = (6.4 \pm 0.9) \times 10^{-10} \text{ D m V}^{-1}$ and $\beta_z(X^0) = (7.8 \pm 1.0) \times 10^{-10} \text{ D m V}^{-1}$ are deduced at an electron density of $(1.5 \pm 1.0) \times 10^{12} \text{ cm}^{-2}$. These values are nearly one order of magnitude lower than the previously reported values [10].

It is striking that the polarizabilities of the neutral and charged excitons are almost the same yet the emission energies are quite different on account of the different Coulomb interactions. The experiment itself therefore implies that Coulomb interactions in the excitons, equivalently screening by the electron gas, is unimportant in determining the QCSE. This in turn allows us to compare the experimental result to a single-particle theory. The excitonic polarizabilities have been theoretically calculated with a finite barrier quantum well model [12]. Using barriers of 2.8 eV [21] for both electron and hole, a quantum well thickness of 0.65 nm and effective electron and hole masses of 0.35 bare electron mass [17], an exciton polarizability of $7.5 \times 10^{-10} \text{ D m V}^{-1}$ is deduced. This is in good agreement with the experimental values reported here and strengthens the claim that the measured QCSE is dominated by single-particle energy shifts. This point can be understood by considering the highly anisotropic nature of the confinement.

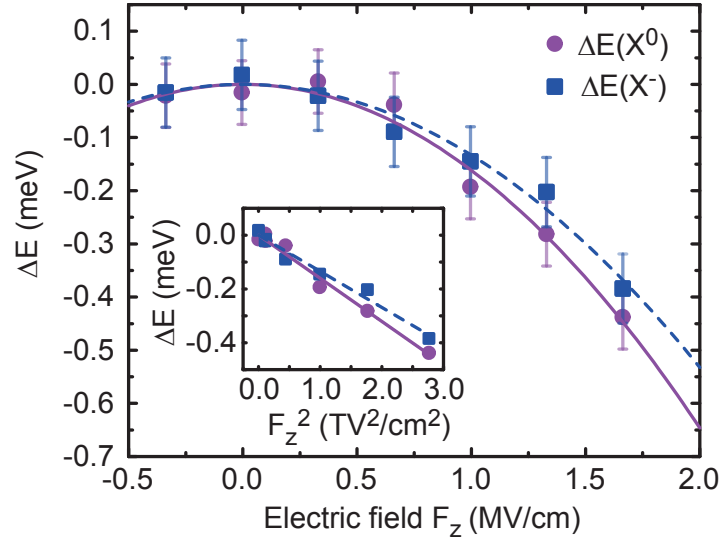


Fig. 4.4. Neutral X^0 (purple circles) and negatively charged X^- (blue squares) Stark shift as a function of the applied electric field F_z , extracted from the measurements in Fig. 4.2. The solid purple and dashed blue lines are parabolic fits. The inset shows the same data points as a function of the squared electric field F_z^2 in order to highlight the quadratic dependence of the Stark shift.

In the vertical direction, the confinement is dominated by single particle effects, i.e. confinement in a deep potential well. In the lateral direction, the exciton is much more polarizable [12, 25].

In detail, the experiment shows that the trion is slightly less polarizable than the neutral exciton, Fig. 4.4. This can be explained, at least qualitatively, by a subtle change in the Coulomb interactions. Specifically, in the X^- complex there is an additional decrease in the exciton binding energy with electric field. This is induced by the localization of the two electrons on one side of the monolayer and the hole on the other side, increasing the electron-electron repulsion, decreasing the electron-hole interaction [26], thus leading to a decrease in the trion binding energy. We measure here the polarizability at a rather low electron density where the conventional excitonic picture is valid [14, 15]. The transition to a many-body description occurs at higher electron densities than those used here and it is an open question to what extent the many-body interactions, screening and so on, cause a departure from the single-particle QCSE.

4.4 Conclusion

In conclusion, the QCSE of excitons has been extracted from photoluminescence measurements on a high quality MoS₂ monolayer embedded in a vdWh. As the electron density in the monolayer is observed to vary with electric field, a careful data analysis exploiting reference measurements on a directly contacted MoS₂ device was performed. Regions were identified in which the electron density in the monolayer remains constant as the electric field is varied. Having ruled out any contribution of a changing electron density to the exciton energy shift, a QCSE was unambiguously identified. The small exciton polarizability is in line with theoretical computation [12]. The maximum QCSE achieved here corresponds to just half the homogeneous linewidth despite the fact that large electric fields were applied. The insensitivity of the exciton to an electric field in MoS₂ has profound implications on its optical properties. On the one hand, we believe that the minute QCSE renders the exciton energy insensitive to charge noise. This, along with the super-fast radiative decay, explains the observation of optical linewidths close to the homogeneous limit in MoS₂ vdWhs [16]. On the other hand, electrical control of the exciton based on the QCSE would require larger polarizabilities or a non-zero dipole moment as observed in heterobilayers for instance [27]. The methodology used here to determine the QCSE in MoS₂ can be used also in other semiconducting monolayers, where similar values of the polarizability should be obtained owing to the extreme out-of-plane confinement of both electrons and holes, as confirmed by recent measurements on monolayer WSe₂ [28].

4.5 Methods

Device fabrication Van der Waals heterostructures were fabricated by stacking two-dimensional materials via a dry-transfer technique [29]. All layers were mechanically exfoliated from bulk crystals (natural MoS₂ crystal from SPI Supplies, synthetic h-BN [30] and natural graphite from NGS Naturgraphit). MoS₂ monolayers were treated by a bis(tri-fluoromethane)sulfonimide (TFSI) solution following Ref. [31] before full encapsulation between h-BN layers. Few-layer graphene was employed as a top transparent electrode or as a contact electrode to MoS₂ [32]. Metal contacts to FLG were patterned by electron-beam lithography and subsequent metal deposition of Au (45 nm)/Cr (5 nm). The flake thickness of each layer was characterized by a combination of optical contrast, atomic force microscopy, PL and Raman spectroscopy. The data shown in this Letter were measured on a device consisting of SiO₂ (300 nm)/h-BN (5.4 nm)/MoS₂

(0.65 nm)/h-BN (12 nm)/FLG (17 nm).

Photoluminescence measurements Photoluminescence spectroscopy was performed in a liquid He bath cryostat using a home-built confocal microscope setup. The main sample and the reference sample were optically excited using a linearly polarized diode laser at photon energy 2.32 eV (wavelength 535 nm) and a HeNe laser at photon energy 2.09 eV (wavelength 594 nm) with an intensity below 2 kW cm^{-2} , respectively. The collected light was dispersed onto a charged-coupled device array by a single monochromator equipped with a 1500 grooves/mm grating.

Bibliography

- [1] Mak, K. F., Lee, C., Hone, J., Shan, J. & Heinz, T. F. Atomically Thin MoS₂: A New Direct-Gap Semiconductor. *Phys. Rev. Lett.* **105**, 136805 (2010).
- [2] Splendiani, A. *et al.* Emerging Photoluminescence in Monolayer MoS₂. *Nano Lett.* **10**, 1271–1275 (2010).
- [3] Geim, A. K. & Grigorieva, I. V. Van der Waals heterostructures. *Nature* **499**, 419–425 (2013).
- [4] Novoselov, K., Mishchenko, A., Carvalho, A. & Castro Neto, A. 2D materials and van der Waals heterostructures. *Science* **353** (2016).
- [5] Chernikov, A. *et al.* Exciton Binding Energy and Nonhydrogenic Rydberg Series in Monolayer WS₂. *Phys. Rev. Lett.* **113**, 076802 (2014).
- [6] Miller, D. A. B. *et al.* Band-edge electroabsorption in quantum well structures: The quantum-confined Stark effect. *Phys. Rev. Lett.* **53**, 2173–2176 (1984).
- [7] High, A. A., Novitskaya, E. E., Butov, L. V., Hanson, M. & Gossard, A. C. Control of exciton fluxes in an excitonic integrated circuit. *Science* **321**, 229–231 (2008).
- [8] Schinner, G. J. *et al.* Confinement and interaction of single indirect excitons in a voltage-controlled trap formed inside double InGaAs quantum wells. *Phys. Rev. Lett.* **110**, 127403 (2013).
- [9] Schuller, J. A. *et al.* Orientation of luminescent excitons in layered nanomaterials. *Nat. Nanotechnol.* **8**, 271–276 (2013).
- [10] Klein, J. *et al.* Stark effect spectroscopy of mono- and few-layer MoS₂. *Nano Lett.* **16**, 1554–1559 (2016).
- [11] Guo, Y. *et al.* Charge trapping at the MoS₂-SiO₂ interface and its effects on the characteristics of MoS₂ metal-oxide-semiconductor field effect transistors. *Appl. Phys. Lett.* **106**, 103109 (2015).

- [12] Pedersen, T. G. Exciton Stark shift and electroabsorption in monolayer transition-metal dichalcogenides. *Phys. Rev. B* **94**, 125424 (2016).
- [13] Chernikov, A. *et al.* Electrical tuning of exciton binding energies in monolayer WS₂. *Phys. Rev. Lett.* **115**, 126802 (2015).
- [14] Sidler, M. *et al.* Fermi polaron-polaritons in charge-tunable atomically thin semiconductors. *Nat. Phys.* **13**, 255 (2016).
- [15] Efimkin, D. K. & MacDonald, A. H. Many-body theory of trion absorption features in two-dimensional semiconductors. *Phys. Rev. B* **95**, 035417 (2017).
- [16] Cadiz, F. *et al.* Excitonic linewidth approaching the homogeneous limit in MoS₂-based van der Waals heterostructures. *Phys. Rev. X* **7**, 021026 (2017).
- [17] Mak, K. F. *et al.* Tightly bound trions in monolayer MoS₂. *Nat. Mater.* **12**, 207–211 (2013).
- [18] Manassen, A., Cohen, E., Ron, A., Linder, E. & Pfeiffer, L. N. Exciton and trion spectral line shape in the presence of an electron gas in GaAs/AlAs quantum wells. *Phys. Rev. B* **54**, 10609–10613 (1996).
- [19] Ju, L. *et al.* Photoinduced doping in heterostructures of graphene and boron nitride. *Nat. Nanotechnol.* **9**, 348–352 (2014).
- [20] Epping, A. *et al.* Quantum transport through MoS₂ constrictions defined by photodoping. *J. Phys.: Condens. Matter* **40**, 205001 (2016).
- [21] Choi, M. S. *et al.* Controlled charge trapping by molybdenum disulphide and graphene in ultrathin heterostructured memory devices. *Nat. Commun.* **4**, 1624 (2013).
- [22] Wang, H., Wu, Y., Cong, C., Shang, J. & Yu, T. Hysteresis of electronic transport in graphene transistors. *ACS Nano* **4**, 7221–7228 (2010).
- [23] Hawrylak, P. Optical properties of a two-dimensional electron gas: Evolution of spectra from excitons to Fermi-edge singularities. *Phys. Rev. B* **44**, 3821–3828 (1991).
- [24] Ajayi, O. A. *et al.* Approaching the intrinsic photoluminescence linewidth in transition metal dichalcogenide monolayers. *2D Mater.* **4**, 031011 (2017).

- [25] Scharf, B. *et al.* Excitonic stark effect in mos₂ monolayers. *Phys. Rev. B* **94**, 245434 (2016).
- [26] Shields, A. *et al.* Stark effect of negatively and positively charged excitons in semiconductor quantum wells. *Physica E* **2**, 87–92 (1998).
- [27] Rivera, P. *et al.* Observation of long-lived interlayer excitons in monolayer MoSe₂–WSe₂ heterostructures. *Nat. Commun.* **6** (2015).
- [28] Verzhbitskiy, I., Vella, D., Watanabe, K., Taniguchi, T. & Eda, G. Suppressed out-of-plane polarizability of free excitons in monolayer WSe₂. *ACS Nano* **13**, 3218–3224 (2019).
- [29] Zomer, P., Guimarães, M., Brant, J., Tombros, N. & Van Wees, B. Fast pick up technique for high quality heterostructures of bilayer graphene and hexagonal boron nitride. *Appl. Phys. Lett.* **105**, 013101 (2014).
- [30] Taniguchi, T. & Watanabe, K. Synthesis of high-purity boron nitride single crystals under high pressure by using Ba–BN solvent. *J. Cryst. Growth* **303**, 525–529 (2007).
- [31] Amani, M. *et al.* Near-unity photoluminescence quantum yield in MoS₂. *Science* **350**, 1065–1068 (2015).
- [32] Yu, L. *et al.* Graphene/MoS₂ hybrid technology for large-scale two-dimensional electronics. *Nano Lett.* **14**, 3055–3063 (2014).

Chapter 5

Spin-Polarized Electrons in Monolayer MoS₂

Adapted from: Jonas Gaël Roch, Guillaume Froehlicher, Nadine Leisgang, Peter Makk, Kenji Watanabe, Takashi Taniguchi and Richard John Warburton, “Spin-polarized electrons in monolayer MoS₂”, Nat. Nanotechnol., **14**, 432-436 (2019)

Coulomb interactions are crucial in determining the ground state of an ideal two-dimensional electron gas (2DEG) in the limit of low electron densities [1]. In this regime, Coulomb interactions dominate over single-particle phase-space filling. In practice, electrons in silicon and gallium arsenide are typically localized at these low densities. In contrast, in transition metal dichalcogenides (TMDs), Coulomb correlations in a 2DEG can be anticipated at experimentally relevant electron densities. Here, we investigate a 2DEG in a gated monolayer of the TMD molybdenum disulfide [2]. We measure the optical susceptibility, a probe of the 2DEG which is local, minimally-invasive and spin-selective [3]. In a magnetic field, we present evidence that the ground state is spin-polarized. Of the four available conduction bands [4, 5], only two are occupied. These two bands have the same spin but different valley quantum numbers. Our results suggest that only two bands are occupied even at low magnetic fields. The spin-polarization increases with decreasing 2DEG density suggesting that Coulomb interactions are a key aspect of the symmetry breaking. We propose that exchange couplings align the spins [6]. The Bohr radius is so small [7] that even electrons located far apart in phase-space interact with each other [6].

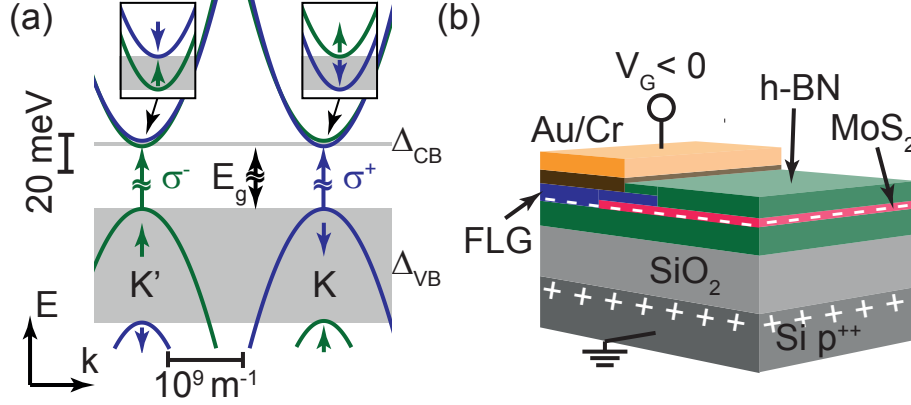


Fig. 5.1. **Monolayer MoS₂**. (a) Band structure of monolayer MoS₂. The colour corresponds to the electron spin state. (b) A van der Waals heterostructure consisting of monolayer MoS₂ embedded in h-BN all placed on a Si/SiO₂ substrate. The MoS₂ is contacted by a few-layer graphite (FLG) electrode [8]. The FLG is covered with a Cr/Au layer to which a voltage V_G is applied.

5.1 Introduction

A two dimensional electron gas (2DEG) is formed when the movement of free electrons is limited to two spatial dimensions. As the electron density n increases, single particle effects (phase-space filling) increases more rapidly than the Coulomb interactions. This ratio is described with the Wigner-Seitz parameter, $r_s = \frac{1}{\sqrt{\pi n}} \frac{1}{a_B}$ where a_B is the effective Bohr radius. Coulomb interactions dominate at large values of r_s . However, in 2DEGs in silicon and gallium arsenide, the electrons are typically localized at large values of r_s .

Monolayer transition metal dichalcogenides (TMDs) such as MoS₂, MoSe₂, WS₂ and WSe₂ represent a natural host for a 2DEG. There are two inequivalent conduction band valleys at the K and K' points of the Brillouin zone. The large electron effective mass [4] and the weak dielectric screening result in an extremely small Bohr radius [7], ~ 0.5 nm. The immediate consequence is that r_s is pushed towards relatively large values at experimentally relevant electron concentrations.

MoS₂ is a special TMD as the spin-orbit splitting in the conduction band is small compared to typical 2DEG Fermi energies [5]. There are four available bands: K_{\uparrow} , K_{\downarrow} , K'_{\uparrow} and K'_{\downarrow} . In a single-particle picture at realistic electron concentrations, the low temperature ground state consists of a close-to-equal filling of the four bands. We present here an experiment which overturns this single-particle picture.

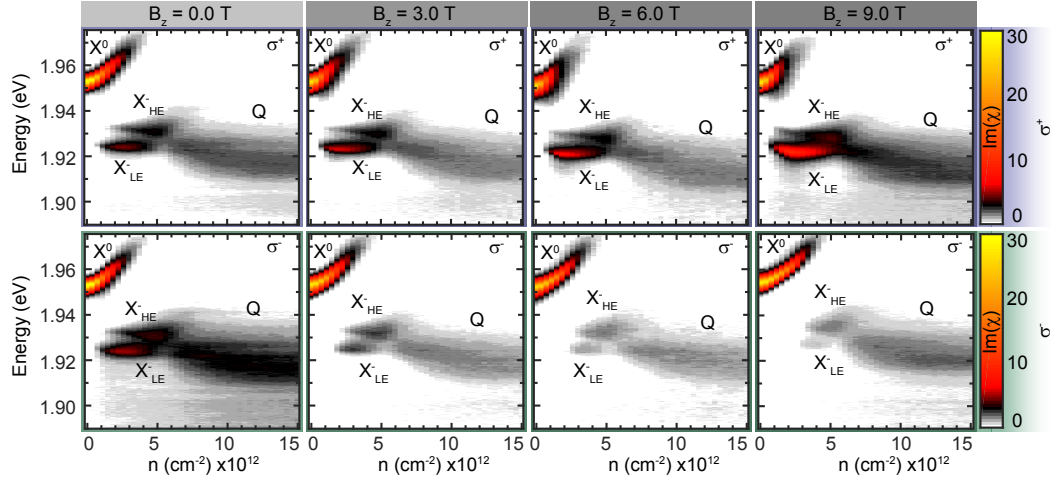


Fig. 5.2. **Optical susceptibility of a gated monolayer of MoS₂.** The optical reflectivity is measured from a 400 nm diameter region on the device at low temperature (4.2 K) using a confocal microscope and ultra-weak, incoherent light source [9]. The imaginary part of the optical susceptibility is deduced from the reflectivity by accounting for optical interferences [9, 10]. At the optical resonance, the reflectivity contrast is very large, 60%; equivalently, the susceptibility is 30. The colour-maps show the optical susceptibility as a function of the photon energy (vertical axis) and electron concentration (horizontal axis) in a perpendicular magnetic field B_z of 0.0, 3.0, 6.0 and 9.0 T with σ^+ -polarized light (top panels) and with σ^- -polarized light (bottom panels).

5.2 Methods

We probe the 2DEG ground state in MoS₂ by measuring the susceptibility at optical frequencies. This probe is particularly powerful. First, it is a local measurement: signal is gleaned from a few-hundred-nanometer diameter spot on the sample. On this length scale, close-to-ideal optical linewidths have been demonstrated [11, 12] yet there are clearly inhomogeneities on larger length scales even with state-of-the-art material. Secondly, the measurement represents a weak perturbation to the ground state: in our experiments, there is on average less than one photo-created excitation (an exciton, an electron-hole pair) [9]. Thirdly, the optical probe is valley- and spin-selective via the polarization of the light [3].

Interpreting our results with the established theory of the 2DEG optical susceptibility shows that up to $n \simeq 5 \times 10^{12} \text{ cm}^{-2}$, two and not four bands are occupied. The electrons have the same spin but reside in different valleys. This is our main result: the spontaneous creation of a spin-polarized 2DEG.

Monolayer MoS₂ has a graphene-like structure with Mo and S sub-lattices [2, 3]. The band edges are located at the K and K' points; an energy gap of about 2 eV separates

the conduction band (CB) from the valence band (VB) (Fig. 6.1(a)). Spin degeneracy is lifted by spin-orbit coupling. In each valley, the two CBs are split by $\Delta_{\text{CB}} \approx 3$ meV [4, 5, 13] and the two VBs are split by $\Delta_{\text{VB}} \approx 150$ meV [5]. In MoS₂, the upper VB has the same spin as the lower CB [14]. Optical absorption promotes an electron from a VB state to a CB state with strict selection rules [3]: a circularly polarized σ^+ photon couples the VB and CB with spin- \downarrow at the K point; a σ^- photon couples the VB and CB with spin- \uparrow at the K' point (Fig. 6.1(a)).*

Fig. 6.1(b) shows the structure of our sample. A monolayer of MoS₂ forms a planar capacitor with respect to a conductive substrate. The carrier density n in the monolayer is determined by a voltage V_G applied to the capacitor [9]. The MoS₂ monolayer is encapsulated in hexagonal boron nitride (h-BN): this allows close-to-ideal optical linewidths [9, 11] and Shubnikov-de Haas oscillations [15] to be observed at low temperature. We measure the optical susceptibility. At $n \simeq 0$, the optical spin-valley effect is very pronounced [9].

5.3 Optical susceptibility of a monolayer of MoS₂ at various electron concentrations

Fig. 6.2 shows the local optical susceptibility as a function of electron concentration at various B_z . We focus initially on the susceptibility at $B_z = 9.0$ T for $n \leq 6 \times 10^{12} \text{ cm}^{-2}$.

At low electron density, the peak labeled X^0 dominates the susceptibility for both σ^+ and σ^- . This resonance corresponds to the creation of a neutral exciton. As n increases, the X^0 blue-shifts (on account of band-gap renormalization), broadens and weakens, eventually disappearing into the noise. With σ^+ polarization, as X^0 weakens, two resonances emerge, labelled X_{LE}^- and X_{HE}^- . These two resonances are red-shifted with respect to X^0 . In the opposite photon polarization, σ^- , as n increases the X^0 resonance blue-shifts and weakens but for low to modest n there are no X^- features.

The excitons injected into the 2DEG by our optical probe interact with the electrons in the Fermi sea. Theory has been developed to describe an exciton interacting either with a spin-degenerate Fermi sea at the Γ -point of the Brillouin zone [16, 17] or a spin-polarized Fermi sea [18], and successfully stress-tested against experiments on quantum wells [16] and monolayer MoSe₂ [19]. When the exciton-electron interaction is attractive, the exciton resonance splits into two exciton-polarons [18, 19]. The upper exciton-polaron corresponds to X^0 ; the lower exciton-polaron corresponds to X^- (and becomes the trion

*In the literature, there is often the opposite convention that σ^+ and σ^- are defined such that a σ^+ (σ^-) photon addresses the transition between two bands with spin- \uparrow (spin- \downarrow).

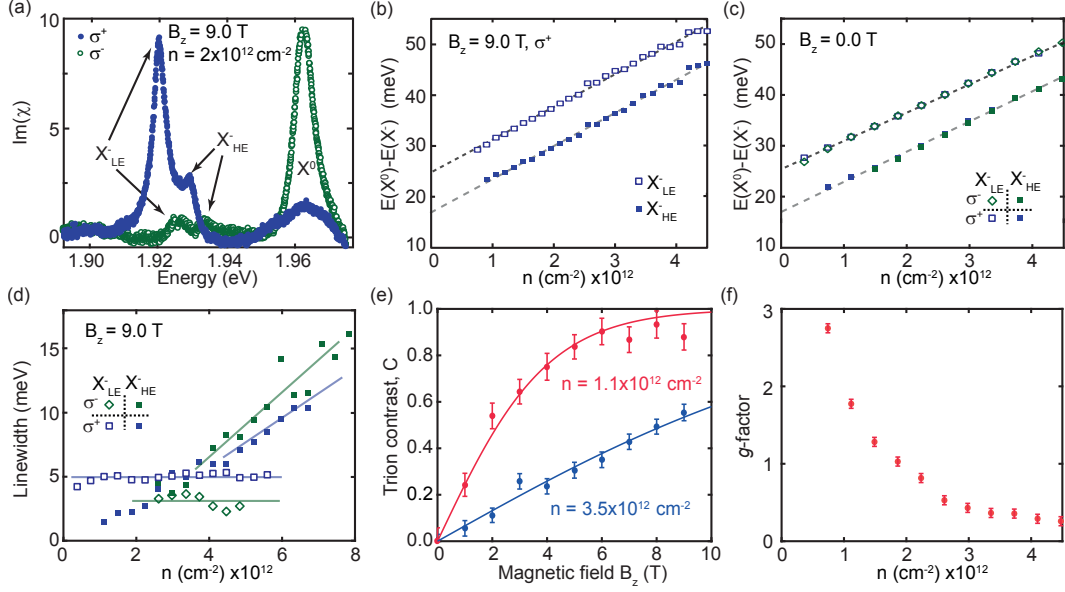


Fig. 5.3. **Analysis of the optical susceptibility of a gated monolayer of MoS₂.** (a) Optical susceptibility at $B_z = 9.0$ T and $n = 2.0 \times 10^{12} \text{ cm}^{-2}$ for both σ^+ and σ^- photons. For σ^+ , two trion resonances (X_{LE}^- and X_{HE}^-) dominate the spectrum. (LE stands for low-energy; HE high-energy.) For σ^- , X^0 dominates and X^0 has a high energy tail. (b) Energetic difference $E(X^0) - E(X^-)$ for the two trions at $B_z = 9.0$ T as a function of n . Linear fits give slopes of 6.1×10^{-15} and $6.3 \times 10^{-15} \text{ eVcm}^2$ for X_{LE}^- and X_{HE}^- , respectively. (c) As in (b), but at $B_z = 0.0$ T. Linear fits give 5.6×10^{-15} and $5.9 \times 10^{-15} \text{ eVcm}^2$ for X_{LE}^- and X_{HE}^- , respectively. The trion binding energies are 17 meV (X_{LE}^-) and 25 meV (X_{HE}^-). (d) Linewidth of X_{LE}^- and X_{HE}^- at $B_z = 9.0$ T versus n . (e) Contrast C (as defined in the text) versus B_z for $n = 1.1 \times 10^{12} \text{ cm}^{-2}$ (red) and for $n = 3.7 \times 10^{12} \text{ cm}^{-2}$ (blue). The solid lines are a fit to two-level Maxwell-Boltzmann statistics with notional g -factor $g = 1.6 \pm 0.1$ (red) and $g = 0.4 \pm 0.1$ (blue). (f) Notional g -factor as a function of n . Taking a Bohr radius of 0.48 nm, $n = 1.0 \times 10^{12} \text{ cm}^{-2}$ corresponds to $r_s = 11.8$.

in the single-particle limit [14, 20, 21]). On the other hand, when the exciton-electron interaction is repulsive, only the X^0 appears in the susceptibility with a tail on the high energy side [9]. In these theories, the interaction is attractive only if the electron in the exciton and the electron in the Fermi sea have opposite spins, a spin-singlet. The interaction is repulsive for parallel spins, a spin-triplet.

We apply the exciton-polaron theory to the MoS₂ susceptibility. With σ^+ photons, we observe not one but *two* lower exciton-polarons, X_{LE}^- and X_{HE}^- . This implies that the exciton interacts with *two* Fermi seas, the energy splitting arising from different exciton-electron scattering cross-sections. Specifically, the electron in the exciton has spin- \downarrow . To form spin-singlets, both Fermi seas must have spin- \uparrow , i.e. the K_{\uparrow}' and K_{\uparrow} bands are occupied. The different binding energies (defining the binding energy as the energy

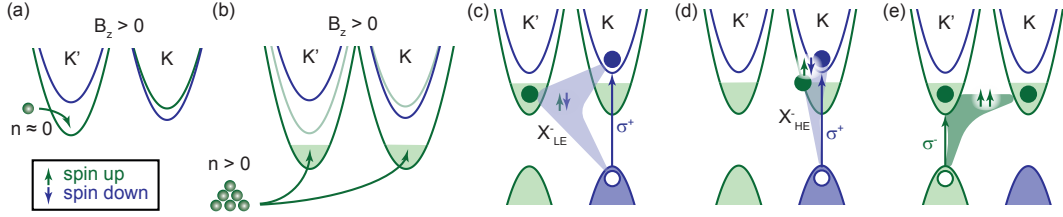


Fig. 5.4. **Electrons and exciton states in monolayer MoS₂.** (a) The conduction bands at $B_z = 9$ T. The minima all have different energies due to Zeeman shifts [9]. The “first” electrons injected from the contact populate the band with the lowest energy, K' . (b) Strong intra- and inter-valley exchange pull the bands of the same spin to lower energy, creating a spin-polarized 2DEG. (c) Exciton-Fermi sea interaction resulting in X_{LE}^- . (d) Exciton-Fermi sea interaction resulting in X_{HE}^- . The trions in (c) and (d) both correspond to electron spin-singlets. (e) A trion with an electron spin-triplet. This trion resonance is unbound and results in the high energy tail of the X^0 with σ^- photons.

separation between the two exciton-polarons in the limit $n \rightarrow 0$) arise from the fact that the two Fermi seas are at different locations in phase-space. The X_{LE}^- has a constant linewidth whereas the X_{HE}^- has a linewidth which increases with n (Fig. 5.3(d)). This difference also points to the fact that the exciton interacts with two different Fermi seas. With σ^- photons, the spectra follow the exciton-polaron theory for a repulsive exciton-Fermi sea interaction. This means that the photo-excited spin- \uparrow electrons interacts with spin- \uparrow electrons in the Fermi sea: there are no spin- \downarrow partners to create spin-singlets in this case. For both σ^+ and σ^- photons, the details of the measured spectra match the exciton-polaron theory [9].

We are led to the conclusion that at $B_z = 9.0$ T, two bands are occupied, both with spin- \uparrow . Fig. 5.4(c-d) show how we understand the two X^- resonances. A photon-generated electron-hole pair with electron spin- \downarrow interacts attractively with spin- \uparrow electrons from two different bands. The trion binding for the inter-valley scattering process (Fig. 5.4(c)) is larger [22, 23] as the electrons have both opposite spin and valley indices, similar to MoSe₂ [10]. We associate this process to the resonance X_{LE}^- . The intra-valley scattering process (Fig. 5.4(d)) leads to the resonance X_{HE}^- . The absence of an X^- resonance in σ^- polarization tells us that the triplet process in Fig. 5.4(e) is unbound.

Of the four bands, only *two* are occupied. This conclusion on the number of occupied bands can be verified via another feature of the susceptibility spectra. In the limit of large hole mass, the energetic separation between the upper and lower exciton-polarons is simply $\delta E = E(X^0) - E(X^-) = E_B + E_F$ where E_B is the trion binding energy and E_F the Fermi energy [24], a result demonstrated experimentally on CdTe quantum wells [25]. For the equal hole and electron masses of MoS₂, this result applies at $E_F \geq 20$ meV [9]. The gradient $d\delta E/dE_F$ increases from 1.0 to 2.0 as $E_F \rightarrow 0$. Our experimental data

lie mostly in the high- E_F regime [9]. This enables us to determine E_F from the optical spectra. As E_F is linked to n by the two-dimensional density of states, we can determine how many bands are populated. Taking an electron effective mass of $m_e^* = 0.44m_o$ [4], the measured $d\delta E/dn$ (Fig. 5.3(b)) implies that 1.9 ± 0.1 bands are occupied at $B_z = 9.0$ T [9]*.

We turn now to the magnetic field dependence. At $B_z = 0.0$ T, the X_{LE}^- and X_{HE}^- features are equally strong for both σ^+ and σ^- photons (Fig. 6.2). As B_z increases, the X_{LE}^- and X_{HE}^- gradually disappear for σ^- photons. At $B_z = 0.0$ T, the gradients $d\delta E/dn$ (Fig. 5.3(c)) change by less than 10% with respect to $B_z = 9.0$ T, suggesting that even in this limit, only two bands are occupied. Given the equivalence of the spectral signatures at $B_z = 0.0$ T with respect to those at $B_z = 9.0$ T (Fig. 6.2), the same two bands are occupied, the two with the same spin but different valley indices. We define a contrast C as

$$C = \frac{I_{LE+HE}(\sigma^+) - I_{LE+HE}(\sigma^-)}{I_{LE+HE}(\sigma^+) + I_{LE+HE}(\sigma^-)}, \quad (5.1)$$

where $I_{LE+HE}(\sigma^+)$ [$I_{LE+HE}(\sigma^-)$] is the integrated susceptibility of X_{LE}^- and X_{HE}^- in σ^+ [σ^-] polarization. C increases from $C = 0\%$ at $B_z = 0.0$ T to $C = 95\%$ at $B_z = 9.0$ T (Fig. 5.3(e)). Phenomenologically, we imagine that there are two states, one with spin-polarization \uparrow , the other with spin-polarization \downarrow . The two states are separated by $g\mu_B B_z$ where μ_B is the Bohr magneton and g is a g -factor. Maxwell-Boltzmann statistics applied to this notional two-level system gives $C(B) = \tanh(g\mu_B B_z/k_B T)$, where k_B is the Boltzmann constant and T the temperature. C follows this dependence on B (Fig. 5.3(e)). The notional g -factor decreases strongly with increasing n (decreasing r_s) (Fig. 5.3(f)). This n -dependence (and the temperature dependence [9]) suggests strongly that the spin polarization arises as a consequence of Coulomb correlations [27]. A microscopic interpretation of these two spin-polarized states represents an open question.

It is worth adding that despite the large value of $B_z = 9$ T, no hints of Landau levels are observed in the low electron concentration regime, as in monolayer MoSe₂ [10] and WSe₂ [28]. Even at 9 T, Coulomb interactions are indeed so strong that the exciton is in the weak field regime [29]. The experiment would therefore suggest that Landau quantization is not crucial for the spontaneous spin-polarization.

For $n \geq 6 \times 10^{12} \text{ cm}^{-2}$, X_{LE}^- and X_{HE}^- weaken and the susceptibility is dominated by

*Here, an effective electron mass of 0.44 explains well our results. Recent theoretical work by Miserev *et al.* [26] supports the idea of an equal two-band filling of the conduction bands (the two conduction bands with the same spin). Improvements of the sample fabrication techniques have increased the efficiency of the electron injection in the MoS₂ 2DEG. Our results are now compatible with an effective mass of 0.8 under the assumption of an equal two-bands filling. These results are compatible with the recent electronic transport by Pisoni *et al.* [15]

a broad, red-shifted peak labeled Q (Fig. 6.2). There is no established theory for the optical susceptibility in this regime where the Fermi energy exceeds the trion binding energy. Nevertheless, we speculate that the absence of a marked contrast between σ^+ and σ^- signals that the 2DEG is no longer spin-polarized.

The spin-polarization of the MoS_2 2DEG can be qualitatively understood by exchange [30] and the strong inter-valley Coulomb scattering [6, 31, 32]. At low temperature, the “first” injected electrons populate the band with lowest energy (Fig. 5.4(a)). Intra-valley and inter-valley exchange will then favour population of the bands with the same electron spin (Fig. 5.4(b)): the small CB spin-orbit splitting implies a moderate cost in kinetic energy. These results highlight a very particular feature of TMDs. The Bohr radius is only slightly larger than the lattice constant such that the two-body Coulomb interaction connecting an electron at the K point with an electron at the K' point (far apart in phase-space) is comparable to the two-body Coulomb interaction between two electrons close together in phase-space [6].

5.4 Conclusion

At first sight, the spin polarization mimics Stoner ferromagnetism. However, the Stoner mechanism is based on a mean-field theory which is invalid in two-dimensions for which ferromagnetic order is excluded by the Mermin-Wagner theorem [33]. However, the conduction band spin-orbit splitting, small but non-zero, establishes an in-built quantization axis such that a spontaneous symmetry-breaking is feasible, Mermin-Wagner notwithstanding. Theory is lacking and should go beyond the standard random-phase-approximation [34].

Full spin polarization is achieved here at rather large external magnetic fields. It may be possible to create spin polarizations at lower magnetic fields by using a magnetic substrate [35]. In turn, patterning this substrate may allow a textured spin polarization to be generated.

Bibliography

- [1] Attaccalite, C., Moroni, S., Gori-Giorgi, P. & Bachelet, G. B. Correlation energy and spin polarisation in the 2D electron gas. *Phys. Rev. Lett.* **88**, 256601 (2002).
- [2] Mak, K. F., Lee, C., Hone, J., Shan, J. & Heinz, T. F. Atomically thin MoS₂: A new direct-gap semiconductor. *Phys. Rev. Lett.* **105**, 136805 (2010).
- [3] Xiao, D., Liu, G.-B., Feng, W., Xu, X. & Yao, W. Coupled spin and valley physics in monolayer of MoS₂ and other group-VI dichalcogenides. *Phys. Rev. Lett.* **108**, 196902 (2012).
- [4] Kormányos, A., Zoloyomi, V., Drummond, N. D. & Burkard, G. Spin-orbit coupling, quantum dots , and qubits in monolayer transition metal dichalcogenides. *Phys. Rev. X* **4**, 011034 (2014).
- [5] Liu, G.-B., Shan, W.-Y., Yao, Y., Yao, W. & Xiao, D. Three-band tight-binding model for monolayers of group-VIB transition metal dichalcogenides. *Phys. Rev. B* **89**, 039901 (2014).
- [6] Dery, H. Theory of intervalley Coulomb interactions in monolayer transition-metal dichalcogenides. *Phys. Rev. B* **94**, 075421 (2016).
- [7] Chernikov, A. *et al.* Exciton binding energy and nonhydrogenic Rydberg series in monolayer WS₂. *Phys. Rev. Lett.* **113**, 076802 (2014).
- [8] Yu, L. *et al.* Graphene/MoS₂ hybrid technology for large-scale two-dimensional electronics. *Nano Lett.* **14**, 3055–3063 (2014).
- [9] *More details are provided in Appendix A .*
- [10] Back, P. *et al.* Giant paramagnetism-induced valley polarization of electrons in charge-tunable monolayer MoSe₂. *Phys. Rev. Lett.* **118**, 237404 (2017).
- [11] Cadiz, F. *et al.* Excitonic linewidth approaching the homogeneous limit in MoS₂-based van der Waals heterostructures. *Phys. Rev. X* **7**, 021026 (2017).

- [12] Ajayi, O. A. *et al.* Approaching the intrinsic photoluminescence linewidth in transition metal dichalcogenide monolayers. *2d Mater.* **4**, 031011 (2017).
- [13] Marinov, K., Avsar, A., Watanabe, K., Taniguchi, T. & Kis, A. Resolving the spin splitting in the conduction band of monolayer MoS₂. *Nat. Commun.* **8**, 1938 (2017).
- [14] Mak, K. F. *et al.* Tightly bound trions in monolayer MoS₂. *Nat. Mater.* **12**, 207 (2013).
- [15] Pisoni, R. *et al.* Interactions and magnetotransport through spin-valley coupled Landau levels in monolayer MoS₂. *Phys. Rev. Lett.* **121**, 247701 (2018).
- [16] Suris, R. A. *et al.* Excitons and trions modified by interaction with a two-dimensional electron gas. *Phys. Status Solidi B* **227**, 343–352 (2001).
- [17] Ossau, W. J. & Suris, R. *Optical Properties of 2D Systems with Interacting Electrons* (Kluwer Academic Publishers, 2003).
- [18] Efimkin, D. K. & MacDonald, A. H. Many-body theory of trion absorption features in two-dimensional semiconductors. *Phys. Rev. B* **95**, 035417 (2017).
- [19] Sidler, M. *et al.* Fermi polaron-polaritons in charge-tunable atomically thin semiconductors. *Nat. Phys.* **13**, 255–261 (2016).
- [20] Plechinger, G. *et al.* Trion fine structure and coupled spin–valley dynamics in monolayer tungsten disulfide. *Nat. Mater.* **7**, 12715 (2016).
- [21] Courtade, E. *et al.* Charged excitons in monolayer WSe₂: Experiment and theory. *Phys. Rev. B* **96**, 085302 (2017).
- [22] Yu, H., Liu, G., Gong, P., Xu, X. & Yao, W. Dirac cones and Dirac saddle points of bright excitons in monolayer transition metal dichalcogenides. *Nat. Commun.* **5**, 3876 (2014).
- [23] Yu, H., Cui, X., Xu, X. & Yao, W. Valley excitons in two-dimensional semiconductors. *Natl. Sci. Rev.* **2**, 57–70 (2015).
- [24] Hawrylak, P. Optical properties of a two-dimensional electron gas: Evolution of spectra from excitons to Fermi-edge singularities. *Phys. Rev. B* **44**, 3821 (1991).
- [25] Huard, V., Cox, R. T., Saminadayar, K., Arnoult, A. & Tatarenko, S. Bound states in optical absorption of semiconductor quantum wells containing a two-dimensional electron gas. *Phys. Rev. Lett.* **84**, 187 (2000).

- [26] Miserev, D., Klinovaja, J. & Loss, D. Spontaneous Symmetry Breaking in Monolayers of Transition Metal Dichalcogenides. *arXiv e-prints* arXiv:1902.07961 (2019). [arXiv:1902.07961](#).
- [27] Wang, Z., Mak, K. F. & Shan, J. Strongly interaction-enhanced valley magnetic response in monolayer WSe₂. *Phys. Rev. Lett.* **120**, 066402 (2018).
- [28] Wang, Z., Shan, J. & Mak, K. F. Valley- and spin-polarized Landau levels in monolayer WSe₂. *Nat Nanotechnol.* **12** (2016).
- [29] Stier, A. V., McCreary, K. M., Jonker, B. T., Kono, J. & Crooker, S. A. Exciton diamagnetic shifts and valley Zeeman effects in monolayer WS₂ and MoS₂ to 65 Tesla. *Nat. Commun.* **7**, 10643 (2016).
- [30] Scrace, T. *et al.* Magnetoluminescence and valley polarized state of a two-dimensional electron gas in WS₂ monolayers. *Nat. Nanotechnol.* **10**, 603 (2015).
- [31] Groenewald, R. E., Rösner, M., Schönhoff, G., Haas, S. & Wehling, T. O. Valley plasmonics in transition metal dichalcogenides. *Phys. Rev. B* **93**, 205154 (2016).
- [32] Van Tuan, D., Benedikt, S., Žutić, I. & Dery, H. Marrying excitons and plasmons in monolayer transition-metal dichalcogenides. *Phys. Rev. X* **7**, 041040 (2017).
- [33] Mermin, N. D. & Wagner, H. Absence of ferromagnetism or antiferromagnetism in one- or two-dimensional isotropic Heisenberg models. *Phys. Rev. Lett.* **17**, 1133 (1966).
- [34] Žak, R. A., Maslov, D. & Loss, D. Spin susceptibility of interacting two-dimensional electrons in the presence of spin-orbit coupling. *Phys. Rev. B* **82**, 115415 (2010).
- [35] Zhao, C. *et al.* Enhanced valley splitting in monolayer WSe₂ due to magnetic exchange field. *Nat. Nanotechnol.* **12**, 757 (2017).

Chapter 6

First order phase transition in a MoS₂ itinerant ferromagnet

6.1 Introduction

Electrons in a two-dimensional electron gas (2DEG) experience a repulsive interaction due to their charge. By preferably populating states with the same spin, they can save energy with electron-electron exchange despite the kinetic energy cost. However, a ferromagnetic order at any finite temperature is excluded by the Mermin-Wagner theorem [1].

In a semiconducting 2DEG, electrons behave similarly to that of an ideal 2DEG, with the band structure dictating their dispersion. Monolayer MoS₂ has four conduction bands at Fermi energies experimentally relevant, two with opposite spins in the two inequivalent K and K' points of the Brillouin zone. Spin-orbit interaction lifts the degeneracy of the spin states at K and K' by ≈ 3 meV [2, 3, 4]. An out-of-plane anisotropy results from the small but finite spin-orbit interaction and lifts the validity of the Mermin-Wagner theorem. Recent theoretical work by Miserev *et al.* [5] has shown that non-analyticities [6] in the Taylor expansion of the free-energy in term of the magnetisation M are important in the case of MoS₂. The free-energy F expansion then goes beyond standard Ginzburg-Landau theory and reads

$$F(M) \approx aM^2 + c|M|^3 + bM^4 + \dots, \quad (6.1)$$

where a , b and c are functions of the electron density. The parameter b comes from Pauli blocking and must therefore be positive as a high magnetisation has a kinetic energy cost. The parameter a can be negative, in which case a spontaneous magnetisation (Stoner magnetism) can occur (even with $c = 0$). In this case, as a would increase with the carrier density n due to the reduced strength of Coulomb interactions at high carrier density, the magnetisation would gradually shift to zero. This scheme would then describe a first

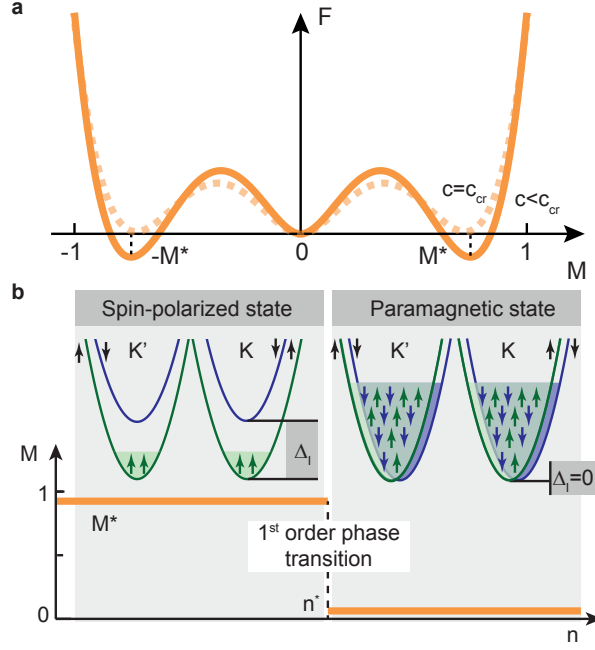


Fig. 6.1. **First order transition in monolayer MoS₂.**(a) Free energy F as a function of the magnetisation M , as in Eq. 6.1. Due to the cubic term $c|M|^3$, F is minimised by a large magnetisation M^* of the 2DEG. For the Free-energy plotted here, we have $a, b > 0$, $c < 0$. The dashed functional is plotted for $c = c_{cr}$, the critical value of the parameter c for which the magnetisation jumps from 0 to M^* . (b) The electron density n acts as a control of the order parameter M . The transition from a spin-polarised 2DEG ground state to a paramagnetic state occurs abruptly at the critical density n^* .

order phase transition. On the other hand, when the non-analyticities are accounted for with $c < 0$, the functional in Eq. 6.1 has a global minimum at a high magnetisation [5]. When the term c increases with n , the magnetisation can jump abruptly from a finite and large magnetisation to a zero magnetisation, as in Fig. 6.1(b). A jump of the magnetisation is a consequence of the first order nature of the phase transition.

In a single-particle picture, a near-to-equal filling of the four lowest energy conduction bands (see Fig. 6.2) is expected when the Fermi level lies above the spin-orbit splitting. In our recent work on the absorption of a gated monolayer MoS₂, we have used absorption spectroscopy to show that inter-valley electron exchange overturns the single-particle picture [7]. The electronic ground state is spin-polarised and consists of two Fermi seas sharing the same spin but having different valley quantum numbers [7]. Here, we use photoluminescence and absorption spectroscopy to show that the 2DEG formed by a monolayer of MoS₂ undergoes a first-order phase transition from a ferromagnetic state to a paramagnetic state at a critical electron density $n^* = 4.5 \cdot 10^{12} \text{ cm}^{-2}$.

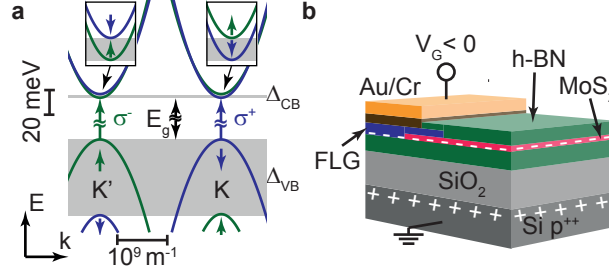


Fig. 6.2. **Sample and band dispersion of MoS₂.**(a) Band structure of monolayer MoS₂ in a single-particle picture. The spin states are indicated by the arrows. (b) The device forms a planar capacitor where the monolayer MoS₂ acts as an electrode separated to the conducting silicon substrate by an oxide layer. The monolayer MoS₂ is fully encapsulated into h-BN.

6.2 Methods

The photoluminescence is obtained by exciting the MoS₂ with a red HeNe laser at an energy of 1.96 eV using a home-built confocal setup. Our setup is polarisation-resolved and we can use liquid crystal variable retarders to excite and detect in the two circular polarisations of light. This is particularly important in the case of MoS₂: by exciting the sample with σ^+ (σ^-) photons, we create an exciton in the K (K') valley (see Fig. 6.2(a)), as a consequence of the optical spin-valley effect [3]. We can therefore analyse the photoluminescence of MoS₂ in the presence of a 2DEG in four polarisations configurations (excitation/collection): (σ^+/σ^-), (σ^-/σ^+), (σ^+/σ^+) and (σ^-/σ^-). For clarity, from now on, the polarisation of the excitation laser is defined as if the experiment were carried out in a forward scattering geometry.

Absorption was determined from reflectivity contrast measurement using Kramers-Kronig relations [7]. A white LED was used to illuminate the sample and the light was gleaned from a diffraction limited spot on the sample surface.

In order to use optics to probe the ground-state of the 2DEG, we used low optical excitation power to ensure that the number of electron-hole pair excitations at a time are out-numbered by more than four orders of magnitude by the 2DEG electrons.

The 2DEG is formed by a monolayer of MoS₂ fully encapsulated in hexagonal boron nitride (h-BN). The h-BN encapsulation is known to be a critical step to obtain transform limited line-width [8]. A gold metallic contact within the van der Waals heterostructure is used to inject electrons efficiently in the 2DEG [9]. A capacitance C between the doped substrate and the MoS₂ flake is formed by a 300-nm thick silicon oxide layer. The electron density in the 2DEG is then controlled via the voltage V_G applied across the capacitance, $n = CV_G$. As a consequence of the photon-doping effect [10, 11], the

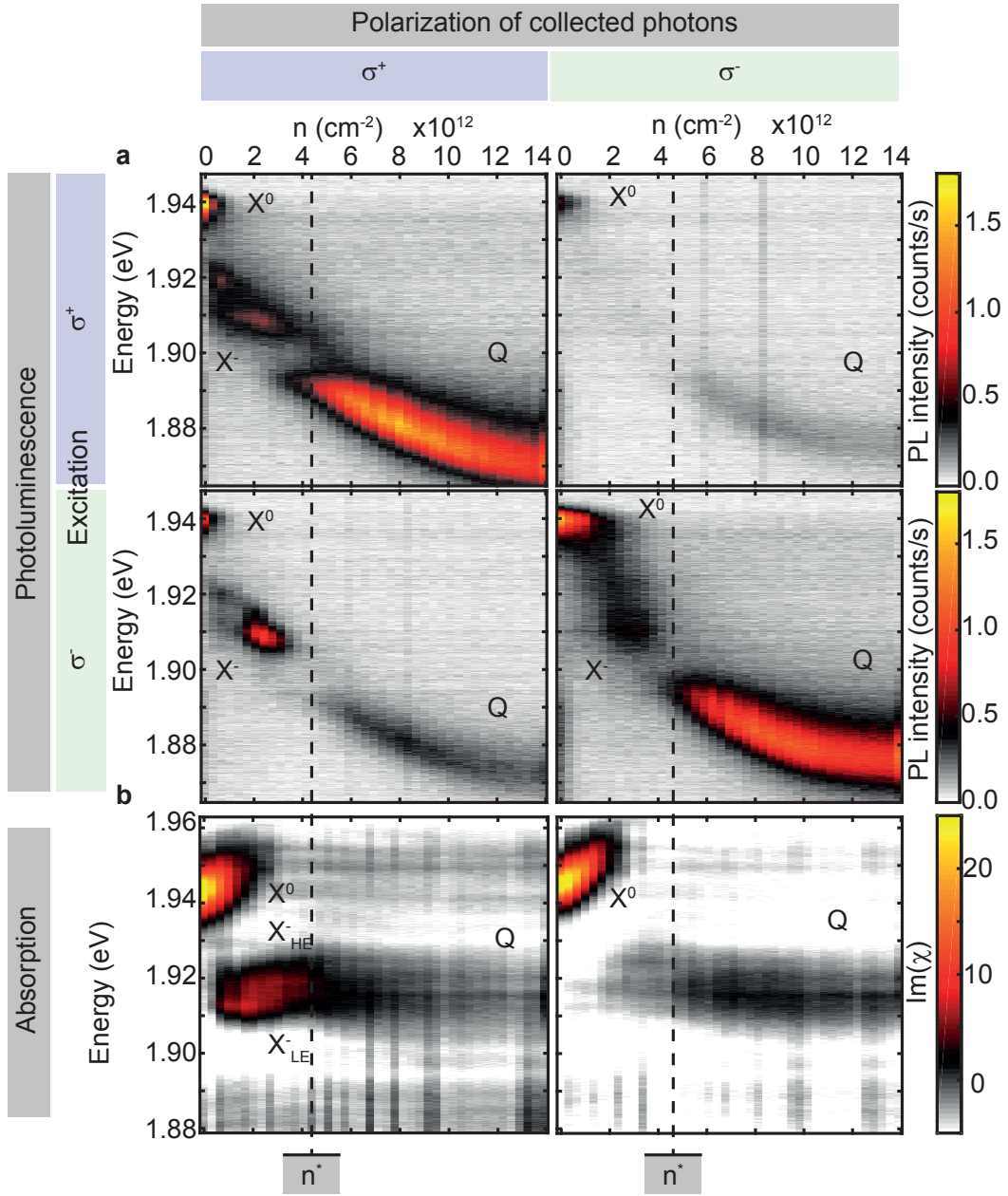


Fig. 6.3. **Optics of a monolayer MoS₂ as a function of electron density.** (a) Polarisation resolved photoluminescence of the MoS₂ 2DEG at various electron density n as a colour-map. The two lines of colour-maps correspond to the two excitation photons' circular polarisations. The two columns of colour-maps decompose the photoluminescence signal into the two circular polarisations. (b) Imaginary part of the optical susceptibility (absorption) as a function of n as colour-maps. The colour-map left (right) shows the optical response to σ^+ (σ^-) photons. Data obtained in an out-of-plane magnetic field of 9 T and a temperature of 4 K.

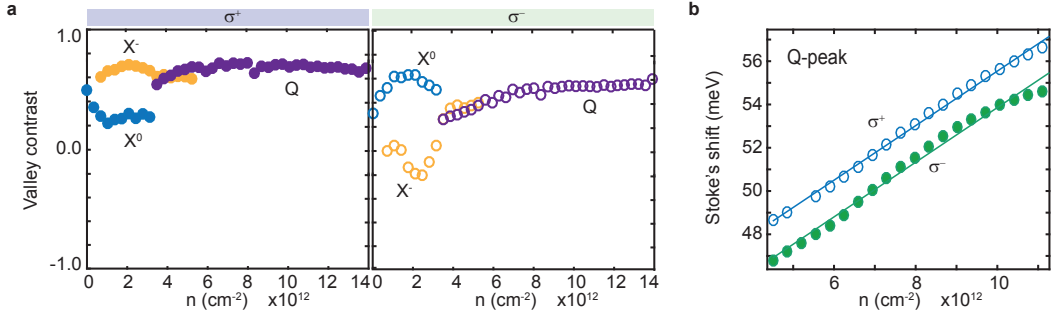


Fig. 6.4. **Processed data.** (a) Evolution of the photoluminescence valley contrast as a function of n for both circular polarisations. (b) Stoke's shift of the Q-peak in photoluminescence as a function of n . The slopes extracted from the fit are $2.52 \cdot 10^{-15} \text{ eVcm}^2$ and $2.53 \cdot 10^{-15} \text{ eVcm}^2$. Data obtained in an out-of-plane magnetic field of 9 T and a temperature of 4 K.

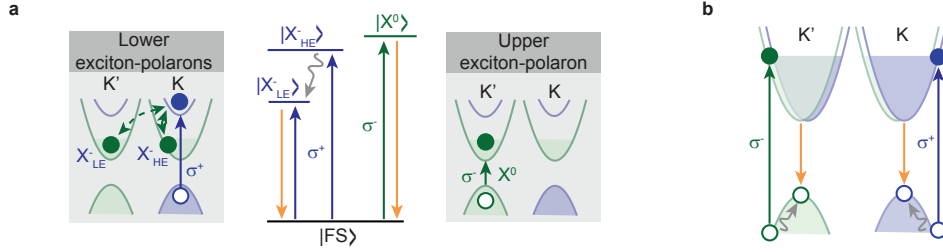


Fig. 6.5. **Optics of monolayer MoS₂.** (a) In the ferromagnetic state, the photo-excited ground states are different in the two polarisations of light. Due to the spin-nature of the exciton-Fermi sea (FS) interaction, two lower exciton-polarons (X_{LE}^- and X_{HE}^-) exist in σ^+ polarisation, while only the X^0 exists in the σ^- polarisation. (b) When the electronic ground state changes to a paramagnetic state, the optics is dominated by band-to-band absorption.

carrier density in the 2DEG decreases with time as the laser light exposure is long during a measurement. In order to circumvent the problem, after each spectrum acquisition, we re-initialise the charge state of the 2DEG by depleting it with the gate and sweeping back again to the same voltage.

Our measurements are all performed in a magnetic field of 9.0 T. It has little implications on the nature of the 2DEG ground state, but it helps stabilising a given spin state of the 2DEG [7].

6.3 Results and discussion

Fig. 6.3(a) shows colour-maps of the polarisation-resolved photoluminescence and the absorption spectra of a gated monolayer MoS₂ at varying n and in an out-of-plane magnetic

field $B_z = 9.0$ T. Using the spin-valley selection rules, we can deterministically create an exciton in the K (K') valley by exciting the sample with σ^+ (σ^-) circularly-polarised light [3]. We collect the light from a given valley by filtering the photoluminescence signal using the σ^+ and σ^- basis. In Fig. 6.4(a) shows the polarisation-resolved absorption spectrum at the same location on the sample with the same electron densities.

At low $n \approx 0$, light is emitted solely from the neutral exciton, labelled as X^0 . A significantly higher signal is seen in the configurations (σ^+/σ^+) and (σ^-/σ^-) , as expected from the valley-spin selection rules [3]. Due to the non-resonant photoluminescence excitation, we measure a finite signal in the (σ^+/σ^-) and (σ^-/σ^+) configurations [12]. However, in absorption, the selection rules are robust and no cross-talk between the two polarisations is measured. Robustness of the absorption selection rules tells us that the momentum is a good quantum number and that we do not suffer from spatial inhomogeneities in the ≈ 500 nm spot from which we collect the light.

At $0 < n < n^* = 4.5 \cdot 10^{12} \text{ cm}^{-2}$, the optical susceptibility is described by the Suris' model [13, 14, 15]. The exciton interacts attractively with the 2DEG when the spin of electron component of the exciton is anti-parallel to that of the 2DEG electrons. In this case, two resonances appear at energy lower than the X^0 . As a consequence of the spin-polarised 2DEG, the two lower exciton-polarons (X_{LE}^- and X_{HE}^-) appear in the σ^+ polarisation only. The two peaks come from the different trion binding energies of an exciton with an electron of the K or the K' valley.

In the photoluminescence, at $0 < n < n^*$, light is emitted at energy lower than X^0 (feature labelled X^- in Fig. 6.3(a)) only when we collect the σ^+ -polarised light or, equivalently, the light emitted from the K valley. This can be understood from the absorption spectra: the energetically favourable X_{LE}^- state exists only in the σ^+ polarisation.

When $n = n^*$, the optical response in both photoluminescence and absorption changes dramatically. The absorption changes from sharp excitonic-like resonances to a broad peak labelled as Q . The transition to the Q peak is abrupt and a jump in the photoluminescence energy can be observed at $n = n^*$. In photoluminescence, strict valley-conservation rules are again observed with light emitted from the Q peak solely in the momentum conserving (σ^+/σ^+) and (σ^-/σ^-) configurations.

Fig. 6.4(b) shows the valley contrast as a function of n for the different spectral features in photoluminescence for both circular polarisations of the excitation. The

valley contrast in the excitation polarisation σ^+ , $C(\sigma^+)$, is defined as

$$C(\sigma^+) = \frac{I(\sigma^+) - I(\sigma^-)}{I(\sigma^+) + I(\sigma^-)} \quad (6.2)$$

where I_{σ^+} (I_{σ^-}) is the light intensity in the σ^+ (σ^-) polarisation. A purely valley-conserving transition would have a valley contrast of +1.

At $n \approx 0$, the contrast only reaches around 40%, which can be explained by the non-resonant excitation [12]. Our exciton transition is indeed 20 meV lower in energy than our excitation laser.

As n increases, the contrast of X^0 decreases in one polarisation while it increases in the other polarisation. On the contrary, the X^- is highly valley conserving when excited with σ^+ -photons while clearly anti-valley-conserving when excited with σ^- -photons. This behaviour can be explained using the Suris' model as in Fig. 6.5(a): the X^- states exist only in the valley excited by σ^+ and will therefore be highly polarised. In the other polarisation, the excitons can be scattered to the other valley where they will be able to create the X^- , thus yielding a σ^+ photon.

When n reaches the critical density n^* , the polarisation behaviour changes completely and a high positive valley polarisation is observed again. This means that the ferromagnetic phase with a broken symmetry disappears suddenly to give rise to a new phase with the same symmetry as the one in the absence of electrons.

The electron's effective mass in the ferromagnetic phase can be computed using Suris' model of the absorption in a 2DEG (see Appendix A and Refs. [13, 14, 15]). The energetic difference between the upper and lower exciton-polaron is a measure of the Fermi level E_F with

$$\frac{d}{dE_F}(E(X^0) - E(X_{LE}^-)) = 1.2 = \underbrace{\left[\frac{\partial}{\partial n}(E(X^0) - E(X_{LE}^-)) \right]}_{\text{Experiment: } 2.93 \cdot 10^{-15} \text{ eVcm}^2} \underbrace{\frac{dn}{dE_F}}_{\frac{m_e}{\pi \hbar^2}} \quad (6.3)$$

where $E(X^0)$ and $E(X_{LE}^-)$ are the upper and lower exciton-polarons energies. From the experimental data, the n dependence of the energetic splitting $E(X^0) - E(X_{LE}^-)$ can be extracted to be $2.93 \cdot 10^{-15} \text{ eVcm}^2$. Accounting for two-bands filling, we can deduct that the electron mass in the ferromagnetic phase is $m_e = 0.97m_0$. This mass is significantly higher than the mass of $m_e = 0.45m_0$ extracted from DFT calculation. It is however in agreement with the $m_e \approx m_0$ mass deduced from the temperature dependence of

Shubnikov-de Haas oscillations in a recent electronic transport experiment [9]. The mass extracted here is subject to a systematic error as we cannot measure the carrier density. In comparison, in Chapter 5, the Q -peak would appear at a density $n^* = 6 \cdot 10^{12} \text{ cm}^{-2}$ and the slope $\frac{\partial}{\partial n}(E(X^0) - E(X_{LE}^-)) = 6.1 \cdot 10^{-15} \text{ eVcm}^2$. We are however confident that the mass extracted from the data presented in Fig. 6.3 is accurate as the transition to the Q -peak appears at $4.5 \cdot 10^{12} \text{ cm}^2$, density at which the density of states changes abruptly in the recent electronic transport experiment [9].

Knowing the mass in the interacting phase, it is possible to compute the Fermi level $E_F^* = 14 \text{ meV}$ at the phase transition. This value is significantly higher than the spin-orbit splitting of the conduction bands and underlines the robustness of the ferromagnetic phase: up to temperature of the order of $T^* = E_F^*/k_B \approx 150 \text{ K}$, we predict that the ferromagnetic phase is stable. Similar results as in Fig. 6.3 (a) were indeed obtained at $T = 40 \text{ K}$, showing no smearing of the phase transition.

In the paramagnetic phase we cannot extract an effective mass as we lack of a complete understanding of the optical response in this density regime. However, in the paramagnetic phase, the mass should be close to the DFT value of $m_e \approx 0.45$ [4], as a result of the reduced strength of Coulomb correlations. Note also that the exciton-polarons disappear in the paramagnetic phase. A likely reason for this would be a significant decrease of the trion binding energy induced by a decrease of the electron mass.

The optical response of a 2DEG at high density is described by the Fermi-edge singularity (FES) [16, 17, 18]. Absorption occurs at the Fermi level, as in Fig. 6.5(a), minus the residual electron-hole Coulomb interaction. In the case of a localised hole, the photoluminescence will form a band with a width of E_F and peaking at the Fermi-edge at the high energy side, due to the enhanced oscillator strength at the Fermi level [17]. In the finite mass case, the emission takes place from the bottom of the conduction band, as in Fig. 6.5(b) [16, 19]. Fig. 6.4(b) shows the Stoke's shift (i.e. the difference in energy between absorption and photoluminescence) as a function n for both (σ^+/σ^+) and (σ^-/σ^-) . Starting at n^* , the Stoke's shift increases monotonously with increasing carrier concentration. In WSe₂, at similar electron densities, Landau levels have been observed in the optical response [20], showing the quasi-single-particle nature of the optical response in this density regime [19]. We believe that the comparatively heavier effective electron mass of MoS₂ explains the difficulty to detect hints of Landau levels in our experiment [21].

It is known that electron-electron interaction renormalises parameters as the electron mass or g -factors. In the event of a second-order phase transition, a continuous evolution from the electron masses and g -factors toward the non-interacting parameters is expected

as n crosses n^* . Here, as the Stoke's shift is linear with n , no signs of a continuous second order phase transition can be detected.

6.4 Conclusion

We show compelling evidence that the ground-state of a MoS₂ 2DEG changes abruptly from a ferromagnetic state to a normal paramagnetic state when the carrier density n increases. The phase transition occurs at a carrier density $n^* = 4.5 \cdot 10^{12} \text{ cm}^{-2}$. No hints of a continuous renormalisation of the Fermi liquid parameters at the phase transition can be detected experimentally. We therefore conclude that the magnetic phase transition in monolayer MoS₂ is of the first order.

The first order nature of the phase transition was expected from the recent theoretical work by Miserev *et al.* [5]. Its experimental observation underlines the importance of non-analycities in the expansion of the free energy in term of the magnetisation.

Bibliography

- [1] Mermin, N. D. & Wagner, H. Absence of ferromagnetism or antiferromagnetism in one- or two-dimensional isotropic Heisenberg models. *Phys. Rev. Lett.* **17**, 1133 (1966).
- [2] Mak, K. F., Lee, C., Hone, J., Shan, J. & Heinz, T. F. Atomically thin MoS₂: A new direct-gap semiconductor. *Phys. Rev. Lett.* **105**, 136805 (2010).
- [3] Xiao, D., Liu, G.-B., Feng, W., Xu, X. & Yao, W. Coupled spin and valley physics in monolayer of MoS₂ and other group-VI dichalcogenides. *Phys. Rev. Lett.* **108**, 196902 (2012).
- [4] Kormányos, A., Zoloyomi, V., Drummond, N. D. & Burkard, G. Spin-orbit coupling, quantum dots , and qubits in monolayer transition metal dichalcogenides. *Phys. Rev. X* **4**, 011034 (2014).
- [5] Miserev, D., Klinovaja, J. & Loss, D. Spontaneous Symmetry Breaking in Monolayers of Transition Metal Dichalcogenides. *arXiv e-prints* arXiv:1902.07961 (2019). [arXiv:1902.07961](https://arxiv.org/abs/1902.07961).
- [6] Maslov, D. & Chubukov, A. Nonanalytic paramagnetic response of itinerant fermions away and near a ferromagnetic quantum phase transition. *Phys. Rev. B* **79**, 075112 (2009).
- [7] Roch, J. *et al.* Spin-polarized electrons in monolayer MoS₂. *Nat. Nanotechnol.* **14**, 432–436 (2019).
- [8] Cadiz, F. *et al.* Excitonic linewidth approaching the homogeneous limit in MoS₂-based van der Waals heterostructures. *Phys. Rev. X* **7**, 021026 (2017).
- [9] Pisoni, R. *et al.* Interactions and magnetotransport through spin-valley coupled Landau levels in monolayer MoS₂. *Phys. Rev. Lett.* **121**, 247701 (2018).
- [10] Ju, L. *et al.* Photoinduced doping in heterostructures of graphene and boron nitride. *Nat Nanotechnol.* **9** (2014).

- [11] Epping, A. *et al.* Quantum transport through MoS₂ constrictions defined by photodoping. *J Phys Condens Matter.* **30** (2018).
- [12] Mak, K. F., He, K., Shan, J. & Heinz, T. F. Control of valley polarization in monolayer MoS₂ by optical helicity. *Nat. Nanotechnol.* **7**, 494 (2012).
- [13] Suris, R. A. *et al.* Excitons and trions modified by interaction with a two-dimensional electron gas. *Phys. Status Solidi B* **227**, 343–352 (2001).
- [14] Sidler, M. *et al.* Fermi polaron-polaritons in charge-tunable atomically thin semiconductors. *Nat. Phys.* **13**, 255–261 (2016).
- [15] Efimkin, D. K. & MacDonald, A. H. Many-body theory of trion absorption features in two-dimensional semiconductors. *Phys. Rev. B* **95**, 035417 (2017).
- [16] Hawrylak, P. Optical properties of a two-dimensional electron gas: Evolution of spectra from excitons to Fermi-edge singularities. *Phys. Rev. B* **44**, 3821 (1991).
- [17] Skolnick, M. S. *et al.* Observation of a many-body edge singularity in quantum-well luminescence spectra. *Phys. Rev. Lett.* **58**, 2130 (1987).
- [18] Huard, V., Cox, R. T., Saminadayar, K., Arnoult, A. & Tatarenko, S. Bound states in optical absorption of semiconductor quantum wells containing a two-dimensional electron gas. *Phys. Rev. Lett.* **84**, 187 (2000).
- [19] Uenoyama, T. & Sham, L. J. Effect of finite hole mass on edge singularities in optical spectra. *Phys. Rev. Lett.* **65**, 1048 (1990).
- [20] Wang, Z., Shan, J. & Mak, K. F. Valley- and spin- polarized Landau levels in monolayer WSe₂. *Nat. Nanotechnol.* **12**, 144–150 (2017).
- [21] Kormanyos, A. *et al.* k.p theory for two-dimensional transition metal dichalcogenides semiconductors. *2d Mater.* **2**, 022001 (2015).

Chapter 7

Conclusion

In the introduction, I placed this work within the context of understanding the physics of transition metal dichalcogenides. The atomic thickness of their monolayers make them truly two-dimensional materials. The different studies presented in this Thesis illustrate very well the challenges of understanding the physics of these materials. While a small polarisability of excitons in monolayer MoS₂ was expected (Chapter 4), the spontaneous creation of a spin-polarised 2DEG in MoS₂, as discussed in Chapter 5 was unexpected. The physics behind the spin-polarisation was further investigated in Chapter 6, where we have found that the standard phase transition theory (Ginzburg-Landau) cannot be applied to the doped MoS₂ monolayer case.

The small polarisability of excitons in monolayer MoS₂ has important implications for the design of optoelectronic devices. A main result of our work is that a control of the emission wavelength of a monolayer of transition metal dichalcogenide cannot be easily controlled by an out-of-plane electric field. Nevertheless, van der Waals heterostructure also present great opportunities to tailor the excitonic emission energy. By stacking monolayers of different materials within van der Waals heterostructures, it becomes possible to create heterostructures where the lowest energy excitation is a spatially indirect exciton: the electron and the hole components of such an exciton live in the different materials. This spatial separation of the electron to the hole gives the indirect excitons a permanent dipole moment. Due to the large binding energy of excitons in TMDs, the emission energy of indirect excitons can be controlled over tens of meV using an external electric field.

The spin-polarisation of the electronic ground-state in monolayer MoS₂ presented in Chapter 5 and further discussed in Chapter 6 has important consequences to the understanding of the physics in two dimensions. The Coulomb interaction is so strong in monolayer MoS₂ that electrons prefer populating a single spin-state, despite the large kinetic energy cost. The first-order nature of the phase transition from a ferromagnetic state to a paramagnetic state observed in Chapter 6 shows that the roots of the spin-

polarisation resides in high-orders of the Coulomb interaction. Recent theoretical work by Miserev *et al.* has shown that Coulomb interaction can explain the first order nature of the phase transition. Although the importance of non-analyticities from high orders of the Coulomb interaction in the thermodynamic potential was foreseen already for standard Fermi-liquids, monolayer MoS₂ is the first material system in which these high orders of Coulomb interaction dominates the complete dynamics of the system.

Appendix A

Supplementary information to chapter 5 “Spin-Polarized Electrons in Monolayer MoS₂”

In chapter 5 “Spin-Polarized Electrons in Monolayer MoS₂”, optical susceptibility measurement is presented as a tool to investigate the ground-state of a two-dimensional electron gas (2DEG) formed by a monolayer of MoS₂. We found that the ground-state of the 2DEG is spin-polarised, inter-valley Coulomb interaction likely to be responsible for the spontaneous symmetry breaking. Here, we provide more details about the experiment, the data analysis, the sample and the modelling.

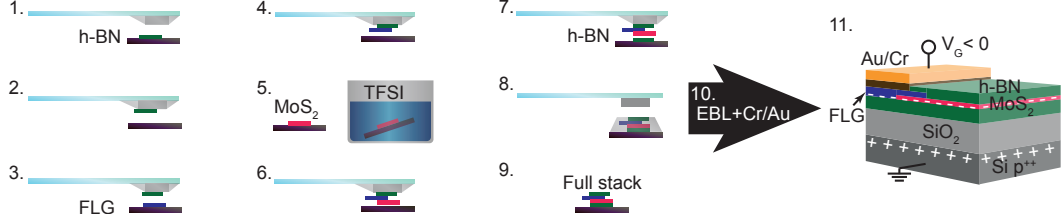


Fig. A.1. **Sample fabrication.** Using a PDMS/PC stamping procedure, flakes are picked up (1-7) and stacked on the PC film. At the last step (8), the PC film is left on a SiO₂/Si substrate by heating. After dissolving the PC film (9), electron beam lithography (EBL) and contact deposition can be performed (10). The final sample structure is sketched in (11).

A.1 Sample fabrication

Van der Waals heterostructures were fabricated by stacking two-dimensional materials via a dry-transfer technique[1], as depicted in Fig. A.1. A polydimethylsiloxane (PDMS) stamp with a thin polycarbonate (PC) layer is used to pick up flakes exfoliated on SiO₂(300 nm)/Si substrates. Exfoliation was carried out from bulk crystals (natural MoS₂ crystal from SPI Supplies, synthetic h-BN[2], and natural graphite from NGS Naturgraphit). MoS₂ monolayers were treated by a bis(trifluoromethane)sulfonimide (TFSI) solution, following Ref. [3], before full encapsulation between h-BN layers. Few-layer graphene (FLG) was employed as a contact electrode to MoS₂[4]. Metal contacts to the FLG were patterned by electron-beam lithography (EBL) and subsequent metal deposition of Au (45 nm)/Cr (5 nm).

The capacitance of the device was estimated using electrostatics: the MoS₂ flake and the p-doped silicon are considered as two electrodes separated by the thickness d_{BN} of the bottom h-BN and the thickness d_{SiO_2} of the SiO₂. The capacitance per unit area is then given by

$$C = \frac{1}{\frac{d_{\text{BN}}}{\epsilon_{\text{BN}}} + \frac{d_{\text{SiO}_2}}{\epsilon_{\text{SiO}_2}}} \quad , \quad (\text{A.1})$$

where $\epsilon_{\text{BN}} = 3.76$ [5] and $\epsilon_{\text{SiO}_2} = 3.9$ are the dielectric constants of h-BN and SiO₂, respectively. Using $d_{\text{BN}} = 10$ nm and $d_{\text{SiO}_2} = 300$ nm, we obtain $C = 11.1 \pm 0.5$ nFcm⁻², where an overall 5% uncertainty in the layers thicknesses is taken into account.

Due to the small size of the sample (~ 10 μm²), it is difficult to measure directly its absolute \sim fF capacitance. Fig. A.2 shows the gate voltage dependence of the leakage current through the oxide layer at cryogenic temperature (4 K). No gate leak (> 10 GΩ) was observed up to 100 V between the top electrode and the bottom gate.

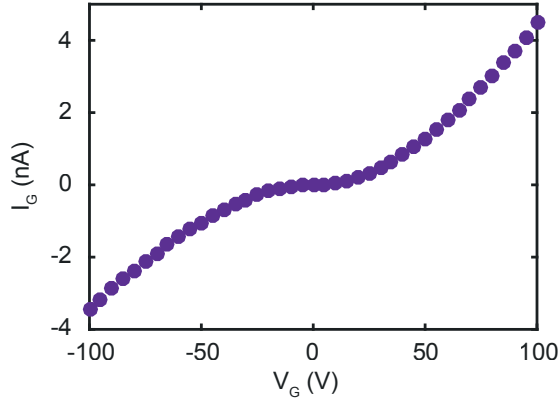


Fig. A.2. **Electrical characterization of our device.** Leakage current I_G through the oxide layer as a function of the gate voltage V_G at cryogenic temperature (4 K).

Experimentally, we apply a voltage V_G to inject carriers in the 2DEG. For a capacitive device, the carrier concentration n is given by $n = CV_G$ and it is expected that $n = 0$ when $V_G = 0$. Before sweeping V_G , the optics tell us that our as-fabricated devices are undoped: the optical response consists only of the neutral exciton. However, as a combined consequence of photo-doping effect [6, 7] and charge trapping [8] at the different interfaces in the van der Waals heterostructure, the device exhibits hysteresis when V_G is swept in a loop. When we increase V_G from 0 to 100 V for the first time, the optical response remains the same, suggesting that the Fermi level is pinned to the bottom of the conduction band of MoS₂. Taking advantage of this hysteresis, we can set the $n \approx 0$ density when $V_G(n \approx 0) = 100$ V. Optically, the absence of negatively charged excitons in the absorption spectra in both polarisations can be used to attest the absence of electrons in the 2DEG. As soon as we sweep the voltage down to a lower voltage, the optical response changes, attesting the injection of carriers in the monolayer MoS₂. At different gate voltages, n reads

$$n(V_G) = -C(V_G(n \approx 0) - V_G). \quad (\text{A.2})$$

In the main text, we use equation (A.2) to determine the electron density n .

A.2 Experimental setup

The absorption spectra displayed in Fig. 2 in the main text were recorded with the setup sketched in Fig. A.3. The red part of a white (Osram warm white) light emitting diode

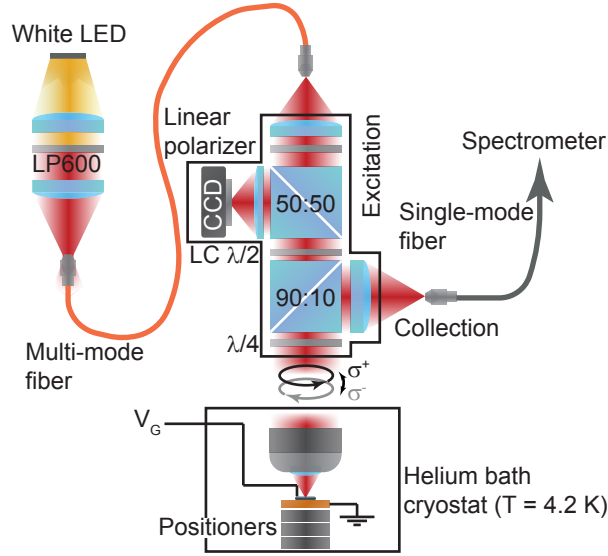


Fig. A.3. **Experimental setup.**

(LED) is filtered by a 600 nm longpass filter and coupled into a multi-mode fiber. The output of the fiber is connected to a home-built microscope. A CCD camera mounted on the microscope is used to visualise the sample. In the microscope, the light is first sent through a linear polarizer. A computer controlled liquid crystal (LC) retarder that can produce a $+\lambda/2$ or $-\lambda/2$ retardance of the initial beam is used to produce two perpendicular linear polarizations on demand. An achromatic quarter-wave plate retarder ($\lambda/4$) is subsequently used to produce circularly polarized light. By controlling the voltage on the LC retarder, we can then circularly polarize the LED light with right- or left- handed orientation. The circularly polarized light goes then in a helium bath cryostat at 4.2 K and is focused on the sample using a microscope objective (NA=0.65). The position of the sample with respect to the focus can be adjusted with cryogenic nanopositioners. The reflected light is coupled into a single-mode fiber, ensuring a confocal detection, and sent to a spectrometer. Light was dispersed by a 1500 grooves per millimeter grating, before being focused onto a liquid-nitrogen cooled charged coupled device (CCD) array. The spectral resolution of the spectrometer setup is 0.05 nm. In this way, reflectivity spectra were acquired.

A.3 Reflectivity of a thin film: determination of the susceptibility

Monolayers MoS₂ or h-BN are visible when placed on a SiO₂ substrate. Optical contrast is induced by interferences in the thin films. Thin film interferences thus play an important role when measuring the reflectivity of a van der Waals heterostructure.

For a monolayer placed on a thick substrate, the system can be modeled by a three layer system, as depicted in Fig. A.4(a). A thin-film is at the interface between two semi-infinite systems, namely vacuum and the SiO₂ layer. As the monolayer thickness d is much smaller than the wavelength of light λ , the differential reflectivity of the monolayer $\frac{\Delta R}{R}$ at normal incidence can be written as [9]:

$$\frac{\Delta R}{R} = -\frac{8\pi d n_1}{\lambda} \Im m \left(\frac{\epsilon_1 - \tilde{\epsilon}_2}{\epsilon_1 - \epsilon_3} \right), \quad (\text{A.3})$$

where ϵ_j is the dielectric function of the j -th layer and n_1 is the refractive index of the first medium. The meaning of the tilde in $\tilde{\epsilon}_2$ will be explained later. In the linear response approximation, $\epsilon_j = 1 + \chi_j$, where χ_j is the optical susceptibility of layer j . As the first medium is air, $\epsilon_1 = 1$ and the numerator in equation (A.3) simplifies to $\epsilon_1 - \tilde{\epsilon}_2 = 1 - (1 + \tilde{\chi}_2) = -\tilde{\chi}_2$. Assuming that the glass substrate has a negligible absorption ($\Im m(\epsilon_3) = 0$), equation (A.3) can then be rewritten as,

$$\Im m(\tilde{\chi}_2) = \underbrace{\frac{\lambda(1 - \epsilon_3)}{8\pi d}}_{\beta} \frac{\Delta R}{R} \approx -49.1 \frac{\Delta R}{R}, \quad (\text{A.4})$$

where we use an effective monolayer thickness $d = 0.65$ nm, $\epsilon_3 = 2.25$ and a constant wavelength $\lambda = 642$ nm, corresponding to the centre position of the spectrometer grating during the measurements. Equation (A.4) allows a measured $\frac{\Delta R}{R}$ to be converted into the imaginary part of the susceptibility. We define here $\beta = \frac{\lambda(1 - \epsilon_3)}{8\pi d} \approx -49.1$.

In our sample, we have more than three layers. In the experiment, when we measure $\frac{\Delta R}{R}$, we actually probe an effective susceptibility $\tilde{\chi}_2$ of the MoS₂ monolayer. Reflection on the SiO₂/Si interface, as well as the multiple thin-film interferences in the h-BN layers will indeed mix the real and imaginary part of the dielectric function of the MoS₂.

As the susceptibility is a complex number, a phase factor $e^{i\zeta}$ can be used [10, 11] to mix the imaginary and real part of the dielectric function of the monolayer MoS₂. The effective susceptibility $\tilde{\chi}_2$ of the thin-film that we probe in our measurement is then related to the susceptibility χ_2 of MoS₂ by $\tilde{\chi}_2 = e^{-i\zeta} \chi_2$.

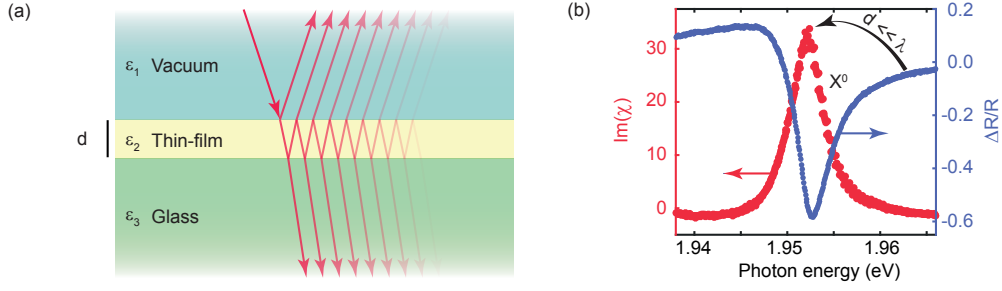


Fig. A.4. **From reflectivity to the optical susceptibility.** (a) Three layer system: light comes from a semi-infinite medium 1 (top) and is reflected at the thin-film (middle). Multiple interferences in the thin-film create optical interferences. (b) Using a Kramers-Kronig relation, the raw reflectivity data (blue) around the X^0 energy at zero electron concentration can be turned into a Lorentzian absorption lineshape. Here, we used a phase factor $\zeta = 0.69$ rad to account for multiple thin-film interferences.

We are not interested in the value of the effective susceptibility, but we want to access to the value of χ_2 , which is intrinsic to MoS₂. However, equation (A.4) links the measured $\frac{\Delta R}{R}$ to the effective optical susceptibility

$$\frac{\Delta R}{R} = \frac{1}{\beta} \text{Im}(\tilde{\chi}_2) = \frac{1}{\beta} \tilde{\chi}_2'' , \quad (\text{A.5})$$

where we decomposed $\tilde{\chi}_2$ in its real and imaginary part $\tilde{\chi}_2 = \tilde{\chi}_2' + i\tilde{\chi}_2''$. As before, $\beta \approx -49.1$. By definition, $\chi_2 = e^{i\zeta} \tilde{\chi}_2$ and therefore

$$\chi_2'' = \cos(\zeta) \tilde{\chi}_2'' + \sin(\zeta) \tilde{\chi}_2' . \quad (\text{A.6})$$

Our experiment measures $\frac{\Delta R}{R} = \frac{1}{\beta} \tilde{\chi}_2''$. In order to compute $\tilde{\chi}_2''$ from equation (A.6), we need to know the value of $\tilde{\chi}_2'$. The causality of the dielectric function $\tilde{\chi}_2$ implies that we can make use of the Kramers-Kronig relation in equation (A.6).

$$\chi_2''(\omega) = \cos(\zeta) \tilde{\chi}_2'' + \sin(\zeta) \underbrace{\frac{2}{\pi} \mathcal{P} \int_0^\infty \frac{\omega' \tilde{\chi}_2''(\omega')}{\omega'^2 - \omega^2} d\omega'}_{\tilde{\chi}_2'} , \quad (\text{A.7})$$

where ω denotes the angular frequency. Using equation (A.4), we can express the imaginary part of the dielectric function of MoS₂ as a function of the differential reflectivity

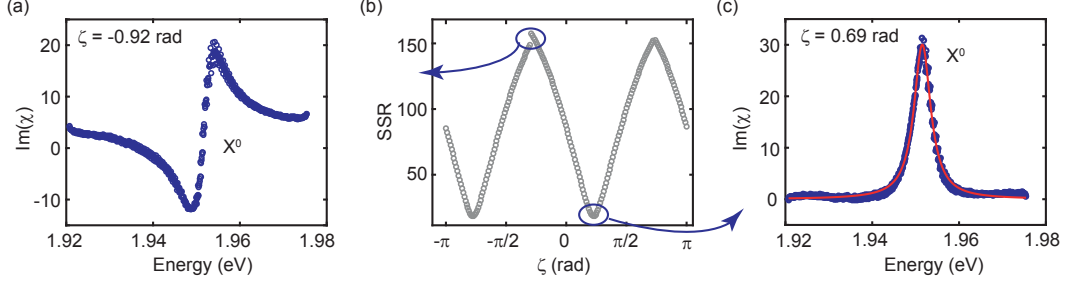


Fig. A.5. **Kramers-Kronig and ζ .** The phase factor ζ accounting for multiple thin-film interferences is varied such that the X^0 resonance at near zero electron density is Lorentzian. After the Kramers-Kronig transformation, the X^0 resonance is non-Lorentzian (a) or Lorentzian (c), depending on the value of ζ . (b) The sum of the squared residues (SSR) of a Lorentzian fit of the data is used to find the optimal $\zeta = 0.69$ rad.

$\frac{\Delta R}{R}$ that we measure experimentally:

$$\chi_2'' = \beta \left(\sin(\zeta) \frac{2}{\pi} \mathcal{P} \int_0^\infty \frac{\omega' \frac{\Delta R}{R}(\omega')}{\omega'^2 - \omega^2} d\omega' + \cos(\zeta) \frac{\Delta R}{R} \right). \quad (\text{A.8})$$

As interference effects depend on the wavelength, the phase $e^{i\zeta}$ also depend on the wavelength ($\zeta = \zeta(\omega)$). However, as the wavelength range we access in a single spectrum is small compared to the wavelength itself, to first order, we can set ζ to a constant value.

The imaginary part of the susceptibility of a neutral exciton (X^0) has a Lorentzian lineshape in the absence of free carriers. A differential reflectivity spectrum at near zero electron density is transformed using the Kramers-Konig relation in equation (A.8) with different values of ζ to compute the susceptibility. The integral appearing in equation (A.8) is only computed over the wavelength range corresponding to the experimental spectra. The value of ζ for which the X^0 has a Lorentzian lineshape in the absence of carriers is then used for transforming the spectra at higher electron densities. Fig. A.5(b) shows the sum of the squared residues (SSR) of a Lorentzian fit of the exciton resonance. With $\zeta = 0.69$ rad, the X^0 is well described by a Lorentzian, as in Fig. A.5(c). On the other hand, in A.5(a), at a value of $\zeta = -0.92$ rad, the residues are maximized and the data cannot be fitted by a Lorentzian. Fig. A.4(b) shows the differential reflectivity of X^0 as measured and the imaginary part of the susceptibility extracted using equation (A.8).

The optical susceptibility spectrum of the X^0 in Fig. A.5(c) is typical for our sample.

The line-width of the X^0 in the absence of electron is extracted from a Lorentzian fit. We measure a line-width of 5 meV, close to the state-of-the-art (4 meV) observed in absorption in samples with similar structure [12]. As the exciton life-time was measured to be sub-picosecond [13], the resonances observed in our susceptibility spectra are mostly homogeneously broadened, demonstrating a superior sample quality.

In the main text, we present absorption as a tool to non-invasively probe the 2DEG. To attest that our probe is non-invasive, we compute here the density of photo-generated electron-hole pairs and compare it to the injected electron density.

The total power of the LED sent on the sample is $P_{LED} = 500$ nW. The LED has a broad spectrum spreading on $\Gamma_{LED} \approx 100$ meV. The power density of the LED can be estimated to be $I_{LED} = P_{LED}/\Gamma_{LED} \approx 5$ nWmeV⁻¹.

The main absorption of the sample occurs when $n \approx 0$. In this density regime, the absorption is dominated by the X^0 at an energy of $E(X^0) = 1.95$ eV. We obtain an upper bound for the density of photo-generated electron-hole pairs if we assume that all the photon coming from the LED are absorbed at the X^0 resonance. As the X^0 resonance has a line-width of $\Gamma_{X^0} = 5$ meV, the absorbed power is $P_{abs} = I_{LED}\Gamma_{X^0} \approx 25$ nW. The focal spot of the LED coming from a multi-mode fiber on the sample has an area of $A \approx 100$ μm^2 . The electron-hole pair generation rate s_{eh} can be therefore estimated as $s_{eh} = \frac{P_{abs}}{AE(X^0)} \approx 5 \times 10^{17}$ s⁻¹cm⁻².

The average population of electron-hole pair is given by the product of the generation rate s_{eh} with the lifetime of the electron-hole pairs τ_{eh} . The electron-hole pair lifetime in MoS₂ can be extracted from the homogeneous line-width obtained from four wave mixing experiments. It was measured to be $\tau_{eh} < 1$ ps [13]. Using $\tau_{eh} = 1$ ps, we can estimate $n_{eh} = s_{eh}/\tau_{eh} \approx 5 \times 10^5$ cm⁻². As the typical electron concentrations are $n > 10^{11}$ cm⁻², n is more than 5 orders of magnitude larger than n_{eh} , showing that our optical probe can be considered as non-invasive.

In order to evaluate the differential reflectivity $\frac{\Delta R}{R}$, we compare a reflectivity spectra R obtained on the MoS₂ flake at a given gate voltage with a reference spectrum R_0 , such that $\Delta R = R - R_0$. As the trion features in the reflectivity have a weak signal ($\frac{\Delta R}{R} \approx 5\%$), special attention need to be taken in the choice of the reference spectrum. A small interference pattern (amplitude of $\approx 5\%$) appears indeed in the raw reflectivity spectra due to reflections in the experimental setup. As they have approximatively the same amplitude as the weak signals that we want to measure, they can only be canceled by a careful choice of the reference. Ideally, R_0 could be acquired on the h-BN, at a

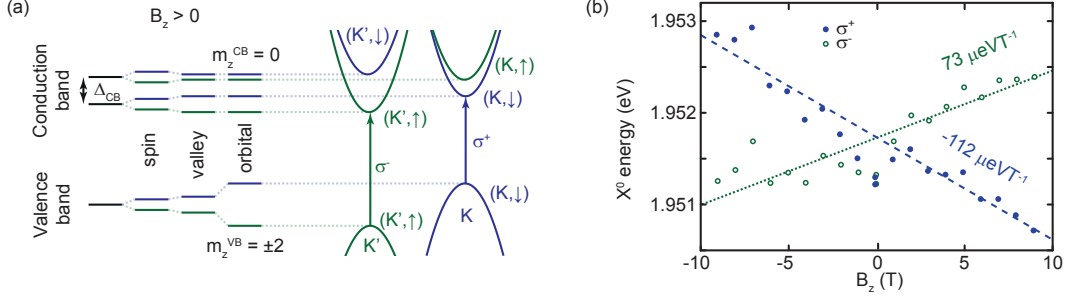


Fig. A.6. **Valley Zeeman effect.** (a) When increasing the magnetic field from $B_z = 0$ to a finite value, the energy of the different bands changes. Valley pseudo-spin, spin and orbital momentum contribute to the energy shift of a band. (b) Energy of the X^0 at different magnetic fields in the two circular polarizations. The energy dependence of the exciton transition energies in both polarisations are extracted from the linear fit. In σ^+ (σ^-) polarisation, the exciton energy varies with magnetic field as -112 (73) $\mu\text{eV}\text{T}^{-1}$.

position next to the MoS₂ flake. However, by moving the sample, the optical path length changes slightly and the interference pattern appearing in the raw reflectivity spectra does not cancel. The reflectivity spectra R change significantly with varying electron density. The median of the several spectra obtained while sweeping the gate voltage can therefore be used as the reference R_0 : the features appearing in $\frac{\Delta R}{R}$ will be then only be related to changes in electron density. As R and R_0 are all obtained at the same position, the interference pattern is canceled in ΔR and very clean differential reflectivity spectra can be acquired.

A.4 Selection rules and valley Zeeman effect

For monolayer MoS₂, the optical response depends on the valley in which the photo-generated electron-hole pair is created. Broken inversion symmetry ensures that the electrons from the same band in the two valleys carry opposite spin, angular momentum and valley angular momentum. An out-of-plane magnetic field shifts a band in energy by a Zeeman shift ΔE :

$$\Delta E = \underbrace{\Delta_s}_{\text{spin}} + \underbrace{\Delta_\alpha}_{\text{angular momentum}} + \underbrace{\Delta_v}_{\text{valley}}, \quad (\text{A.9})$$

where $\Delta_s = \frac{1}{2}g_s\mu_B s_z B_z$ and $\Delta_v = \frac{1}{2}g_v\mu_B \tau_z B_z$, with $g_s = 1.98$ [14] and $g_v = 0.75$ [14]. s_z and τ_z are the spin and pseudo-spin (valley) operators perpendicular to the monolayer. We write $\tau_z = 1(\tau_z = -1)$ for the valley pseudo-spin corresponding to the K (K')

valley. The states at the conduction band edge are mostly made from d_{z^2} orbital with a zero orbital angular momentum $m_{z,\tau_z}^{CB} = 0$, yielding $\Delta_\alpha^{CB} = 0$. On the other hand, the valence band is mostly composed of d_{xy} and $d_{x^2-y^2}$ orbitals with a finite orbital angular momentum $\hbar m_{z,\tau_z}^{VB} = -2\hbar\tau_z$ [15]. In the valence band, the angular momentum contribution to the Zeeman shift is finite: $\Delta_\alpha^{VB} = \mu_B m_{z,\tau_z}^{VB} B_z$.

An optical transition must satisfy conservation of the total angular momentum, spin and momentum. The conservation laws are enforced by the selection rules that dictate which transitions can be coupled by the light field. In transition metal dichalcogenides, as the band edges are located at the K and K' points of the Brillouin zone, it was shown that circularly polarised light can be used to address a specific valley [16]. A $\sigma^+(\sigma^-)$ polarised photon couples the top valence band states to the bottom conduction band at the K (K') valley.

When in $B_z > 0$, the Zeeman shifts of two bands coupled via an optical transition have the same spin and valley contribution as a result of conservation rules. For an inter-band transition, only the orbital angular momentum contribution differs between the two coupled bands, as $m_{z,\pm K}^{VB} \neq m_{z,\pm K}^{CB}$. The neutral exciton (X^0) correspond to the coupling of the top valence band to the bottom conduction band. Its transition energy $E(X^0)$ is dictated by

$$E(X^0) = E_{CB} - E_{VB} - E_b(X^0), \quad (\text{A.10})$$

where E_{CB} and E_{VB} are the energies of states in the conduction band and valence band, respectively, and $E_b(X^0)$ is the exciton binding energy. We define $E_{CB} - E_{VB} = E_g^{B_z=0}$. In magnetic field, $E(X^0)$ is modified by the Zeeman shift of both conduction and valence band. As s_z and τ_z are the same in an optical transition, the spin and valley contributions cancel:

$$E(X^0) = E_g^{B_z=0} + (\Delta_s + \Delta_v) - (\Delta_s + \Delta_v + \Delta_\alpha^{VB}) - E_b(X^0)$$

$$E(X^0) = E_g^{B_z=0} - \mu_B m_{z,\tau_z}^{VB} B_z - E_b(X^0). \quad (\text{A.11})$$

As m_z^{VB} is opposite in the two valleys, the X^0 energy in a finite magnetic field is different when observed in different circular polarisation of light. Fig. A.6(a) depicts the Zeeman shifts of the different bands and shows that, when in magnetic field, the energy of the X^0 is different for the two circular polarisations of light. The energy difference $\Delta E(X^0)$ between $E(X^0)$ in the two valleys is given by $|\Delta E(X^0)| = 2\mu_B |m_{z,\tau_z}^{VB}| B_z$.

The absorption energy $E(X^0)$ of the X^0 can be extracted from our experimental data. Fig. A.6(b) displays $E(X^0)$ as a function of the magnetic field. It is clear that for posi-

tive magnetic fields the energy of X^0 increases for σ^- polarization, while the opposite is seen for σ^+ polarization. The energetic difference $\Delta E(X^0)$ is extracted from the fits and is $185 \mu\text{eV T}^{-1}$, yielding $|m_{z,\tau_z}^{VB}| = 1.6$, close to the expected value of 2, but differing from measured values on samples with similar structure [12]. The measurement in Fig. A.6(b) is used to verify that σ^+ light addresses the K valley.

We can make use of the valley Zeeman effect to verify that the optical selection rules are robust in our experiment. In magnetic field, the X^0 transition energy changes in the two polarizations of light, but its lineshape remains constant. If selection rules were not conserved in our experiment, the absorption spectrum in one polarization would contain a small amount of the features of the other polarization. A mixing of the two polarisations can be detected by computing the integrated difference between the spectra obtained in the two polarisations. We show here that up to noise level, the integrated difference between the two susceptibility spectra goes down to zero when one of the spectrum is shifted in energy by the Zeeman shift.

The absorption signal S^\pm in polarization σ^\pm can be written as

$$S^\pm(E_i) = \bar{S}_i^\pm + N_i^\pm, \quad (\text{A.12})$$

where the index i accounts for the discrete nature of the energy E axis in the experimental spectra, \bar{S}_i^\pm is the absorption at energy E_i , and N_i^\pm is an independent random variable with zero mean modelling noise on the data. To prove that the optical selection rules are conserved in our measurements, we compute the sum of the absolute value of the difference ΔS between the two spectra when they are shifted in energy by ΔE_j :

$$\Delta S(E_j) = \sum_i |S^+(E_i) - S^-(E_i + \Delta E_j)|. \quad (\text{A.13})$$

The expected value and variance of $\Delta S(E_j)$ are given by

$$\mathbb{E}(\Delta S(E_j)) = \sum_i |\bar{S}^+(E_i) - \bar{S}^-(E_i + \Delta E_j)| \quad (\text{A.14})$$

and

$$\text{Var}(\Delta S(E_j)) = \text{Var}\left(\sum_i N_i^+\right) + \text{Var}\left(\sum_i N_i^-\right). \quad (\text{A.15})$$

The Central Limit Theorem implies that a sum of random variables tends to a Gaussian random variable as the number of elements in the sum increases. Furthermore, the

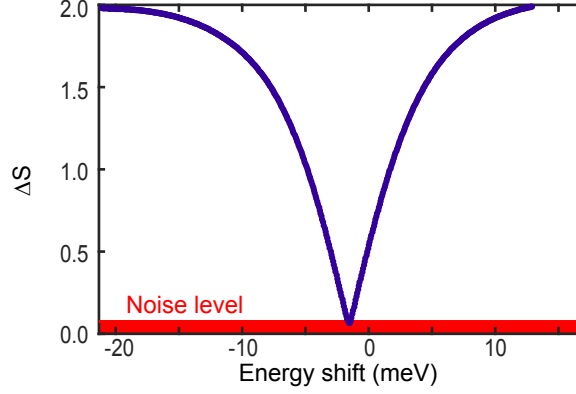


Fig. A.7. **Robustness of optical selection rules.** The optical selection rules are verified with an accuracy reaching the noise level. ΔS is the integrated difference between the X^0 spectra at 9 T in the two polarizations (*see* equation (A.13)). The spectra are shifted in energy. The two spectra are identical when the energy shift is equal to the valley Zeeman shift.

variance of the sum is given by the sum of the variances of the independent random variables in the sum. Here, assuming that the noise amplitude is the same at all points and in both polarizations (*i.e.* $\text{Var}(N_i^+) = \text{Var}(N_j^-)$, $\forall i, j$), we have

$$\text{Var}(\Delta S(E_j)) = 2h\sigma_N^2, \quad (\text{A.16})$$

with σ_N is the standard deviation of the noise N and h the number of elements in the sum. σ_N was measured on the spectra in a spectral region away from the X^0 resonance. Fig. A.7 shows ΔS as a function of detuning when S^\pm are normalized such that

$$1 = \sum_i S^\pm(E_i). \quad (\text{A.17})$$

If the detuning is large, ΔS is 2 as the two spectra do not overlap at all. When the detuning reaches the value of the Zeeman shift, ΔS should reach zero. However, noise prevents reaching a zero value. The red domain in Fig. A.7 shows possible values of ΔS taking noise into account, in the case of perfect selection rules. As the minimal value of the measured ΔS (blue curve) falls in the noise level (red domain) at the value of the Zeeman shift, we can conclude that selection rules are conserved to the detection limit of our setup.

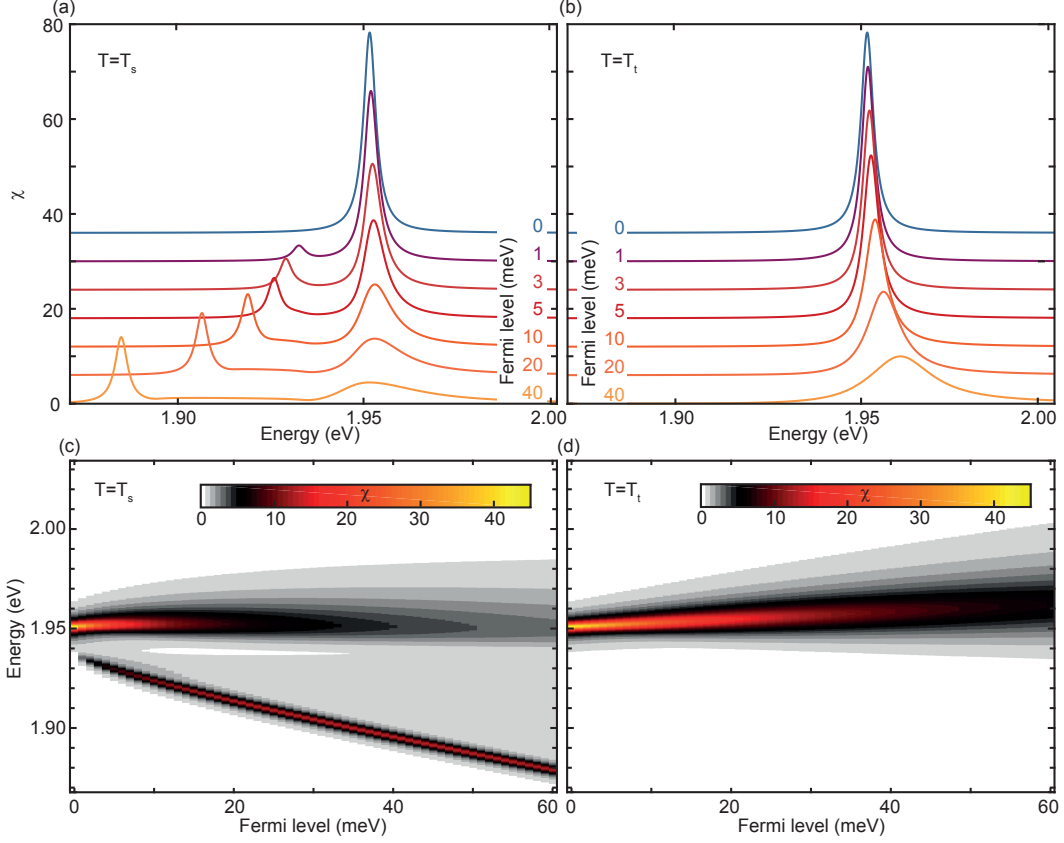


Fig. A.8. **Suris model of 2DEG optical susceptibility.** Optical susceptibility of an exciton simulated following equation (A.19). The exciton interact with a fully spin-polarised Fermi sea. (a) The electron of the photo-generated excitons have opposite spin to that of the electrons of the Fermi sea. Excitons interact attractively with electrons (singlet collisions). A low energy peak emerges around 1.9 eV as consequence of interactions, while the X^0 stays at 1.95 eV. (b) The electron of the photo-generated excitons have the same spin as the electrons of the Fermi sea. Excitons experience a repulsive interaction with electrons (triplet collisions). The X^0 peak becomes more asymmetrical toward the high energy side with higher electron density. (c) Optical susceptibility in the case of singlet collision as a colormap at different Fermi levels and different photon energies. (d) Same as in (c) but for triplet collisions. The simulations presented here were obtained using $m_{CB}^* = 0.44$ [14], $m_{VB}^* = 0.5$ [17], $E_b(X^0) = 260$ meV, $E_b(X^-) = 17$ meV, $E(X^0) = 1.952$ eV, $\alpha = 1$, and $\gamma = 2.0$ meV.

A.5 Theory of trion absorption in a 2DEG

When the Fermi level E_F is of the same order of magnitude as the trion binding energy $E_b(X^-)$ and less than the exciton binding energy $E_b(X^0)$, the description of the trion as a three particle body is no longer valid [18, 19, 20]. In this limit, trions appear as a consequence of the exciton - Fermi sea interaction: the exciton energy splits in two

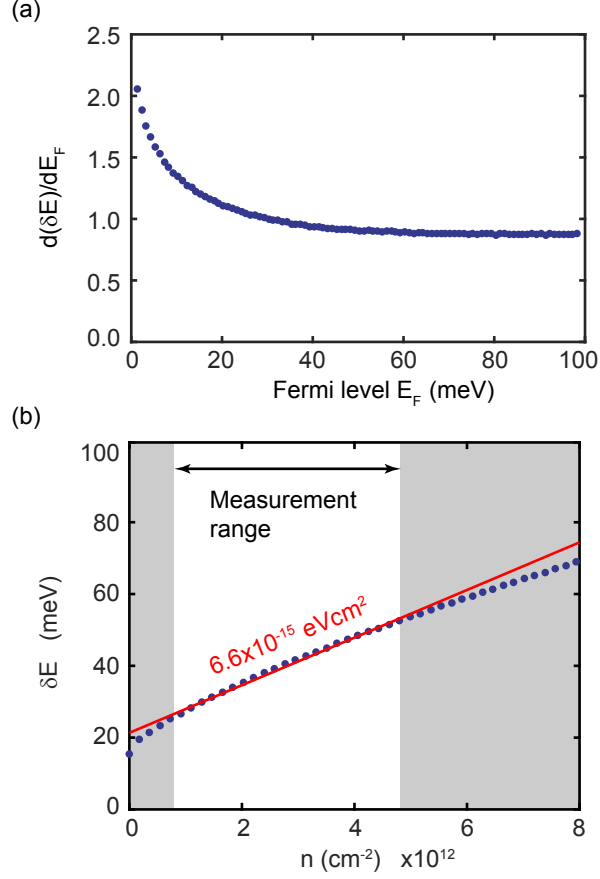


Fig. A.9. **Optics as a measure of the Fermi level.** The susceptibility in equation (A.19) can be computed at various Fermi-level, as in Fig. A.8. From the simulated spectra we can extract the energy of the X^0 and of the X^- . (a) Gradient of δE as a function of the Fermi level. At high Fermi level, the gradient tends to a value of 1. (b) δE as a function of the carrier density. The red solid line is a linear fit of the simulated δE in the range of densities where trion and exciton can be experimentally resolved in the susceptibility spectra. The parameters used for this simulation are the same as those used in Fig. A.8.

branches when it interacts with a Fermi sea, forming excitons and trions. In this picture, it is more accurate to name the two branches in terms of Fermi polarons [21, 22]. The upper energy branch, the exciton, is then the repulsive polaron, while the trion forming the lower energy branch is referred to as the repulsive polaron [21].

Photo-generated excitons interact with the Fermi-sea in two ways: either an exciton captures an electron and creates an X^- (attractive interaction) or an electron scatters off an exciton (repulsive interaction). These two interactions contributes to the self-energy

(Ξ) in the 2D exciton optical susceptibility [18, 19, 20, 23].

$$\chi(\hbar\omega) = -2|d_{cv}|^2 \frac{|\psi(\mathbf{r}=0)|^2}{\hbar\omega + i\gamma - E(X^0) - \Xi} , \quad (\text{A.18})$$

where $E(X^0)$ is the exciton energy, γ accounts for broadening, d_{cv} is the intervalley optical dipole moment and ψ is the exciton wavefunction.

It was shown that in the regime when $E_F < E_b(X^-)$, the self energy Ξ can be written as [18]

$$\Xi(\hbar\omega) = \int_0^\infty g_{2D} f_{\text{FD}}(\epsilon) T(\hbar\omega + \epsilon) d\epsilon , \quad (\text{A.19})$$

where $f_{\text{FD}}(\epsilon)$ is the Fermi-Dirac distribution describing the occupation of the Fermi-sea, $g_{2D} = \frac{m_{CB}^*}{2\pi\hbar^2}$ is the two-dimensional density of states (without spin-degeneracy), m_{CB}^* is the effective electron mass in the conduction band and $T(\epsilon)$ is the two-particle T -matrix.

Under the assumption that the electrons of a Fermi-sea interact only with excitons composed with an electron of opposite spin (singlet collision) forming a bound state (singlet trion) the T -matrix elements are [18]*

$$T(\hbar\omega) = T_s(\hbar\omega) = \frac{2\pi\hbar^2}{\mu_T} \frac{1}{\ln\left(\frac{-E_b(X^-)}{\hbar\omega - E(X^0) + i\gamma}\right)} , \quad (\text{A.20})$$

where μ_T is the reduced exciton-electron mass. μ_T can be written as

$$\frac{1}{\mu_T} = \frac{1}{m_{CB}^*} + \frac{1}{m_{VB}^* + m_{CB}^*} , \quad (\text{A.21})$$

with m_{VB}^* the effective electron masses in the valence band.

Suris [19, 20] derived a model of absorption of a 2DEG considering the effect of both singlet and triplet collisions. In a singlet collision, exciton-electron interaction has a bound state corresponding to the singlet trion. On the contrary, in triplet collision, they are no bound states of the exciton-electron interaction. The absence of a bound state comes the fact that triplet trions are unbound in the absence of magnetic fields [24].

In his model, [19, 20] the two types of interactions are introduced by decomposing the T -matrix in two parts $T = \frac{1}{2}T_s + \frac{3}{2}T_t$, with T_s accounting for singlet interactions and T_t

*The terms presented here neglect the center of mass motion of trions and also neglect the impact of Pauli blocking on the trion wavefunction. Taking the center of mass motion of the trion and the modification of the trion's wavefunction do not change significantly the results shown here.

for triplet interactions in the scattering of an electron on an exciton. As his scattering matrix elements T_s are in agreements with those of equation (A.20), we generalize here the results from Ref. [18] to the case of singlet and triplet interactions inspired by the work from Suris [19, 20].

The T -matrix elements accounting for triplet interactions can be written as [19, 20]

$$T_t(\hbar\omega) = \frac{2\pi\hbar^2}{\mu_T} \frac{1}{\ln \left(\frac{-E_b(X^0)}{\hbar\omega - E(X^0) + i\gamma} \frac{E_b(X^0)}{\alpha E_b(X^-)} \right)} , \quad (\text{A.22})$$

where $\alpha \approx 1$ is a number.

Fig. A.8 shows the contributions of the different T -matrix components to the optical susceptibility. Fig. A.8 (a, c) show the optical susceptibility resulting only from singlet scattering ($T = T_s$)*. A sharp peak around 1.9 eV emerges with a finite Fermi level. It corresponds to the X^- , or more precisely to the attractive polaron. The X^0 resonance at 1.95 eV (repulsive polaron) is also influenced by the interaction. The X^0 resonance looses indeed quickly in amplitude and the line-shape becomes more asymmetrical as the Fermi-level increases.

When only triplet scattering ($T = T_t$) is allowed, as in Fig. A.8(b, d), there is no low energy peak, as there are no bound triplet trions. The X^0 resonance is however still modified by the presence of the Fermi sea. The amplitude of the X^0 decreases and the X^0 shifts to higher energy. The line-shape of the X^0 is also modified by the presence of electrons: as the Fermi level increases, the X^0 peak becomes less and less Lorentzian as a tail grows on its high energy side.

Comparison between Fig. A.8 (a) and Fig. A.8 (b) informs that an attractive electron-exciton interaction is responsible for a sharp low energy resonance (the X^- or attractive polaron), while a repulsive electron-exciton interaction tends to create a high energy tail to the X^0 . The prediction of the polaron model is in good agreement with our experimental data presented in Fig. 2 of the main text. However, the high energy trion X_{HE}^- has its line-width increase with increasing electron density due to the different nature of the Coulomb interaction.

The energetic difference between neutral exciton and trion, $\delta E = E(X^0) - E(X^-)$ can be used to measure variations of the Fermi level [25]. Hawrylak [26] showed that the X^- is the ground state of an electron-hole pair in a Fermi sea. The X^0 is then an ionised X^- . In the ionisation process, the electron must be dragged to the first available

* $T = T_s$ is actually an approximation. As we have two trions, the oscillator strength is somehow shared between the two trions. However, the low energy trion has a large part of the oscillator strength. It is therefore a good approximation to write $T = T_s$ for the X_{LE}^- .

state in the conduction band, at the Fermi level. The energy cost of ionising an X^- is therefore increasing with the Fermi-level, pushing the X^0 toward higher energies. In this picture, δE varies as the Fermi level E_F , *i. e.* $\frac{d}{dE_F}\delta E = 1$.

In the framework of exciton-polarons, changes in δE can also be related to changes in Fermi level. Fig. A.9(a) shows the evolution of the gradient $\frac{d}{dE_F}\delta E$ as a function of the Fermi level extracted from simulations, as in Fig. A.8. In the high density regime, the slope $\frac{d}{dE_F}\delta E = 1$ is in agreement with Ref. [26]. However, as the electron density decreases, the slope increases up to $\frac{d}{dE_F}\delta E = 2$.

In our experiment, we can observe trions at Fermi levels ranging from 5 meV to 25 meV (two bands filled). In this regime, the gradient is varying slightly from 1.5 to 1, and equals on average 1.2. Fig. A.9(b) shows δE as a function of the electron density n . We find that in the regime where we can observe the trion, δE varies as 6.6×10^{-15} eVcm² with n , using an electron mass $m_{CB}^* = 0.44$ [14].

The gradients $\frac{d}{dE_F}\delta E$ measured experimentally presented in the main text for $X_{LE}^- (X_{HE}^-)$ are 6.1×10^{-15} eVcm⁻² (6.3×10^{-15} eVcm⁻²) in a 9 T magnetic field and 5.6×10^{-15} eVcm⁻² (5.9×10^{-15} eVcm⁻²) in the absence of a magnetic field. These values are in good agreement with the slope $\frac{d}{dE_F}\delta E = 6.6 \times 10^{-15}$ eVcm⁻² extracted from our simulations, as shown in Fig. A.9(b). In this rather limited range of electron densities, we cannot observe a significant change of the slope $\frac{d}{dE_F}\delta E$.

A.6 Band filling and optics in MoS₂

In the main text, we explain our optical spectra by a spin polarization of the 2DEG electrons. This section aims at describing how only a spin polarization of the 2DEG with two bands filled can explain the optical susceptibilities presented in the main text in Fig. 2. The optical susceptibility of MoS₂ in a magnetic field is dominated by two peaks at lower energy than the neutral exciton (X^0) in one polarization. In the other polarization, the optical susceptibility is dominated by the neutral exciton and no other resonances appear in the susceptibility before the appearance of the Q -peak. We review here the different ways of filling the bands and their consequence on the optics by commenting Fig. A.10.

One band filled. When only one band is filled the 2DEG is simultaneously spin- and valley-polarized. Such a band filling, as in Fig. A.10(a) is observed in MoSe₂ when placed in a magnetic field [11]. It was observed [11] that when an electron-hole pair is created

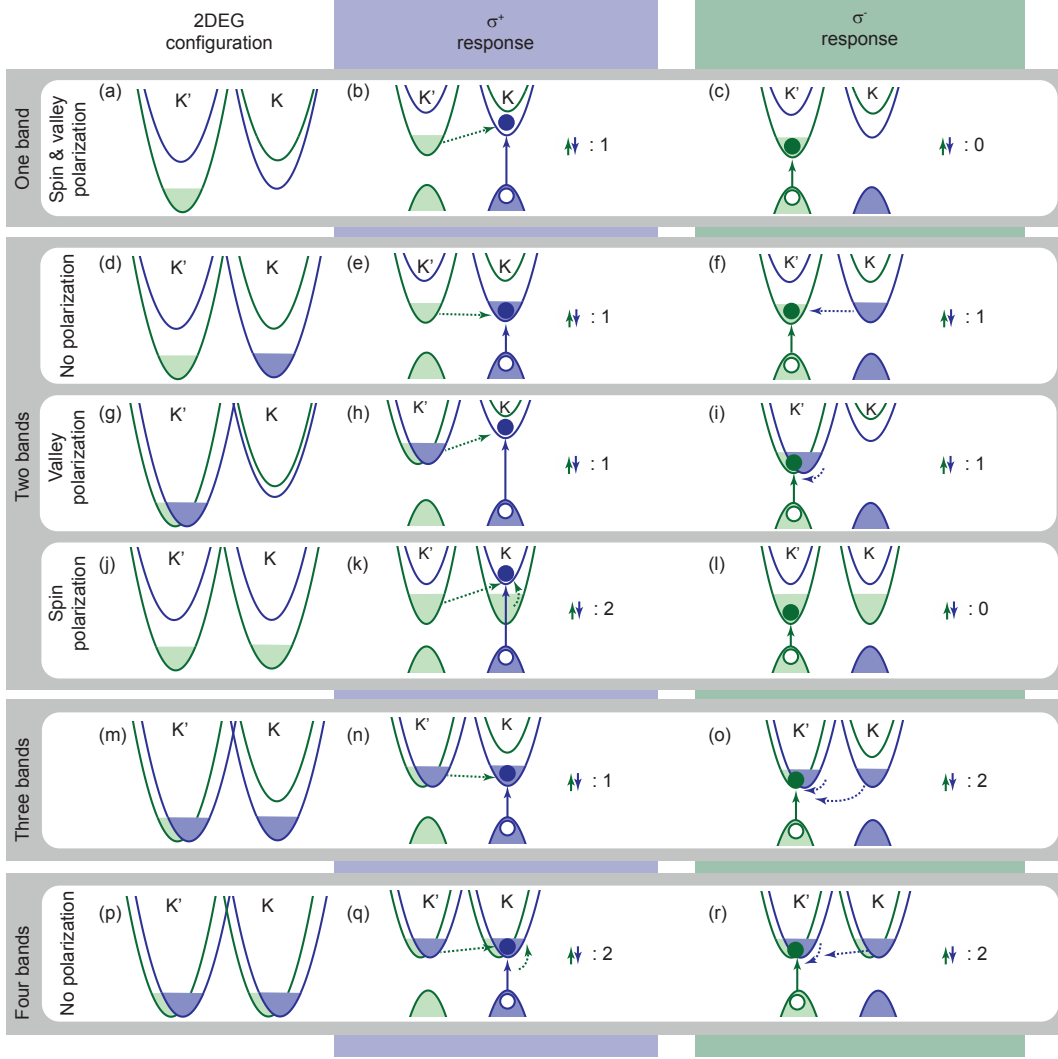


Fig. A.10. Possible band filling in MoS₂ and consequences on the optical susceptibility.

in the filled band, only the neutral exciton (X^0) appears in the optical susceptibility (Fig. A.10(c)). On the other hand, when the electron-hole pair is created in the empty band with opposite spin as in Fig. A.10(b), a low energy resonance identified as a trion or, more accurately, an attractive polaron dominates the susceptibility. This result is completely compatible with theory presented in the previous Section : an attractive polaron (low energy resonance) is formed when the spin of the electrons in the 2DEG is opposite to that of the electron component of the photo-generated electron-hole pairs. As we find that we have two types of low energy resonances, we can conclude that we fill more than a single band.

Two bands filled. If the two spin-split conduction bands were energetically well far apart, in the absence of many-body interactions, it would be expected that only the two lowest energy bands would be populated, as in Fig. A.10(d). In this case, the 2DEG filling is symmetric in both spin and valley population. The optical response is therefore also expected to be independent on the polarization of the light, in contradiction to our measurements.

Another possibility of two bands filling is to create a valley polarization: all electrons are located at the K' of the Brillouin zone with both spin up and spin down population, as depicted in Fig. A.10(g). When an electron-hole pair is formed in the same valley K' as the 2DEG electrons (Fig. A.10(i)), the optical response should be similar to that of two dimensional structures of conventional direct band-gap semiconductor with band edges at the Γ -point, such as GaAs. In the absence of magnetic field, in GaAs, only the singlet trion is observed [27]. As the magnetic field increases, the triplet trion emerges as a low energy shoulder of the X^0 , before being resolved as a separated resonance at high magnetic field. In our case, it would then be expected that when an electron-hole pair is created in the K' valley (σ^- polarized light), as in Fig. A.10(i), where the 2DEG electrons are, at least one resonance should appear in the optical susceptibility. When measuring the susceptibility using σ^+ polarized light (Fig. A.10(h)), there is also one possibility of creating a singlet trion. If the 2DEG was forming a valley polarization in MoS₂ with two filled bands, we would then have at least one resonance in both polarizations. This is also in contradiction with our measurements.

As written in the main text, our results are best explained by a spin polarization (Fig. A.10(j)): when an electron-hole pair is formed in the K valley (σ^+ polarized light), the promoted electron carries opposite spin to that of the electrons, as shown in Fig. A.10(k). Two possible singlet trions can be observed in this polarization. On the other hand, when a σ^- polarized photon promotes an electron with spin up (Fig. A.10(l)) it can only interact repulsively with electrons of the same spin, as explained in the previous Section. No bound states are then observed in this polarization, in agreement with our experimental results.

Three bands filled. The experimental results obtained on MoSe₂ tell us that the optical response of an electron-hole pair created in a filled band is barely modified by the presence of the electrons [11]. Merely a decrease in oscillator strength and an energetic

shift of the X^0 resonance are indeed observed. The three bands filling case as represented in Fig. A.10(m), when probed with σ^+ light (Fig. A.10(n)) is therefore similar to the case of the two bands valley polarization in Fig. A.10(h). At least one resonance should then be observed in this polarization. When the light is σ^- polarized (Fig. A.10(o)), the three bands case is then similar to the two bands spin-polarized case in Fig. A.10(k) and at least two resonances should be observed in this polarization. The three bands filling case is therefore in contradiction with our measurements.

Four bands filled.

Similarly to the unpolarized two-band case, as the four bands 2DEG band filling, as in Fig. A.10(p), is symmetric in both spin and valley filling, the optical response should also be similar in both polarizations.

A.7 Temperature dependence of the optical susceptibility

As temperature increases, electrons in the 2DEG start to populate excited states of the 2DEG. These fluctuations mitigate the Coulomb effects and eventually kill the spin-polarization [28, 29]. Fig. A.11 shows the evolution of the trion contrast, C with increasing temperature. The data was obtained in a magnetic field $B_z = 9$ T and at an electron density $n = 2.1 \cdot 10^{12} \text{ cm}^{-2}$. The red solid line shows the dependence one could expect from our phenomenological description of the trion contrast $C(T) = \tanh(\mu_B g B_z / k_B T)$, where μ_B is the Bohr magneton, k_B the Boltzmann constant and $g = 1.0$ was extracted from Fig. 3(f) in the main text. It is however difficult to interpret high temperature data as the features in the optical susceptibility broaden.

A.7.1 Reproducibility of the data

Five different samples, labelled as D1, D2, D3, D4 and D5 were fabricated to verify the reproducibility of the data presented in the main text (data obtained on sample D5).

We begin our analysis by showing that the optical properties behave qualitatively the same way in all samples. Fig. A.13 shows the imaginary part of the optical susceptibility in the two polarisations of light (left column, σ^- , and right column, σ^+) in an out-of-plane magnetic field $B_z = 9.0$ T. The different rows correspond to different samples. All samples demonstrate charging and spin-polarisation. In σ^+ polarisation, the oscillator strength is transferred from the neutral exciton (X^0) to the negatively charged excitons

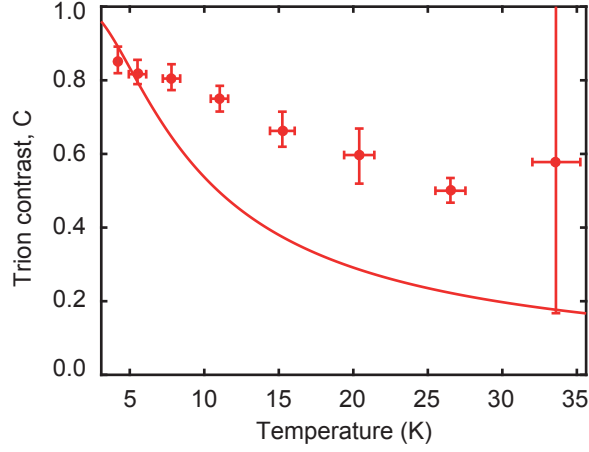


Fig. A.11. **Temperature dependence of the trion contrast, C .** The solid line is the Maxwell-Boltzmann distribution discussed in the main text.

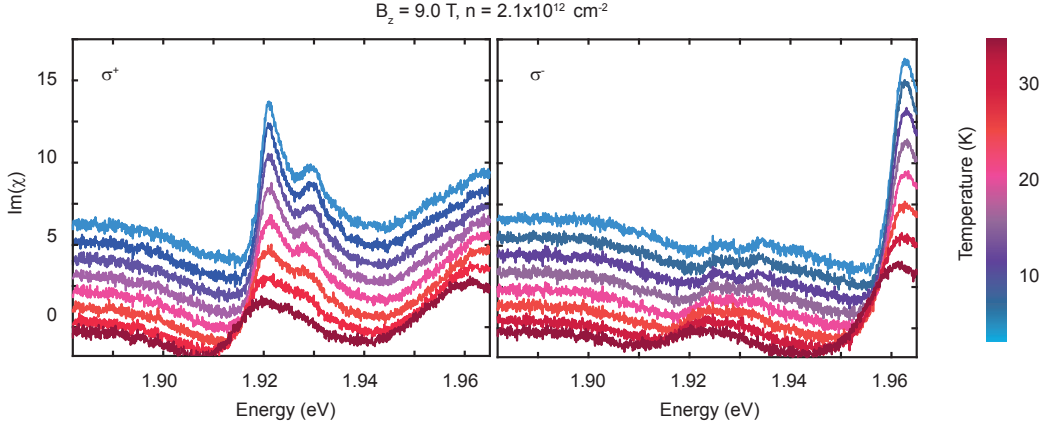


Fig. A.12. **Temperature dependence of the imaginary part of the optical susceptibility.**

(X_{LE}^- and X_{HE}^-) to the Q -peak. On the other hand, in σ^- the oscillator strength is transferred directly from the X^0 to the Q -peak, hence demonstrating the unavailability of electrons with spin-down.

In samples D3 and D5, the monolayer MoS_2 was passivated in TFSI acid prior to encapsulation, while in D1, D2 and D4, no passivation was performed. As the optical properties qualitatively remain the same in all the different samples, we can conclude that the TFSI acid passivation does not modify fundamentally (*i.e.* the density of states remains unchanged) the optical properties of encapsulated monolayer MoS_2 .

When a voltage V_G is applied between the contacts on the MoS_2 and the doped-silicon back-gate, the electron density n can be deduced from the back-gate capacitance. How-

Table A.1. Measured variation of the Fermi level with changing back-gate voltage.

Sample	dE_F/dV_G (meV/V)
D1	0.22
D2	0.26
D3	0.11
D4	0.24
D5	0.36
Theory	0.37

ever, n can be only deduced from the gate capacitance in the case of perfect ohmic contacts (no potential barrier at the contact) and are assuming a zero contact capacitance [30]. Our optical experiment can measure the Fermi-level E_F variation as V_G changes, as

$$\frac{dE_F}{dV_G} = \frac{1}{1.2} \frac{d}{dV_G} (E(X^0) - E(X^-)) , \quad (\text{A.23})$$

where $E(X^0)$ is the energy of the neutral exciton, $E(X^-)$ is the energy of a negatively charged exciton and the factor $1/1.2$ is a correction coming from the exciton-polaron model (*See Section A.5*). The gradient dE_F/dV_G extracted experimentally in the main text (sample D5) is in good agreement with the values expected from theory, using DFT predicted effective electron mass [14]. This good agreement tells us that the electron injection in sample D5 is working well. Table A.1 shows the measured variations of the Fermi level as a function of the gate voltage. We used the different slopes to rescale the electron density axis in Fig. A.13, such as the energetic separation between X^0 and X_{LE}^- and X_{HE}^- varies the same way with a variation of the electron density as in sample D5. With the rescaling, we can see that the two peaks X_{LE}^- and X_{HE}^- always appear at the same carrier densities and that the onset of the Q -peak always takes place at the same carrier densities ($\approx 6 \cdot 10^{12} \text{ cm}^{-2}$), which demonstrate that the sample to sample difference can be explained by a less efficient carrier injection.

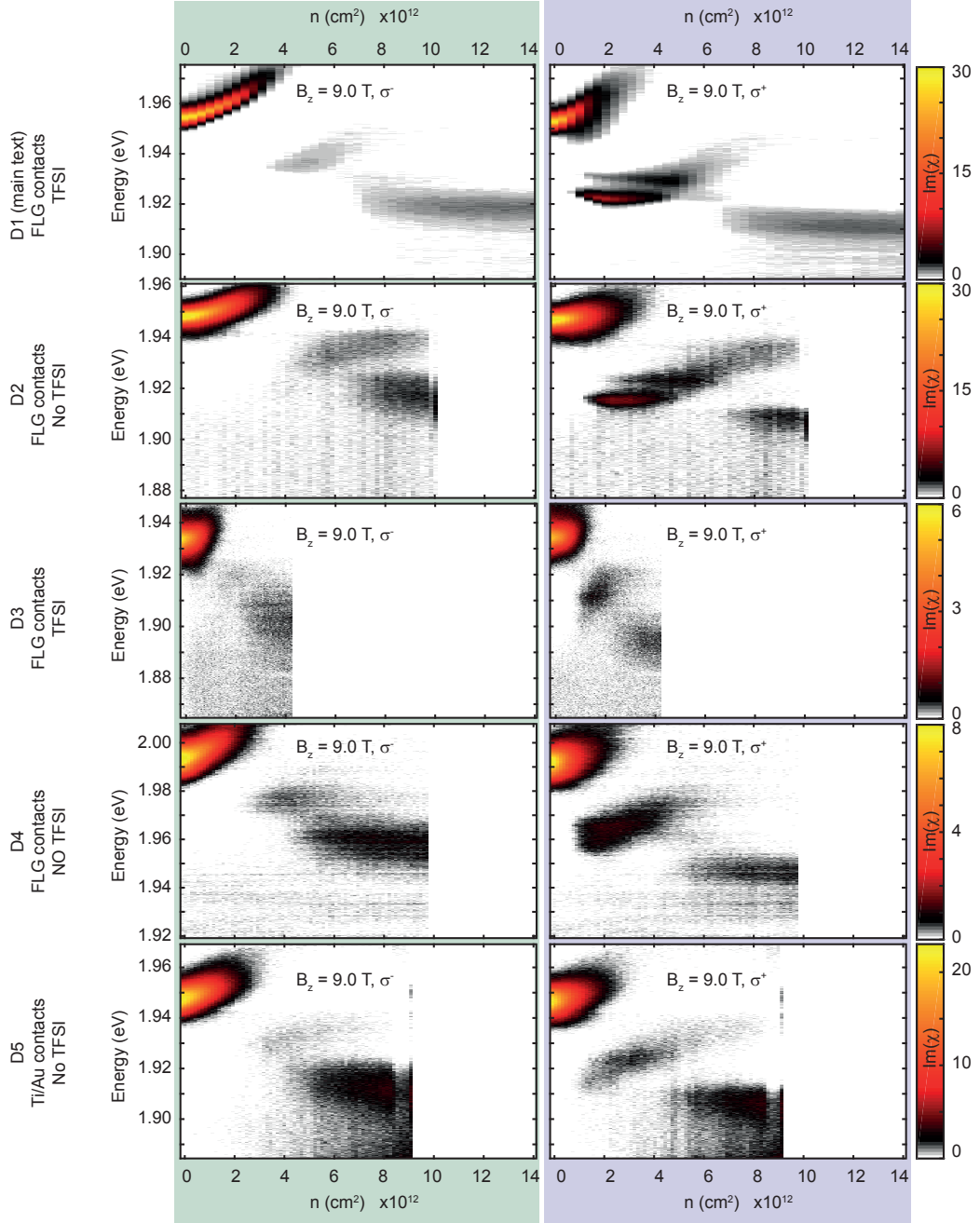


Fig. A.13. Imaginary part of the optical susceptibility at various electron concentrations in a magnetic field $B_z = 9$ T obtained on different samples labeled as D1 to D5. The data presented in the main text are the data extracted from sample D5. The dashed areas indicate densities out of reach with the different samples D1 to D4.

Bibliography

- [1] Zomer, P., Guimarães, M., Brant, J., Tombros, N. & Van Wees, B. Fast pick up technique for high quality heterostructures of bilayer graphene and hexagonal boron nitride. *Appl. Phys. Lett.* **105**, 013101 (2014).
- [2] Taniguchi, T. & Watanabe, K. Synthesis of high-purity boron nitride single crystals under high pressure by using Ba–BN solvent. *J. Cryst. Growth* **303**, 525–529 (2007).
- [3] Amani, M. *et al.* Near-unity photoluminescence quantum yield in MoS₂. *Science* **350**, 1065–1068 (2015).
- [4] Yu, L. *et al.* Graphene/MoS₂ hybrid technology for large-scale two-dimensional electronics. *Nano Lett.* **14**, 3055–3063 (2014).
- [5] Laturia, A., de Put, M. L. V. & Vandenberghe, W. G. Dielectric properties of hexagonal boron nitride and transition metal dichalcogenides: from monolayer to bulk. *NPJ 2D Mater. Appl.* **2** (2018).
- [6] Ju, L. *et al.* Photoinduced doping in heterostructures of graphene and boron nitride. *Nat Nanotechnol.* **9** (2014).
- [7] Epping, A. *et al.* Quantum transport through MoS₂ constrictions defined by photodoping. *J Phys Condens Matter.* **30** (2018).
- [8] Wang, H., Wu, Y., Cong, C., Shang, J. & Yu, T. Hysteresis of electronic transport in graphene transistors. *ACS Nano.* **4** (2010).
- [9] McIntyre, J. D. E. & Aspnes, D. E. Differential reflection spectroscopy of very thin surface films. *Surf. Sci.* **24**, 417 (1971).
- [10] Arora, A., Mandal, A., Subhananda, C. & Ghosh, S. Magneto-optical Kerr effect spectroscopy based study of Landé g-factor for holes in GaAs/AlGaAs single quantum wells under low magnetic fields. *J. Appl. Phys.* **113**, 213505 (2013).
- [11] Back, P. *et al.* Giant paramagnetism-induced valley polarization of electrons in charge-tunable monolayer MoSe₂. *Phys. Rev. Lett.* **118**, 237404 (2017).

- [12] Cadiz, F. *et al.* Excitonic linewidth approaching the homogeneous limit in MoS₂-based van der Waals heterostructures. *Phys. Rev. X* **7**, 021026 (2017).
- [13] Dey, P. *et al.* Optical coherence in atomic-monolayer transition-metal dichalcogenides limited by electron-phonon interactions. *Phys. Rev. Lett.* **116**, 127402 (2016).
- [14] Kormányos, A., Zoloyomi, V., Drummond, N. D. & Burkard, G. Spin-orbit coupling, quantum dots, and qubits in monolayer transition metal dichalcogenides. *Phys. Rev. X* **4**, 011034 (2014).
- [15] Aivazian, G. *et al.* Magnetic control of valley pseudospin in monolayer WSe₂. *Nat. Phys.* **11**, 148–152 (2015).
- [16] Xiao, D., Liu, G.-B., Feng, W., Xu, X. & Yao, W. Coupled spin and valley physics in monolayer of MoS₂ and other group-VI dichalcogenides. *Phys. Rev. Lett.* **108**, 196902 (2012).
- [17] Rybkovskiy, D. V., Gerber, I. C. & Durnev, M. V. Atomically inspired k·p approach and valley Zeeman effect in transition metal dichalcogenide monolayers. *Phys. Rev. B* **95**, 155406 (2017).
- [18] Efimkin, D. K. & MacDonald, A. H. Many-body theory of trion absorption features in two-dimensional semiconductors. *Phys. Rev. B* **95**, 035417 (2017).
- [19] Suris, R. A. *et al.* Excitons and trions modified by interaction with a two-dimensional electron gas. *Phys. Status Solidi B* **227**, 343–352 (2001).
- [20] Ossau, W. J. & Suris, R. *Optical Properties of 2D Systems with Interacting Electrons* (Kluwer Academic Publishers, 2003).
- [21] Massignan, P., Zaccanti, M. & Bruun, G. M. Polarons, dressed molecules and itinerant ferromagnetism in ultracold Fermi gases. *Rep. Prog. Phys.* **77**, 034401 (2014).
- [22] Sidler, M. *et al.* Fermi polaron-polaritons in charge-tunable atomically thin semiconductors. *Nat. Phys.* **13**, 255–261 (2016).
- [23] Haug, H. & Koch, S. W. *Quantum Theory of the Optical and Electronic Properties of Semiconductors* (World Scientific, 2004), 4 edn.

- [24] Whittaker, D. M. & Shields, A. J. Theory of X^- at high magnetic fields. *Phys. Rev. B* **56**, 15185 (1997).
- [25] Huard, V., Cox, R. T., Saminadayar, K., Arnoult, A. & Tatarenko, S. Bound states in optical absorption of semiconductor quantum wells containing a two-dimensional electron gas. *Phys. Rev. Lett.* **84**, 187 (2000).
- [26] Hawrylak, P. Optical properties of a two-dimensional electron gas: Evolution of spectra from excitons to Fermi-edge singularities. *Phys. Rev. B* **44**, 3821 (1991).
- [27] Shields, A., Pepper, M., Simmons, M. & Ritchies, D. Spin-triplet negatively charged excitons in GaAs quantum wells. *Phys. Rev. B* **52**, 7841 (1995).
- [28] Anderson, P. W. *Theory of Magnetic Exchange Interactions: Exchange in Insulators and Semiconductors* (Academic Press, 1963).
- [29] Wang, Z., Mak, K. F. & Shan, J. Strongly interaction-enhanced valley magnetic response in monolayer WSe₂. *Phys. Rev. Lett.* **120**, 066402 (2018).
- [30] Michailow, W. *et al.* Combined electrical transport and capacitance spectroscopy of a MoS₂-LiNbO₃ field effect transistor. *Appl. Phys. Lett.* **110**, 023505 (2017).

Appendix B

Details of the Hartree-Fock calculation

In this Appendix, we present the details of the operator algebra needed to derive the Hartree-Fock results presented in Section 2.3.

B.1 Idea of the computation

We perform here a variational computation of the energy of the 2DEG. We consider that the 2DEG wavefunction is described by a Fermi sea occupying a volume Ω in the reciprocal space. The goal is to minimize the 2D electron gas energy by finding the optimal Ω .

The domain Ω is defined in terms of the Fermi wavevectors $k_F^{\sigma,\tau}$ in the different valleys (momentum measured from the bottom of the bands). Using the definitions of Fig. B.1, Ω can be written as

$$\Omega = \bigcup_{\sigma=\pm 1, \tau=\pm 1} \{k, \text{ s.t. } |k| < k_F^{\sigma,\tau}\} \quad (\text{B.1})$$

$$|\Psi_\Omega\rangle = \prod_{(k,\sigma,\tau) \in \Omega} \hat{a}_{k,\sigma,\tau}^\dagger |0\rangle \quad (\text{B.2})$$

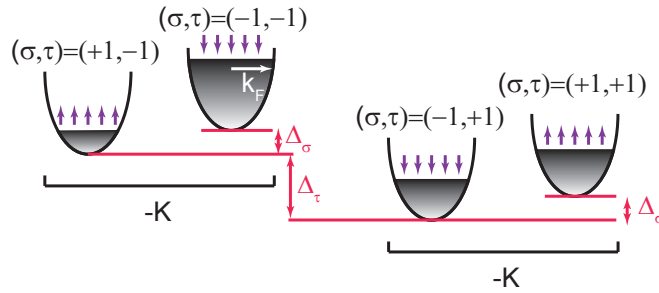


Fig. B.1. The four bands are distinguished by their spin index $\sigma = \pm 1$ and their valley index $\tau = \pm 1$. The two valleys are at $-K$ ($\tau = -1$) and at $+K$ ($\tau = 1$).

The Hamiltonian of the system is given by the sum of the kinetic energy and potential energy

$$\hat{H} = \hat{H}_{kin} + \hat{H}_{pot} \quad , \quad (\text{B.3})$$

where

$$\hat{H}_{kin} = \sum_{(k,\sigma,\tau)} \epsilon_{\sigma,\tau}(k) \hat{a}_{k,\sigma,\tau}^\dagger \hat{a}_{k,\sigma,\tau} \quad . \quad (\text{B.4})$$

$\epsilon_{\sigma,\tau}(k)$ are the single particle energies given by

$$\epsilon_{\sigma,\tau}(k) = \frac{\Delta_\sigma}{2}\sigma + \frac{\Delta_\tau}{2}\tau + \frac{\hbar^2 k^2}{2m} \quad , \quad (\text{B.5})$$

where the spin index σ and the valley index τ take values 1 or -1.

$$\tau, \sigma \in \{+1; -1\} \quad .$$

The potential energy operator \hat{H}_{pot} is made of two contributions: the intravalley Coulomb interaction \hat{H}_{pot}^{intra} and the intervalley Coulomb interaction \hat{H}_{pot}^{inter}

$$\hat{H}_{pot}^{intra} = \frac{1}{2} \sum_{q \neq 0} \sum_{(k,\sigma,\tau)} \sum_{(k',\sigma',\tau')} V_q \hat{a}_{k+q,\sigma,\tau}^\dagger \hat{a}_{k'-q,\sigma',\tau'}^\dagger \hat{a}_{k',\sigma',\tau'} \hat{a}_{k,\sigma,\tau} \quad (\text{B.6})$$

where (SI units)

$$V_q = \frac{e^2}{2\epsilon_0\epsilon_r L^2} \frac{1}{q} \quad (\text{B.7})$$

is the Fourier transform of the Coulomb potential. The intervalley Coulomb interaction can be described by this term:

$$\hat{H}_{pot}^{inter} = \frac{1}{2} \sum_q \sum_{(k,\sigma,\tau)} \sum_{(k',\sigma',\tau')} V_{q+2\tau K} \hat{a}_{k+q,\sigma,-\tau}^\dagger \hat{a}_{k'-q,\sigma',-\tau'}^\dagger \hat{a}_{k',\sigma',\tau'} \hat{a}_{k,\sigma,\tau} \quad (\text{B.8})$$

However, as q is of the order of $k_F \ll K$, it seems reasonable to approximate the intervalley scattering by replacing $V_{q+\tau K}$ by V_K and simplify the intervalley scattering term:

$$\hat{H}_{pot}^{inter} \approx \frac{1}{2} \sum_q V_{|K|} \sum_{(k,\sigma,\tau)} \sum_{(k',\sigma',\tau')} \hat{a}_{k+q,\sigma,-\tau}^\dagger \hat{a}_{k'-q,\sigma',-\tau'}^\dagger \hat{a}_{k',\sigma',\tau'} \hat{a}_{k,\sigma,\tau} \quad (\text{B.9})$$

Now that we have the Hamiltonian of the system, we need to measure the energy E_Ω

for each trial wavefunction $|\Psi_\Omega\rangle$.

$$E_\Omega = \langle \Psi_\Omega | \hat{H} | \Psi_\Omega \rangle = \langle \Psi_\Omega | \hat{H}_{kin} | \Psi_\Omega \rangle + \langle \Psi_\Omega | \hat{H}_{pot}^{intra} | \Psi_\Omega \rangle + \langle \Psi_\Omega | \hat{H}_{pot}^{inter} | \Psi_\Omega \rangle \quad (\text{B.10})$$

B.2 Kinetic energy term

$$E_\Omega^{kin} = \langle \Psi_\Omega | \hat{H}_{kin} | \Psi_\Omega \rangle = \sum_{(k,\sigma,\tau)} \epsilon_{\sigma,\tau}(k) \underbrace{\langle \Psi_\Omega | \hat{a}_{k,\sigma,\tau}^\dagger \hat{a}_{k,\sigma,\tau} | \Psi_\Omega \rangle}_{\Theta(|k| < k_F^{\sigma,\tau})} \quad (\text{B.11})$$

where the function $\Theta(x)$ equals 1 when x is true and 0 otherwise. The summation over k can be replaced by an integral up to the Fermi wavevector

$$E_\Omega^{kin} = \sum_{(\sigma,\tau)} \frac{L^2}{\pi^2} \int_0^{k_F^{\sigma,\tau}} dk \, 2\pi k \epsilon_{\sigma,\tau}(k) = \sum_{(\sigma,\tau)} \frac{L^2}{\pi} \left[(k_F^{\sigma,\tau})^2 \left(\frac{\Delta_\sigma}{2} \sigma + \frac{\Delta_\tau}{2} \tau \right) + \frac{1}{4} (k_F^{\sigma,\tau})^4 \frac{\hbar^2}{m} \right]$$

As the Fermi wavevector k_F is related to the carriers in a band by the simple relationship $k_F^{\sigma,\tau} = \sqrt{2\pi n_{\sigma,\tau}}$, the kinetic energy may also be rewritten as

$$E_\Omega^{kin} = \sum_{(\sigma,\tau)} \frac{L^2}{\pi} \left[2\pi n_{\sigma,\tau} \left(\frac{\Delta_\sigma}{2} \sigma + \frac{\Delta_\tau}{2} \tau \right) + \pi^2 n_{\sigma,\tau}^2 \frac{\hbar^2}{m} \right] \quad (\text{B.12})$$

B.3 Intervalley Coulomb term

$$E_\Omega^{pot,inter} = \langle \Psi_\Omega | \hat{H}_{pot}^{inter} | \Psi_\Omega \rangle$$

$$E_\Omega^{pot,inter} = \frac{1}{2} \sum_q V_{|K|} \sum_{(k,\sigma,\tau)} \sum_{(k',\sigma',\tau')} \langle \Psi_\Omega | \hat{a}_{k+q,\sigma,-\tau}^\dagger \hat{a}_{k'-q,\sigma',-\tau'}^\dagger \hat{a}_{k',\sigma',\tau'} \hat{a}_{k,\sigma,\tau} | \Psi_\Omega \rangle \quad (\text{B.13})$$

Let's start by rewriting the term $\hat{a}_{k+q,\sigma,-\tau}^\dagger \hat{a}_{k'-q,\sigma',-\tau'}^\dagger \hat{a}_{k',\sigma',\tau'} \hat{a}_{k,\sigma,\tau}$ in an easier way:

$$\begin{aligned} \hat{a}_{k+q,\sigma,-\tau}^\dagger \underbrace{\hat{a}_{k'-q,\sigma',-\tau'}^\dagger \hat{a}_{k',\sigma',\tau'}}_{\text{swap } (\tau' \neq -\tau')} \hat{a}_{k,\sigma,\tau} &= -\hat{a}_{k+q,\sigma,-\tau}^\dagger \hat{a}_{k',\sigma',\tau'} \hat{a}_{k'-q,\sigma',-\tau'}^\dagger \hat{a}_{k,\sigma,\tau} \\ &= -\hat{a}_{k+q,\sigma,-\tau}^\dagger \hat{a}_{k',\sigma',\tau'} \delta_{\sigma,\sigma'} \delta_{\tau,-\tau'} \delta_{k,k'-q} \Theta(k < k_F^{\sigma,\tau}) \end{aligned} \quad (\text{B.14})$$

In the last equation, the Kroenecker functions appear by the fact that the hole created by $\hat{a}_{k,\sigma,\tau}$ can only be filled by the creation operator $\hat{a}_{k'-q,\sigma',-\tau'}^\dagger$, as the other creation

operator only operates in the other valley ($-\tau$). This result can be plugged into the expression for $E_{\Omega}^{pot,inter}$:

$$\begin{aligned}
E_{\Omega}^{pot,inter} &= -\frac{1}{2} \sum_q V_{|K|} \sum_{(k,\sigma,\tau)} \sum_{(k',\sigma',\tau')} \langle \Psi_{\Omega} | \hat{a}_{k+q,\sigma,-\tau}^{\dagger} \hat{a}_{k',\sigma',\tau'} \delta_{\sigma,\sigma'} \delta_{\tau,-\tau'} \delta_{k,k'-q} | \Psi_{\Omega} \rangle \Theta(k < k_F^{\sigma,\tau}) \\
&= -\frac{1}{2} V_{|K|} \sum_{(k,\sigma,\tau)} \sum_q \langle \Psi_{\Omega} | \hat{a}_{k+q,\sigma,-\tau}^{\dagger} \hat{a}_{k+q,\sigma,-\tau} | \Psi_{\Omega} \rangle \Theta(k < k_F^{\sigma,\tau}) \\
&= -\frac{1}{2} V_{|K|} \sum_{(\sigma,\tau)} \sum_{k,k'} \langle \Psi_{\Omega} | \hat{a}_{k',\sigma,-\tau}^{\dagger} \hat{a}_{k',\sigma,-\tau} | \Psi_{\Omega} \rangle \Theta(k < k_F^{\sigma,\tau}) \\
&= -\frac{1}{2} V_{|K|} \sum_{(\sigma,\tau)} \sum_{k,k'} \Theta(k' < k_F^{\sigma,-\tau}) \Theta(k < k_F^{\sigma,\tau}) \\
&= -\frac{1}{2} V_{|K|} \sum_{(\sigma,\tau)} \left(\frac{L^2}{\pi^2} \right)^2 \int_0^{k_F^{\sigma,-\tau}} dk' 2\pi k' \int_0^{k_F^{\sigma,\tau}} dk 2\pi k \\
E_{\Omega}^{pot,inter} &= -\frac{1}{2} V_{|K|} \frac{L^4}{\pi^2} \sum_{(\sigma,\tau)} [k_F^{\sigma,-\tau}]^2 [k_F^{\sigma,\tau}]^2 = -2 V_{|K|} L^4 \sum_{\sigma,\tau} n_{\sigma,-\tau} n_{\sigma,\tau} \quad (B.15)
\end{aligned}$$

B.4 Intravalley Coulomb term

$$E_{\Omega}^{pot,intra} = \langle \Psi_{\Omega} | \hat{H}_{pot}^{inter} | \Psi_{\Omega} \rangle$$

$$E_{\Omega}^{pot,intra} = \frac{1}{2} \sum_{q \neq 0} \sum_{(k,\sigma,\tau)} \sum_{(k',\sigma',\tau')} V_q \langle \Psi_{\Omega} | \hat{a}_{k+q,\sigma,\tau}^{\dagger} \hat{a}_{k'-q,\sigma',\tau'}^{\dagger} \hat{a}_{k',\sigma',\tau'} \hat{a}_{k,\sigma,\tau} | \Psi_{\Omega} \rangle \quad (B.16)$$

Let's rewrite the term sandwiched between the brackets in an easier way: as $q \neq 0$,

$$\begin{aligned}
\hat{a}_{k+q,\sigma,\tau}^{\dagger} \underbrace{\hat{a}_{k'-q,\sigma',\tau'}^{\dagger} \hat{a}_{k',\sigma',\tau'}}_{\text{swap } (q \neq 0)} \hat{a}_{k,\sigma,\tau} &= -\hat{a}_{k+q,\sigma,\tau}^{\dagger} \hat{a}_{k',\sigma',\tau'} \underbrace{\hat{a}_{k'-q,\sigma',\tau'}^{\dagger} \hat{a}_{k,\sigma,\tau}}_{\text{swap}} \\
&= -\hat{a}_{k+q,\sigma,\tau}^{\dagger} \hat{a}_{k',\sigma',\tau'} (\delta_{k,k'-q} \delta_{\sigma',\sigma} \delta_{\tau,\tau'} - \underbrace{\hat{a}_{k,\sigma,\tau} \hat{a}_{k'-q,\sigma',\tau'}^{\dagger}}_{=0 \text{ } (|k'-q| < k_F^{\sigma,\tau})}) \quad (B.17)
\end{aligned}$$

Inserting the last expression in the expression for the intervalley potential energy yields

$$E_{\Omega}^{pot,intra} = -\frac{1}{2} \sum_{\sigma,\tau} \sum_{(k,k',k \neq k')} V_{k'-k} \langle \Psi_{\Omega} | \hat{a}_{k,\sigma,\tau}^{\dagger} \hat{a}_{k,\sigma,\tau} | \Psi_{\Omega} \rangle \Theta(|k'| < k_F^{\sigma,\tau}) \quad (\text{B.18})$$

$$E_{\Omega}^{pot,intra} = \sum_{\sigma,\tau} \left[-\frac{1}{2} \sum_{(k,k',k \neq k')} V_{k'-k} \Theta(|k| < k_F^{\sigma,\tau}) \Theta(|k'| < k_F^{\sigma,\tau}) \right] \quad (\text{B.19})$$

The expression between brackets is the standard Coulomb potential term that also appears in semiconductors with a single band located at the Γ point. This term can be computed in the 2D case, following Haug and Koch (Chapter 7.3)

$$E_{\Omega}^{pot,intra} = - \sum_{\sigma,\tau} \frac{L^2 e^2 C}{3\pi\epsilon_0} (2\pi n_{\sigma,\tau})^{3/2} \quad (\text{B.20})$$

where

$$C = \sum_{l=0,2,\dots,\infty} \frac{2}{l+2} \left[\frac{1}{2^l} \binom{l}{l/2} \right]^2 \approx 1.26 \quad (\text{B.21})$$

In the case of transition metal dichalcogenides, the Thomas-Fermi screening length $k_{TF} = 2/a_0$ is on the order of the Brillouin zone size. The Coulomb potential for an intravalley scattering is then essentially independent of the k vector. The Coulomb matrix element V_k can be then replaced by $V_{k_{TF}}$. In such a case, the final result has the same form as the intervalley exchange term:

$$E_{\Omega}^{pot,intra} = -\frac{1}{2} V_{k_{TF}} \frac{L^4}{\pi^2} \sum_{(\sigma,\tau)} [k_F^{\sigma,\tau}]^2 [k_F^{\sigma,\tau}]^2 = -2V_{k_{TF}} L^4 \sum_{\sigma,\tau} n_{\sigma,\tau}^2 \quad (\text{B.22})$$

B.5 Expression of the 2DEG as a function of carrier densities

Now that we have computed the different contributions to the total energy, we can put them all together.

In the absence of screening:

$$\begin{aligned} \frac{E_{\Omega}}{L^2} &= \frac{\langle \Psi_{\Omega} | \hat{H} | \Psi_{\Omega} \rangle}{L^2} \\ &= \sum_{\sigma,\tau} \left[\left[2n_{\sigma,\tau} \left(\frac{\Delta_{\sigma}}{2} \sigma + \frac{\Delta_{\tau}}{2} \tau \right) + \pi n_{\sigma,\tau}^2 \frac{\hbar^2}{m} \right] - 2L^2 V_{|K|} n_{\sigma,-\tau} n_{\sigma,\tau} - \frac{e^2 C}{3\pi\epsilon_0} (2\pi n_{\sigma,\tau})^{3/2} \right] \end{aligned} \quad (\text{B.23})$$

With screening:

$$\frac{E_\Omega}{L^2} = \sum_{\sigma,\tau} \left[\left[2n_{\sigma,\tau} \left(\frac{\Delta_\sigma}{2}\sigma + \frac{\Delta_\tau}{2}\tau \right) + \pi n_{\sigma,\tau}^2 \frac{\hbar^2}{m} \right] - 2L^2 V_{|K|} n_{\sigma,-\tau} n_{\sigma,\tau} - 2L^2 V_{k_{TF}} \sum_{\sigma,\tau} n_{\sigma,\tau}^2 \right] \quad (\text{B.24})$$

With $k_{TF} = 2/a_0$, noting that $a_0 = \frac{4\pi\epsilon_0\epsilon_r\hbar^2}{me^2}$

$$V_q^{Intra} = \frac{e^2}{2\epsilon_0\epsilon_r L^2} \frac{1}{q + k_{TF}} \underbrace{=}_{q < k_{TF}} \frac{e^2}{2\epsilon_0\epsilon_r L^2} \frac{1}{k_{TF}} = \frac{2\pi}{L^2} \frac{\hbar^2}{2m} \quad (\text{B.25})$$

$$V_K^{Inter} = \frac{e^2}{2\epsilon_0\epsilon_r L^2} \frac{1}{K + k_{TF}} \underbrace{=}_{K = \frac{4\pi}{3a}} \frac{4\pi}{L^2} \frac{\hbar^2}{2m} \frac{3a/a_0}{4\pi + 6a/a_0} \quad (\text{B.26})$$

Curriculum vitae

Jonas Gaël Roch

Personal information

Mailing address: Roggenburgstrasse 29, 4055 Basel, Switzerland
Email address: jonas.g.roch@gmail.com
Date of birth: 15th April 1992
Place of birth: Lausanne (VD), Switzerland
Citizenship: Switzerland

Education

2015-2019: **PhD in Experimental Physics**
University of Basel, Switzerland
Thesis: *Photonics of Monolayers of Transition Metal Dichalcogenides.*
Advisor: Prof. Richard John Warburton
Grade: TBA

2013-2015 **Master's in Applied Physics**
EPFL, Lausanne, Switzerland
Thesis: *Experimental study of GaN/AlGaIn multiple quantum wells for planar waveguides operating in the polaritonic regime.*
Advisor: Prof. Nicolas Grandjean

2013 (6 months) Carl Zeiss, Shanghai
Confocal scanning laser ophthalmoscope

2010-2013 **Bachelor's in Applied Physics**
EPFL, Lausanne, Switzerland

2012-2013 (1 year) Chinese University of Hong Kong
Exchange year

2007-2010 **High school**
Gymnase du Bugnon, Lausanne, Switzerland

List of publications

1. Jonas Gaël Roch, Guillaume Froehlicher, Nadine Leisgang, Peter Makk, Kenji Watanabe, Takashi Taniguchi and Richard John Warburton, *Spin-polarized electrons in monolayer MoS₂*, Nature Nanotechnology (2019)
2. Jonas Gaël Roch, Nadine Leisgang, Guillaume Froehlicher, Peter Makk, Kenji Watanabe, Takashi Taniguchi, Christian Schönenberger and Richard John Warburton, *Quantum-confined Stark effect in a MoS₂ monolayer van der Waals heterostructure*, Nano Letter, **18** (2), 1070-1074 (2018)
3. Nadine Leisgang, Jonas Gaël Roch, Guillaume Froehlicher, Matthew Hamer, Daniel Terry, Roman Gorbachev and Richard John Warburton, *Optical second harmonic generation in encapsulated single-layer InSe*, AIP Advances, **8** (10), 105120 (2018)
4. Joachim Ciers, Jonas Gaël Roch, Jean-François Carlin, Gwénolé Jacopin, Raphaël Butté and Nicolas Grandjean, *Propagating polaritons in III-nitride slab waveguides*, Physical Review Applied, **7** (3), 034019 (2017)